

11

MODES AND DISPERSION IN OPTICAL FIBERS

John Tyndall demonstrated in 1870 in front of an audience of the Royal Academy of London that light can travel within a curved jet stream of water from a hole made on the side of a water pail. Propagation was based on repeated total internal reflection at the air–water boundary. However, it was not until 1966, when Kao and Hockham [1] promoted the use of a glass fiber as the transmission medium, that the doors were opened to using the principle of total internal reflection as a viable means of communication. What followed was an intensive development of the purification process of glass materials to reduce transmission loss. Concurrently, improvements were realized in the design and control of critical parameters such as the dimensions and indices of refraction of the fiber layers.

Light propagates in an optical fiber by repeated total internal reflection at the core–cladding glass boundary. Optical fibers have a phenomenally large capacity to carry information and are able to deliver this information to extremely distant locations. Fiber-optic communication systems possess such advantages as:

- Low transmission loss
- Large capacity of information transmission
- No electromagnetic interference
- Lighter weight than copper
- No sparks even when short-circuited
- Higher melting point than copper
- Practically inexhaustible raw material supply

On the other hand, the disadvantages are:

- Connections and taps are more difficult to make than for copper wire.
- Fiber is not as flexible as a copper wire.

Among the advantages, low transmission loss and large capacity of information transmission are the two most important. The transmission loss of highly purified glass has become as low as 0.15 dB/km at $\lambda = 1.55 \mu\text{m}$. Considering the fact that an ordinary glass window just a few centimeters thick cuts the intensity of transmitted light in half, the fiber's loss is unbelievably low. A copper coaxial cable has a loss of approximately 10 dB/km at 50 MHz, so that a significant increase in the span between repeater stations has become possible using fiber-optic cables. In terms of frequency bandwidth, the first copper submarine cable of TAT 1 (Trans Atlantic Transmission) could send 64 voice channels in 1956 but now the submarine fiber-optic link around the globe (FLAG), which links Great Britain and Japan by way of the Middle East and South East Asia, can send 120,000 voice channels [2]. The undersea cables of TyCom Global Network (TGN) will connect major world cities via the Atlantic and Pacific Oceans and the Mediterranean Sea with a transmission capacity of over ten million voice channels [3].

11.1 PRACTICAL ASPECTS OF OPTICAL FIBERS

In this section, practical aspects of optical fibers that are necessary for designing an optical communication system will be explained. The emphasis here is on understanding concepts through simple arguments, leaving the more rigorous and quantitative expressions to a later part of this chapter.

11.1.1 Numerical Aperture of a Fiber

An optical fiber consists of core glass of higher index of refraction in the center, surrounded by cladding glass of lower index of refraction. As shown in Fig. 11.1, light traverses the core glass by *repeated total internal reflection at the boundary between the core and cladding glasses*. There are two paths of propagation in a fiber. One is a zigzag path in a plane containing the fiber axis as shown in Fig. 11.1a. A ray that takes this path is called a *meridional ray*. The other is a helical path around the center of the fiber as shown in Fig. 11.1b. A ray that takes this path is called a *skew ray*.

Since transmission of light relies on total internal reflection, there exists a maximum acceptance angle. Light rays whose angles of incidence exceed this limit do not undergo

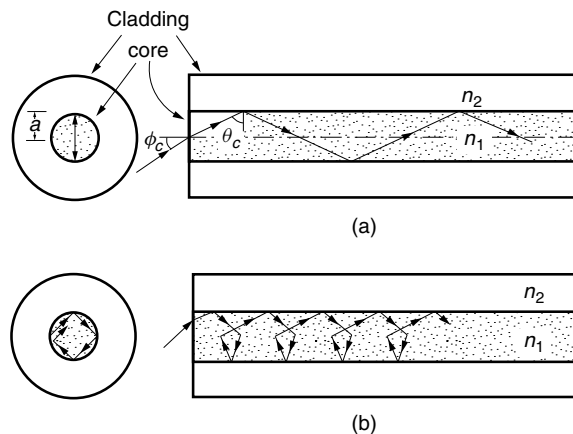


Figure 11.1 Rays in an optical fiber. (a) Meridional ray. (b) Skew ray.

total internal reflection. Referring to Fig. 11.1a, the critical angle at the core–cladding interface is

$$n_1 \sin \theta_c = n_2 \quad (11.1)$$

where n_1 and n_2 are the refractive indices of the core and cladding glasses. The corresponding cutoff incident angle ϕ_c to the end of the fiber is, from Snell's law,

$$n_0 \sin \phi_c = n_1 \sin(90^\circ - \theta_c) \quad (11.2)$$

Combining Eqs. (11.1) and (11.2) gives

$$n_0 \sin \phi_c = \sqrt{n_1^2 - n_2^2} \quad (11.3)$$

Equation (11.3) specifies the maximum incident angle to the end face of a fiber. The quantity $n_0 \sin \phi_c$ is called the *numerical aperture* (NA), and

$$\text{NA} = \sqrt{n_1^2 - n_2^2} \quad (11.4)$$

For example, the NA for a fiber with $n_1 = 1.454$ and $n_2 = 1.450$ is $\text{NA} = 0.11$, which means that the angle of incidence can be no larger than 6.3° .

When the light is coupled to the fiber using a lens, not only the angle of incidence of the converging beam but also the diameter of the incident light beam is restricted. The diameter of the converging incident light beam has to be equal to or smaller than the core diameter for efficient coupling of light to the fiber.

11.1.2 Transmission Loss of Fibers

Figure 11.2 shows the transmission loss (in dB/km) of a silica glass optical fiber with respect to wavelength λ (in μm) [4]. The general shape of the calculated loss curve is a V shape with its minimum at $\lambda = 1.55 \mu\text{m}$. In the vicinity of $1.55 \mu\text{m}$, the measured loss curve closely follows the theoretically calculated attainable limit. The region of the measured loss curve from 1.0 to $1.5 \mu\text{m}$ deviates somewhat from the calculated curve, and local minima are observed at $\lambda = 1.15$ and $1.3 \mu\text{m}$. On the left side of the V in Fig. 11.2, Rayleigh scattering is the prime contributor to the loss curve. This scattering is caused by irregularities in the fused silica glass as well as irregularities associated with the dopant used to raise the index of refraction of the core glass. No matter how slowly the glass fiber is cooled, when the glass solidifies, $1\text{--}10\text{-nm}$ -diameter irregularities in the index of refraction are incurred, and these act as sources of scattering. Scattering from a particle much smaller than the wavelength of the light is known as *Rayleigh scattering*. Rayleigh scattering is proportional to λ^{-4} , so that the amount of Rayleigh scattering decreases rapidly as λ increases.

The amount of Rayleigh scattering loss can be reduced by decreasing the dopant concentration. In fact, a fiber with a pure silica core and fluorine-doped cladding has lower loss than a fiber with a GeO_2 -doped core.

An additional loss on the left-hand side of the V curve is the tail of the electronic transition of fused silica, which occurs at $\lambda = 0.1 \mu\text{m}$ in the ultraviolet region. The amount of this loss is an order of magnitude smaller than the Rayleigh scattering loss.

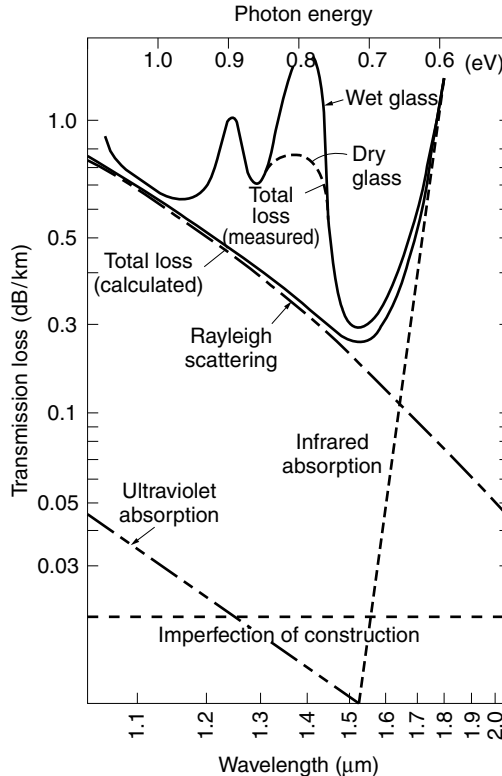


Figure 11.2 Transmission loss with wavelength. (After T. Miya et al. [4].)

Next, the loss in the right-hand side of the V curve will be explained. The right-hand side of the V curve represents the tail of the infrared absorption at $\lambda = 10 \mu\text{m}$. This absorption at $\lambda = 10 \mu\text{m}$ coincides with a vibrational transition of the Si—O lattice in the glass.

Lastly, the peak appearing at $\lambda = 1.38 \mu\text{m}$ in the measured loss curve is due to the presence of OH ion impurities. The increase in loss at $\lambda = 1.38 \mu\text{m}$ occurs because of the second harmonic of the OH ion absorption whose fundamental is located at $\lambda = 2.72 \mu\text{m}$. Absorption by the OH ion is strong, and even small amounts create a significant increase in the fiber loss. In order to remove this loss, the OH ion content has to be reduced to less than 0.1 ppb (parts per billion, 10^{-9}).

11.1.3 Loss Increase Due to Hydrogen and Gamma-Ray Irradiation

It was found that the transmission loss of an optical fiber slowly increases when it is placed in a hydrogen atmosphere. The test results at an elevated temperature are shown in Fig. 11.3a and b. The loss increase is observed over the entire wavelength range, with its maximum at $\lambda = 1.38 \mu\text{m}$. Even though the process is slow at room temperature, such deterioration threatens the life expectancy of fiber-optic communication systems, which is normally 25 years.

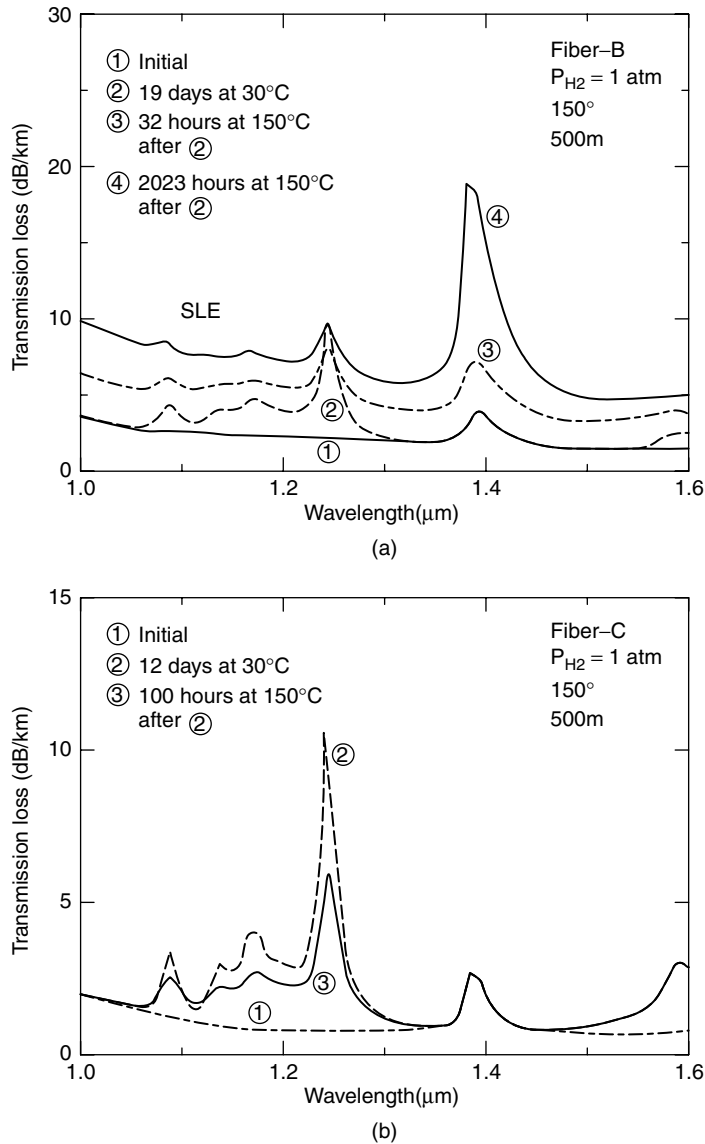
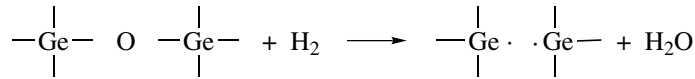


Figure 11.3 Loss increase due to hydrogen exposure for (a) a GeO₂-doped core fiber, and (b) pure SiO₂ core fiber. (After M. Kuwazuru et al. [6].)

There are two types of deterioration: one is reversible and the other is irreversible. The former does not involve a chemical reaction but the latter does. A large class of solid materials will absorb gas from the surface, albeit very small amounts of gas, by diffusion of the gas into the solid. Glass is not an exception. Vibration of the absorbed hydrogen (H₂) gas contributes to the increase in the transmission loss. Such loss, however, is removed when the fiber is removed from the hydrogen atmosphere and then its temperature is raised. The hydrogen gas boils out. This loss is still a problem as long as the fiber has to operate in the hydrogen atmosphere. Some of the

increases in loss caused by the hydrogen gas cannot be removed. These are irreversible deteriorations because they involve chemical reactions between hydrogen and the fiber core. Any chemical reaction resulting in hydroxyl (OH) formation increases the loss at $\lambda = 1.38 \mu\text{m}$. Another irreversible effect is the “short-wavelength-loss edge” (SLE) [5].

The monotonic increase toward short wavelengths is due to SLE. Because of the partial reduction,



an oxygen vacancy is created. Such a defect has a strong absorption line at 215 nm. The SLE is considered to be the tail of this strong absorption. Even when the same fiber ingredients are used, the amounts of OH ion loss and SLE vary, and it is thought that both loss mechanisms have a lot to do with defects of the molecular network [6].

The degree of increase in loss also depends on the kind of dopant in the core. Cores doped with P_2O_5 suffer the highest loss, followed by GeO_2 . The best is the pure silica core with fluorine-doped cladding. This fiber is practically immune to hydrogen deterioration [7] because it has the least defects in the molecular network.

The major source of hydrogen is the evolution of hydrogen from organic cable materials. Silicone resin evolves a large amount of hydrogen due to the excess organohydrogen polysiloxane monomer used as a hardener [8]. The amount of hydrogen evolution of UV-light-cured resin is about one-hundredth that of H_2 -rich silicone resin, and one-half that of H_2 -lean silicone resin.

Another important factor that determines the hydrogen loss is the permeability of hydrogen gas through the cabling material. Even though hydrogen may be evolved from the coating material, if hydrogen escapes from the cabling material into the atmosphere, then the hydrogen pressure, which is directly related to the degree of deterioration, is low, and no problem arises. Coatings of laminated aluminium polyethylene (LAP) have to be properly permeable to hydrogen to prevent the buildup of hydrogen pressure inside the cable.

Next, transmission loss due to gamma-ray (γ -ray) irradiation will be explained. The effects of γ -ray irradiation can be significant if the optical fiber is used within the premises of a nuclear reactor, or in any environment where there is a possibility of exposure to γ rays, such as outer space or deep-sea applications.

When γ rays strike the Si—O lattice, some atoms may become dislodged from the lattice, creating dislocation spots. The dislocation displays a strong absorption at 215 nm with a long tail [9], causing SLE. Figure 11.4 shows the attenuation of light at $\lambda = 1.3 \mu\text{m}$ when the fiber is irradiated by 10^5 rads/h of γ -ray irradiation. As soon as irradiation starts, the attenuation increases, and as soon as irradiation stops the fiber begins to recover. Figure 11.4 also shows that a fiber with a pure silica core is less susceptible to the irradiation and has superior recovery characteristics compared to a GeO_2 -doped fiber.

It is known that the effect of the γ -ray irradiation can be lessened by introducing some H_2O in the core glass, at the cost of a significant increase in the transmission loss. Figure 11.5 shows the attenuation of the fiber with respect to wavelength before and after 10^5 rads/h irradiation for one hour. Even though the attenuation increases at wavelengths shorter than $\lambda = 0.9 \mu\text{m}$, it is practically unchanged at the wavelengths longer than $\lambda = 0.9 \mu\text{m}$.

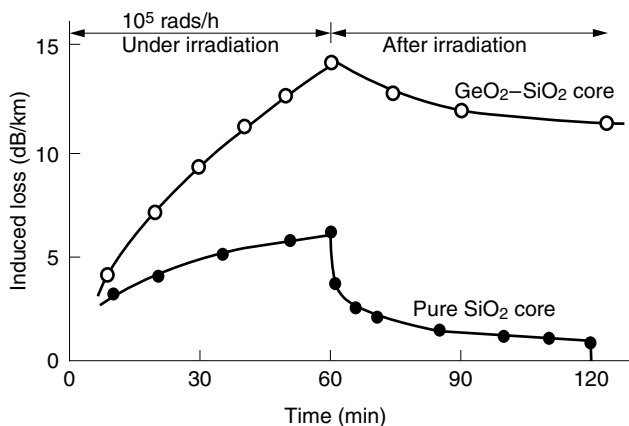


Figure 11.4 Loss increase due to γ -ray irradiation (at $\lambda = 1.3 \mu\text{m}$ and 25°C). (After I. Yoshida et al. [9].)

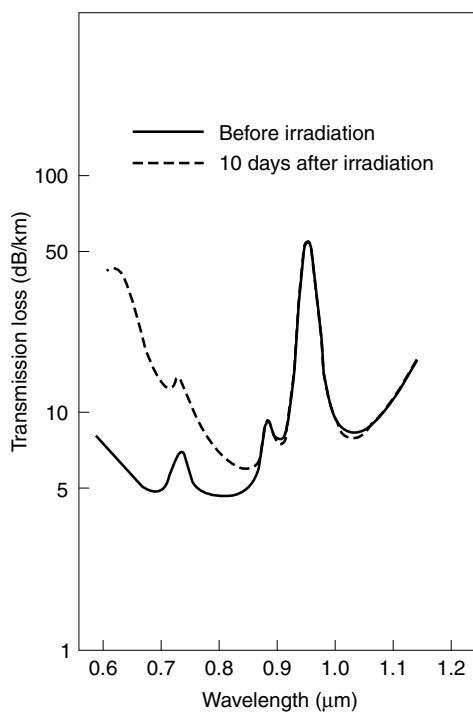


Figure 11.5 Transmission loss of a fiber containing H_2O before and after irradiation with 10^5 rads/h γ rays for one hour. (After G. Tanaka et al. [7].)

For most applications, increased fiber loss due to radiation is undesirable, but in the biomedical field [10], this property has been used to advantage. A fiber sensor has been constructed for monitoring the radiation dose in close vicinity to the site of the radiation therapy. A short length of radiation-sensitive optical fiber such as lead glass fiber or Ge-doped SiO_2 fiber is connected to a radiation-resistant fiber and is inserted

into the body of the patient. The end of the sensor has a mirror and the radiation dose is found by measuring the reflected light power.

11.1.4 Dispersion

Next to the fiber loss, the capacity of information transmission is an important consideration in designing a fiber-optic communication system. The dispersion of the fiber essentially determines the maximum bit rate or modulation frequency that can be attained. There are three types of dispersion:

1. Mode dispersion.
2. Material dispersion.
3. Waveguide dispersion.

Variation in propagation time among different modes creates mode dispersion. If the source were perfectly monochromatic, then mode dispersion would be the only dispersion with which to contend. In reality, all sources, especially when modulated, emit light over a spread of optical frequencies, and the frequency spread of the source leads to other types of dispersion. The variation in propagation time due to the wavelength dependence of the refractive index creates material dispersion. The wavelength dependence of the propagation pattern causes waveguide dispersion.

11.1.5 Mode Dispersion

In the case of the slab optical guide treated in Chapter 9, the mode pattern was considered as a standing-wave pattern made of two component waves propagating in a zigzag path. The component wave of the lowest order mode propagated almost straight, whereas that of the higher order mode propagated with a larger angle of zigzag. The same argument holds for a step-index optical fiber. When a pulse of light is injected into the fiber end, as shown in Fig. 11.6, the pulse energy is partitioned among all possible discrete angles δ_m , where $\delta_0 \doteq 0$ corresponds to the lowest order mode and $\delta_m = \delta_c$ corresponds to the highest order mode. The distance of travel for the lowest order mode is the shortest, while that of the highest order mode is the longest. There is a spread in the arrival time for the pulse energies transmitted in different modes. Such a spread seen in the received pulse is called *mode dispersion*. The time τ needed for the light to travel a unit distance is called the *group delay*, and dispersion

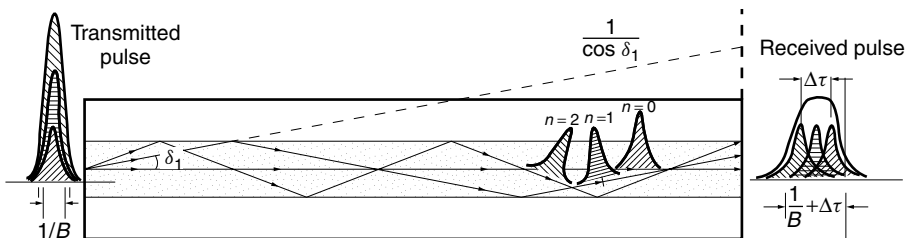


Figure 11.6 Explanation of mode dispersion. Component waves take different zigzag paths. The higher order mode components take a longer time to reach the receiver than the lower order mode components, creating a spread in arrival time.

is expressed as the spread $\Delta\tau$ of the group delay. As shown in Fig. 11.6, the total length of the zigzag propagation for the first mode is identical to the path shown by the dashed line. The spread $\Delta\tau$ due to mode dispersion, therefore, is

$$\Delta\tau = \frac{n_1}{c} \left(\frac{1}{\cos \delta_m} - 1 \right) \quad (11.5)$$

where δ_m is the zigzag angle of the highest order mode. The path of the lowest order mode is assumed a straight line. Only meridional rays are considered. Using Snell's law at the entrance, the numerical aperture is expressed as

$$\text{NA} = n_1 \sin \delta_m \quad (11.6)$$

Equations (11.5) and (11.6) combined with the assumption that δ_m is very small gives

$$\Delta\tau = \frac{1}{2cn_1} (\text{NA})^2 \quad (11.7)$$

It is generally accepted that when the spread $\Delta\tau$ of the light pulse becomes wider than 70% of the bit period $1/B$ seconds, where B is the number of bits per second of the digital signal, information transmission becomes unreliable (see Section 16.6.5). From Eq. (11.7) the maximum bit rate of a multimode fiber is approximately

$$B = 1.4 \frac{cn_1}{(\text{NA})^2} \quad (11.8)$$

For a multimode fiber with $n_1 = 1.55$ and $n_2 = 1.54$, we have, from Eq. (11.4), $\text{NA} = 0.176$. The information capacity for a transmission of one kilometer is $B = 21$ (Mb/s).

Equation (11.8) is valid for a step-index fiber, that is, a fiber whose refractive index profile is a step function. One obvious way to eliminate mode dispersion is to use a fiber in which, only one mode is excited and the mode dispersion is completely removed. Such a fiber is called a single-mode fiber or monomode fiber.

For some applications, single-mode fiber is the preferred choice, despite the more critical alignment tolerances. Just how small is the core of a single-mode fiber? Some calculations are presented here to answer that question. The number of possible modes in a slab guide was determined by the normalized thickness in Section 9.3. Similarly, as will be detailed later, the number of modes in an optical fiber is determined by the normalized radius V of the core

$$V = ka\sqrt{n_1^2 - n_2^2} \quad (11.9)$$

According to the calculation in Eq. (11.107), single-mode propagation is obtained when

$$V < 2.4$$

Equation (11.9) is rewritten using Eq. (11.4) as

$$V = \frac{2\pi}{\lambda} a \cdot (\text{NA}) \quad (11.10)$$

In order to reduce V , there is a choice of either reducing the core radius or the numerical aperture (NA). Choosing too small a value for the radius a makes translational alignment of the source beam too critical. On the other hand, too small a value of NA makes the angular alignment of the source beam too critical. The radius of a single-mode fiber is normally chosen around $a = 4.5\text{--}5\text{ }\mu\text{m}$.

11.1.6 Material and Waveguide Dispersions

Dispersion of an optical fiber is not limited to mode dispersion. Even a single-mode fiber suffers from two additional dispersions. Associated with the light spectrum is a finite wavelength (frequency) bandwidth, either because of signal modulation or characteristics of the light source, and the wavelength (frequency) dependence of the group delay causes the additional dispersion. Glass materials change their index of refraction with wavelength, as shown in Fig. 11.7 (see boxed note). The variation of the index of refraction causes not only a spread in the group velocity of the component waves but also a variation in the zigzag pattern. Dispersion due to the spread of the index of refraction is called *material dispersion*. Dispersion due to the variation in the zigzag pattern is called *waveguide dispersion*.

Material dispersion, waveguide dispersion, and the sum of the two are all plotted with respect to wavelength in Fig. 11.9. In this figure, the dispersion parameter, which has units of ps/(nm·km), is used as a practical unit for representing the dispersion. This unit means the number of picoseconds of spread in arrival time for a source wavelength spread of 1 nm and a fiber length of 1 kilometer. For example, for a pulse whose carrier frequency is $\lambda = 1.55\text{ }\mu\text{m}$, the dispersion parameter D from the graph in Fig. 11.9 is $D = 16.7$. If this pulse has a wavelength band of 1.5 nm and travels 20 km, the expected spread of the arrival time is $(16.7)(1.5)(20) = 501\text{ ps}$.

Material dispersion increases from a negative quantity to a positive quantity with wavelength. At $\lambda = 1.27\text{ }\mu\text{m}$, the curve crosses the horizontal axis and the material dispersion becomes zero, leaving only the waveguide dispersion as well as the mode dispersion.

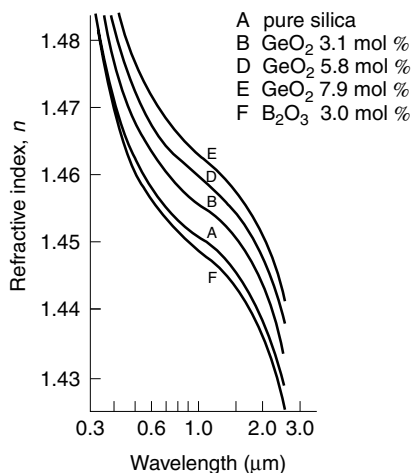


Figure 11.7 Refractive index of doped fused silica and pure fused silica. (After S. Kobayashi et al. [11].)

There is a formula that very nicely fits the wavelength dependence of the index of refraction of pure silica glass [11]:

$$n^2 = 1 + \sum_{i=1}^3 \frac{a_i \lambda^2}{\lambda^2 - b_i} \quad (11.11)$$

with

$$\begin{aligned} a_1 &= 0.6961663 & b_1 &= 0.004629148 \\ a_2 &= 0.4079426 & b_2 &= 0.01351206 \\ a_3 &= 0.8974994 & b_3 &= 97.934062 \end{aligned} \quad (11.12)$$

This formula is known as *Sellmeier's formula*. As shown in Fig. 11.8, the measured index of refraction of the glass has two regions of steep slope in the range of 0.04–40 μm . The steep slope in the region of 7–15 μm is due to the dispersion caused by vibration of the Si—O lattice in the crystal. The electronic transition bands around 0.1 μm are responsible for the steep slope in the region of 0.07–0.15 μm . Each term

$$\frac{a_i \lambda^2}{\lambda^2 - b_i} \quad (11.13)$$

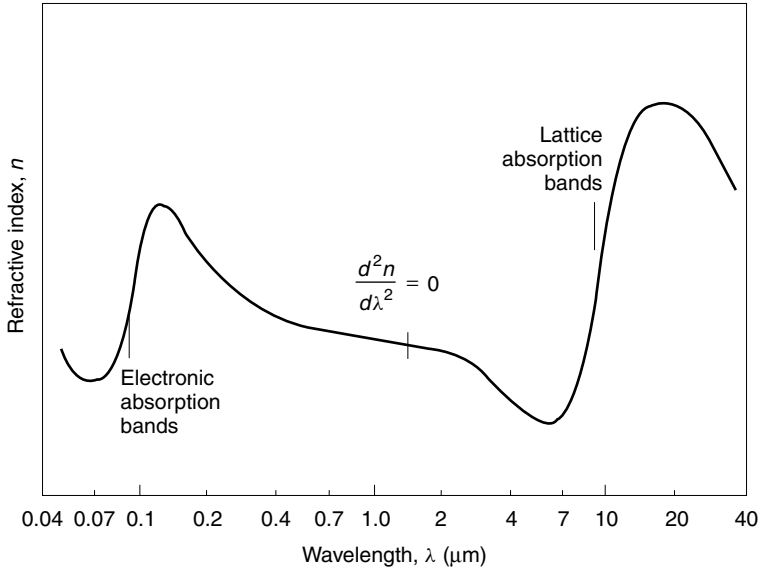


Figure 11.8 Refractive index variation of fused silica. (After S. R. Nagel.)

corresponds to a peak at $\lambda = \sqrt{b_i}$, and the sum of the terms nicely represents the index of refraction, except in very close proximity to $\lambda = \sqrt{b_i}$, where the associated term becomes infinite. Figure 11.7 was obtained by expanding the vertical scale in the region between 0.3 and 3 μm .

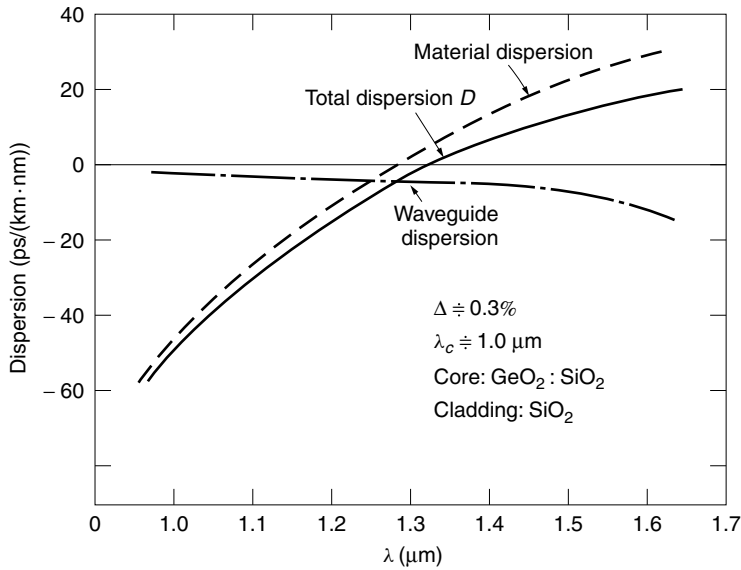


Figure 11.9 Dispersion of a single mode fiber. (After D. B. Keck [12].)

The waveguide dispersion remains a small negative quantity throughout the region shown in Fig. 11.9 [12]. At $\lambda = 1.32 \mu\text{m}$, the waveguide dispersion cancels the material dispersion, and the single-mode optical fiber becomes completely free from these two dispersions.

As seen from Fig. 11.9, the wavelength for dispersion-free transmission can be shifted toward a longer wavelength, more specifically to $\lambda = 1.55 \mu\text{m}$, if the magnitude of the waveguide dispersion is somehow increased. An optical fiber whose dispersion-free wavelength is shifted to the wavelength of lowest loss can have both the merits of lowest loss and no dispersion. Such a fiber is called a *dispersion-shifted fiber* and is discussed further in Section 11.7.

11.1.7 Various Kinds of Optical Fibers

A survey will be made of the various kinds of optical fibers in this section. A brief description of features will be given for each type. A standard cladding diameter of $125 \mu\text{m}$ is assumed unless otherwise specified.

11.1.7.1 Multimode Step-Index Fiber

The geometry of the multimode step-index fiber is shown in Fig. 11.10a. The core diameter is $50 \mu\text{m}$, and the refractive index difference is $\Delta = 0.5\text{--}1.0\%$. The normalized radius is $V \doteq 30$, and the number of modes is on the order of hundreds. The advantage of this fiber is the ease of coupling to a source or connecting to another fiber because of the large core diameter and large NA value. But this fiber has a limited capacity for information transmission due to mode dispersion and is used primarily for short-distance communication. The capacity (bandwidth–length product) is about 65 (Mb/s)·km with $\text{NA} = 0.1$.

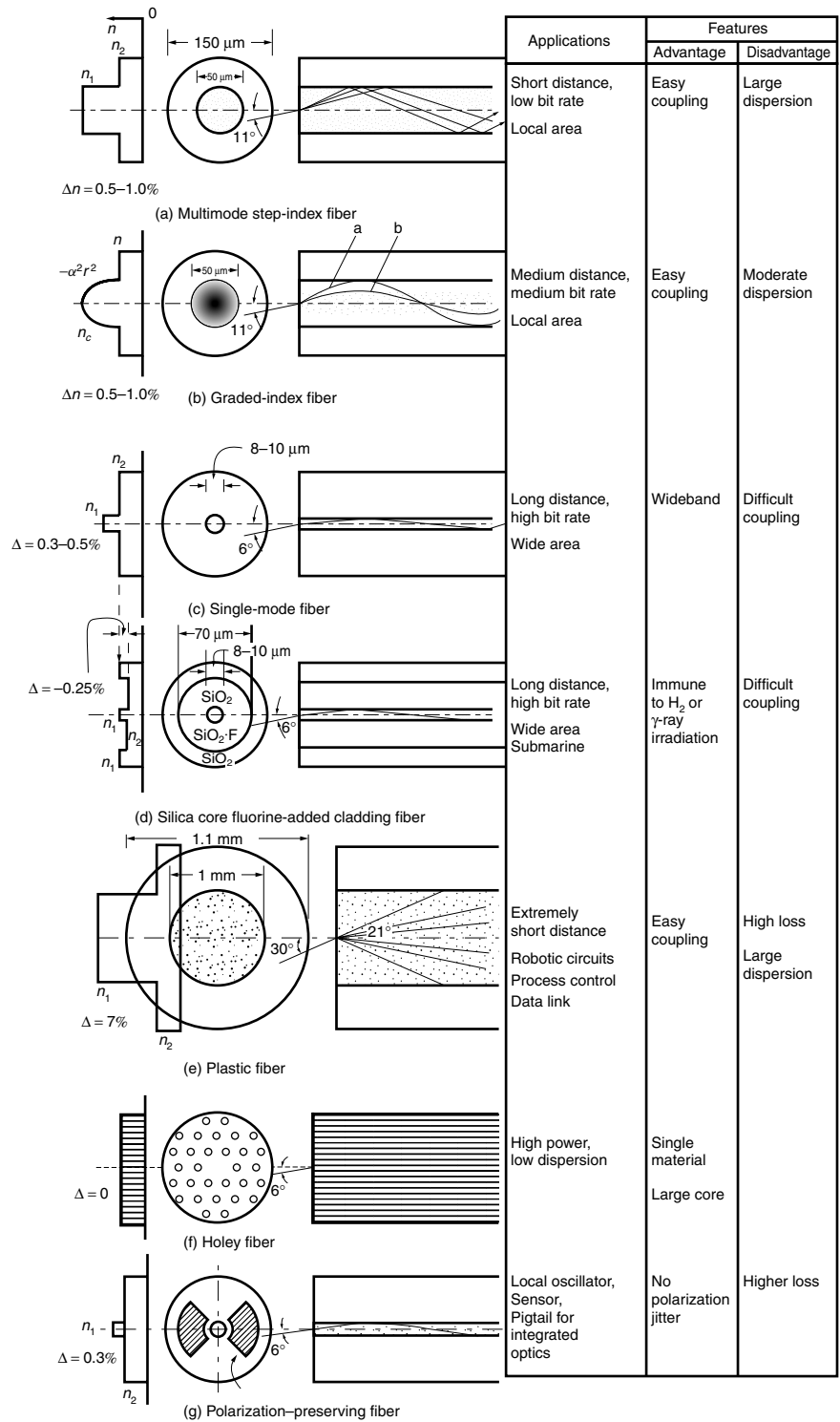


Figure 11.10 Various kinds of optical fibers.

11.1.7.2 Multimode Graded-Index Fiber

A quadratic refractive index distribution is employed as shown in Fig. 11.10b in order to reduce the dispersion. Compare the travel paths of two sinusoidal meridional rays a and b in the figure. Even though the total travel path of ray a is longer, this ray travels mostly in an outer region where the index of refraction is lower and hence the velocity is higher. On the other hand, the travel path of ray b is shorter but it travels in the center region where the index of refraction is higher and hence the velocity is lower. As a result, the difference between the travel times of ray a and b is minimized in the graded index fiber. The dispersion of the graded index fiber is much smaller than that of the multimode step index fiber.

The graded-index fiber retains the coupling ease of the multimode step-index fiber, with the added bonus of a much larger capacity for information transmission, up to 10 (Gb/s)·km. Both the step-index multimode fiber and the graded-index multimode fiber are unsuitable for coherent optical communication systems, or any other system where the phase and state of polarization are important. Because of the hundreds of modes present in these fibers, the phase and state of polarization of the light change in a highly unpredictable manner.

11.1.7.3 Single-Mode Fiber

The geometry of a single mode fiber is shown in Fig. 11.10c. The core diameter is reduced to 8–10 μm , and $\Delta = 0.3\text{--}0.5$, so that the normalized radius V of the fiber in Eq. (11.9) is smaller than the cutoff $V = 2.4$ of the mode that is the next higher mode from the dominant mode. The advantage and disadvantage of the single-mode fiber are reversed compared to the multimode fiber. Coupling is difficult in the single-mode fiber, but the information transmission capacity is significantly larger than that of the multimode fiber. Unlike the multimode fiber, phase information can be transmitted. Even though the state of polarization is subject to change during transmission, it can be compensated for at the receiver (see Section 12.9.1). This fiber is suitable for coherent communication.

11.1.7.4 Dispersion-Shifted Fiber

The dispersion-shifted fiber is not only nominally free from dispersion, but also the wavelength of operation is at $\lambda = 1.55 \mu\text{m}$, where transmission loss is least. The dispersion of the fiber is removed by choosing a refractive index distribution such that waveguide dispersion cancels material dispersion at $\lambda = 1.55 \mu\text{m}$.

Transmission loss is about 0.2 dB/km and the practical limit on the capacity of information transmission is about a (Tb/s)·km.

The refractive index distribution is either one large peak of $\Delta = 0.6\text{--}0.9$, or a concentric step modulation in the cladding layer. The former is shown in Fig. 11.34 and the latter in Fig. 11.35. The physical dimension of the fiber is more or less the same as that of the single-mode fiber shown in Fig. 11.10c. Dispersion-shifted fibers have a larger bending loss than ordinary single-mode fibers due to less confinement of the light within the core.

11.1.7.5 Silica Core Fluorine-Added Cladding Fiber

The cladding glass is normally pure SiO_2 . Germanium dioxide (GeO_2) is usually used to raise the refractive index of the core glass with respect to that of the cladding glass. The inclusion of GeO_2 is an additional inhomogeneity in the core and is deemed to increase the transmission loss of the fiber. If, however, pure SiO_2 is used in the core and the refractive

index of the cladding is lowered by adding fluorine (see Fig. 11.10d), the transmission loss of the fiber is reduced. The transmission loss of such a fiber is 0.154 dB/km at $\lambda = 1.55 \mu\text{m}$.

An even more significant advantage of the silica core fluorine-added cladding fiber is that it is less susceptible to the loss associated with exposure to hydrogen atmosphere or γ -ray irradiation, as already mentioned in Section 11.1.3.

11.1.7.6 Plastic Fiber

This fiber is made out of low-transmission-loss plastic material. Being made of plastic, the diameter of the core can be as large as 1–2 mm. A fiber with such a large diameter would shatter if it were made of glass when it is bent. The plastic fiber not only has a large diameter but also has a large NA value of 0.5, which means $\phi_c = 30^\circ$. Because of the large NA, the plastic fiber can easily be coupled to a light source. The disadvantages of this fiber are a high transmission loss and a large dispersion. It is primarily used for short-distance communication. Figure 11.10e shows the geometry of a plastic fiber. Plastic fiber whose core is made of polymethyl methacrylate (PMMA) and whose cladding is made of fluorinated alkyl methacrylate copolymer is useful in the region of $\lambda = 0.6\text{--}0.8 \mu\text{m}$ and the minimum transmission loss is 20 dB/km at $0.68 \mu\text{m}$ [13].

11.1.7.7 Multi-Ingredient Fiber

The melting point of fused silica is around 1900°C . Light doping with one or two of the commonly used dopants does not affect the melting point of fused silica significantly. Glass that is used for fabricating lenses, however, contains many kinds of metal oxides, such as Na_2O , MgO , B_2O_3 , Tl_2O , CaO , GeO_2 , and Li_2O . The melting point of such glass is lower and is around 1200°C . The lower melting point makes it possible to fabricate an optical fiber by pulling it out of a nozzle at the bottom of a double crucible, where the inner crucible is filled with molten core glass, and the outer crucible is filled with molten cladding glass (see Fig. 11.45). The fiber is made directly from the molten material into a finished fiber, and not only is the fabrication cost lower, but the fiber can be endlessly long. Another merit of this fiber is that the difference in the refractive indices of the core and cladding can be made large and the NA value can be as high as $\text{NA} = 0.5$ for easy coupling to the source.

The transmission loss of such a fiber is at its lowest value of 4 dB/km near $\lambda = 0.8 \mu\text{m}$. Fiber of this kind is used primarily for short-distance optical communication.

11.1.7.8 Holey Optical Fiber (HF)

Holey optical fiber (HF) is a single material fiber with a periodic or aperiodic array of circular [14,15] or elliptical [16] air holes running in the axial direction of the optical fiber. The presence of air holes reduces the effective index of refraction of the material. The effective refractive index difference can be achieved from a single material.

Holey optical fiber is fabricated from a preform. The preform is assembled by stacking hexagonally shaped silica rods whose centers have been bored to produce air holes. The fused stacked silica rods are repeatedly drawn through a furnace tower at 2000°C to achieve the desired air hole dimensions of $0.2\text{--}1.2 \mu\text{m}$ in diameter.

As shown in Fig. 11.10f, there are no holes in the central region, which acts as the core. The surrounding region contains the holes and acts as the cladding.

This type of fiber is single mode over an exceptionally wide wavelength range from 458 to 1550 nm , as determined by measuring the numerical aperture (NA). The NA of the fiber was determined by measuring ϕ_c , where $\text{NA} = \sin \phi_c$ in Fig. 11.1. It was found that the value of NA almost linearly increases with wavelength. ($\text{NA} = 0.13$ at

The single-mode excitation was confirmed by observing the field pattern projected onto a distant screen. The field pattern was not affected either by bending the fiber or changing the launching condition into the fiber. If more than one mode were excited, the projected field pattern would change due to the change in the relative phase between the excited modes when the fiber is disturbed.

$\lambda = 458$ nm, and $NA = 0.36$ at $\lambda = 1,550$ nm.) Thus, the value of NA/λ , hence V , given by Eq. (11.10) maintains an almost constant value with wavelength, and the HF is single mode for such a wide range.

The holey fiber remains single mode even with large core dimensions. For example, a $23\text{ }\mu\text{m}$ core remains single mode at $\lambda = 458\text{ }\mu\text{m}$. An advantage of this type of fiber is that high-power light can be transmitted through the large-core-area fiber without concerns about the nonlinearity effects of the core material.

11.1.7.9 Polarization-Preserving Fiber

A polarization-preserving fiber is used in applications where the stability of the state of polarization is important, such as in coherent optical communication systems or optical fiber sensors. A single-mode optical fiber is actually dual mode in the sense that it is capable of supporting two orthogonal polarization modes. In a cylindrically symmetric optical fiber, perturbations such as bends and stresses on the fiber will cause coupling between the two nearly degenerate polarization modes, with the result that the output state of polarization fluctuates. Building a large asymmetry into the fiber reduces the coupling between polarization modes, so that if only one polarization mode is excited at the input, this state of polarization is preserved during transmission through the fiber.

If the effective index of refraction is raised diametrically, then the two polarization modes are orthogonally linearly polarized—one parallel to this direction, and the other perpendicular to it. Incident linearly polarized light aligned to either of these directions will be preserved.

Polarization-preserving fiber is categorized in Fig. 11.11 by the way the asymmetry of the effective index is generated. The first category relies on stress-applying members (SAM) to produce a stress-induced asymmetry of the refractive index. The second category makes use of geometric asymmetry [17], or uses an additional material with a refractive index different from the core or cladding refractive index. An example of a fiber belonging to the first category is the bow-tie fiber. The heat expansion coefficient of the bow-tie-shaped stress member is higher than that of the cladding glass. When the fiber solidifies as it is cooled, an asymmetric tensile stress is built up in the fiber, and this establishes an asymmetric distribution of the index of refraction. The Panda fiber and the elliptical SAM fiber shown on the left-hand side of Fig. 11.11 also belong to this category.

Examples of polarization-preserving fiber belonging to the second category are shown on the right-hand side of Fig. 11.11. The elliptical core fiber makes use of a geometric asymmetry, while the side pit and side tunnel fibers make use of regions with a third index of refraction.

The direction of the increased effective index of refraction is called the slow axis, and the direction of the decreased effective index of refraction is called the fast axis. The direction of the slow axis of both the bow-tie and Panda fibers is in the direction of the stress members.

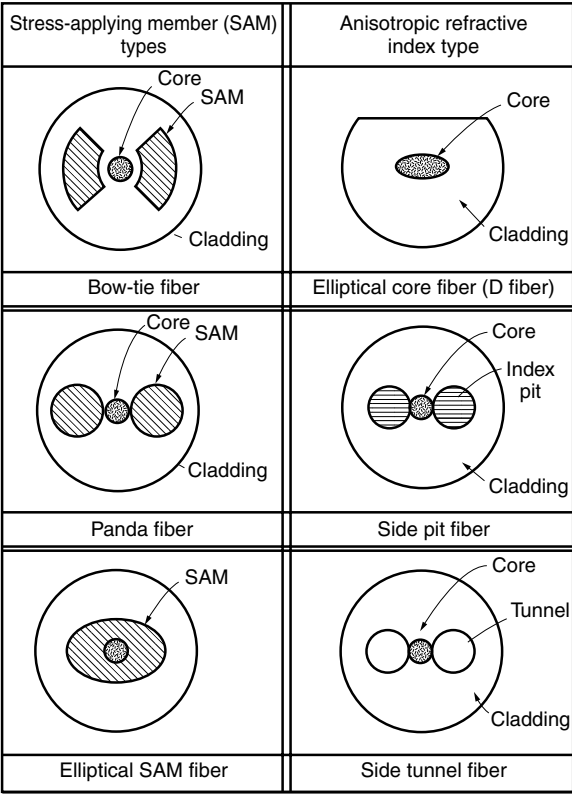


Figure 11.11 Various types of polarization-preserving fiber.

The performance of polarization-preserving fibers is measured by the amount of crosstalk, which is the power received polarized in the direction of the fast axis when linearly polarized light is incident with its polarization parallel to the direction of the slow axis. Crosstalk is typically less than -30 dB/km with a transmission loss of about 2.0 dB/km.

11.1.8 Optical Fibers Other Than Silica Based Fibers

The loss curve of the silicon dioxide (SiO_2)-based fiber was shown in Fig. 11.2. It is V shaped, with the left side of the V dominated by Rayleigh scattering loss, and the right side of the V dominated by the infrared absorption associated with the vibration of the Si—O network. Searches have been made for a material whose vibration frequency of the molecular network is lower than that of the Si—O network, so that the point of the intercept would be lower. If such a material could be found, it might be possible to manufacture a fiber with better transmission characteristics than silicon dioxide.

Figure 11.12 shows the infrared absorption curves due to vibration for various materials. In the order of decreasing vibration frequency, they are the metal fluorides like LiF, MgF_2 , and fused BeF_2 ; the metal chlorides like NaCl, ZnCl_2 , and KCl; and metal halides like KBr and TlBr [18].

Besides the transmission loss, the degree of difficulty in purifying the material, the flexibility, the degree of dispersion, and the availability of sources have to be taken into

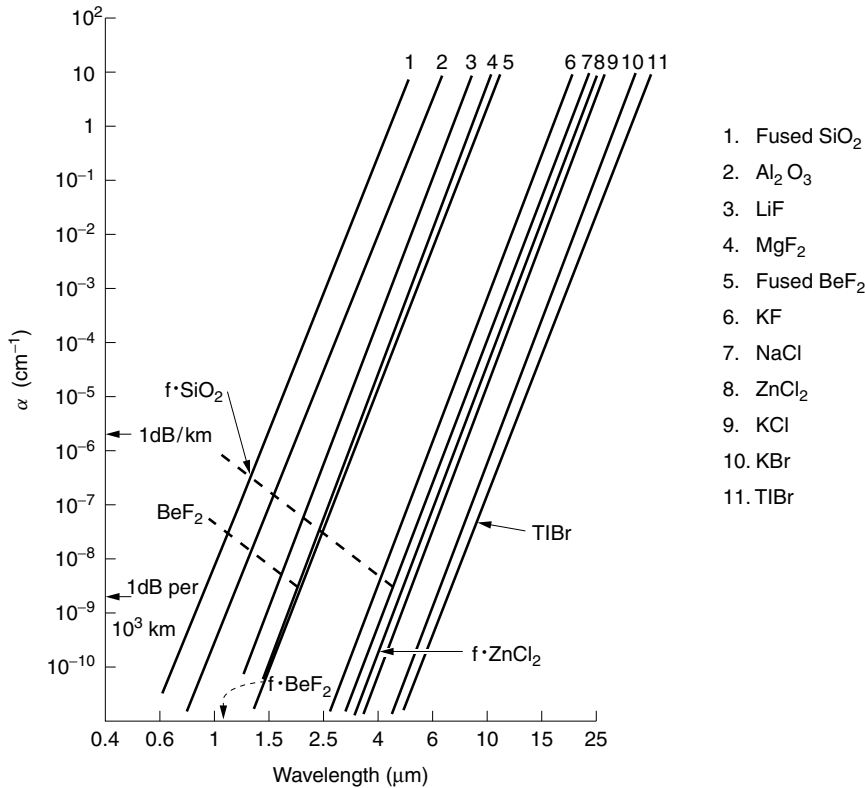


Figure 11.12 Infrared absorption due to lattice vibration for various materials. The arrows indicate the positions of λ_c for the various materials. The upper dashed line indicates scattering-loss values for fused SiO_2 ; the lower, the predicted values for BeF_2 . (After L. G. Van Uitert and S. H. Wemple [18].)

consideration to find new materials for fiber-optic communications. Fiber materials like the metal halides whose minimum loss matches the wavelength of the CO_2 laser have a special significance outside communication as a means of transmitting the energy for a CO_2 laser surgery tool.

11.2 THEORY OF STEP-INDEX FIBERS

Earlier sections of this chapter concentrated on characterization of optical fibers from a practical viewpoint, but the time has now come to face the reality of solving Maxwell's equations to obtain more rigorous expressions. Topics to be covered in this section include hybrid modes with their cutoff conditions, the linearly polarized (LP) modes representation, distortion of a light pulse during transmission inside an optical fiber, and the principles of dispersion-shifted fibers.

11.2.1 Solutions of the Wave Equations in Cylindrical Coordinates

Figure 11.13 shows the geometry of a step-index fiber with a core radius a and cladding radius b . Practically speaking, b is large enough that the evanescent field is negligible, and the assumption of $b = \infty$ is made.

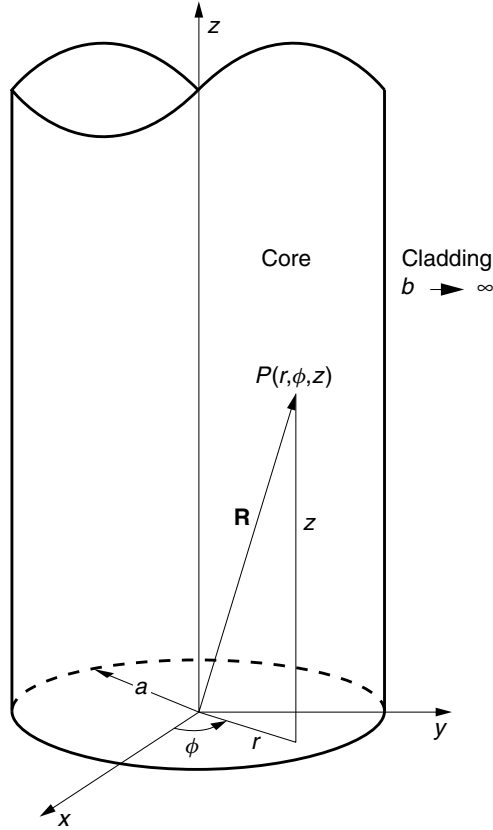


Figure 11.13 Optical fiber in a cylindrical coordinate system.

Since it is easiest to choose a coordinate system that matches the fiber geometry, cylindrical coordinates will be used. The wave equations to be solved are

$$\nabla^2 \mathbf{E} + (nk)^2 \mathbf{E} = 0 \quad (11.14)$$

$$\nabla^2 \mathbf{H} + (nk)^2 \mathbf{H} = 0 \quad (11.15)$$

where

$$n = \begin{cases} n_1 & \text{inside the core} \\ n_2 & \text{inside the cladding} \end{cases}$$

\mathbf{E} and \mathbf{H} in cylindrical coordinates are

$$\mathbf{E} = E_r \hat{\mathbf{r}} + E_\phi \hat{\boldsymbol{\phi}} + E_z \hat{\mathbf{z}} \quad (11.16)$$

$$\mathbf{H} = H_r \hat{\mathbf{r}} + H_\phi \hat{\boldsymbol{\phi}} + H_z \hat{\mathbf{z}} \quad (11.17)$$

The differential operators in cylindrical coordinates are more complicated than those in rectangular coordinates. The wave equation, Eq. (11.15), in cylindrical coordinates is

$$\begin{aligned}
\nabla^2 \mathbf{E} + (nk)^2 \mathbf{E} = & \left(\nabla^2 E_r - \frac{2}{r^2} \frac{\partial E_\phi}{\partial \phi} - \frac{E_r}{r^2} + (nk)^2 E_r \right) \hat{\mathbf{r}} \\
& + \left(\nabla^2 E_\phi + \frac{2}{r^2} \frac{\partial E_r}{\partial \phi} - \frac{E_\phi}{r^2} + (nk)^2 E_\phi \right) \hat{\boldsymbol{\phi}} \\
& + (\nabla^2 E_z + (nk)^2 E_z) \hat{\mathbf{z}} = 0
\end{aligned} \tag{11.18}$$

where the Laplacian operator is

$$\nabla^2 = \frac{1}{r} \frac{\partial}{\partial r} \left(r \frac{\partial}{\partial r} \right) + \frac{1}{r^2} \frac{\partial^2}{\partial \phi^2} + \frac{\partial^2}{\partial z^2} \tag{11.19}$$

Note that in Eq. (11.18), the $\hat{\mathbf{r}}$ component contains both E_r and E_ϕ and likewise with the $\hat{\boldsymbol{\phi}}$ component, but the $\hat{\mathbf{z}}$ component contains only E_z . Because of this fact, the z component is first solved and then the other components E_r and E_ϕ will be obtained directly from Maxwell's equation.

11.2.2 Expressions for the E_z and H_z Components

Equation (11.18) being a vector equation, each component has to vanish individually in order for the vector sum of the components to be zero. Using Eq. (11.19), the z component of Eq. (11.18) is expressed as

$$\frac{1}{r} \frac{\partial}{\partial r} \left(r \frac{\partial E_z}{\partial r} \right) + \frac{1}{r^2} \frac{\partial^2 E_z}{\partial \phi^2} + \frac{\partial^2 E_z}{\partial z^2} + (nk)^2 E_z = 0 \tag{11.20}$$

The differential equation, Eq. (11.20), is solved by the method of separation of variables. The component E_z can be expressed as a product of three functions, each individual functions of r , ϕ , and z only:

$$E_z = F(r)\Phi(\phi)Z(z) \tag{11.21}$$

Inserting Eq. (11.21) into (11.20) gives

$$F''\Phi Z + \frac{1}{r}F'\Phi Z + \frac{1}{r^2}F\Phi''Z + F\Phi Z'' + (nk)^2 F\Phi Z = 0 \tag{11.22}$$

Dividing both sides of Eq. (11.22) by $F\Phi Z$ gives

$$\begin{aligned}
\left[\frac{F''}{F} + \frac{1}{r} \frac{F'}{F} + \frac{1}{r^2} \frac{\Phi''}{\Phi} + (nk)^2 \right] + \frac{Z''}{Z} &= 0 \\
\beta^2 &- \beta^2 = 0
\end{aligned} \tag{11.23}$$

The functions inside the square brackets of Eq. (11.23) are functions of both r and ϕ , but the last term is a function of z only.

Since Eq. (11.23) has to be zero regardless of the combination of r , ϕ , and z , or in other words, since Eq. (11.23) must hold for all points in space, the value inside

the square brackets and the last term have to be individually constant, and the sum of these constants has to be zero. If one defines the value in the square brackets to be β^2 ,

$$\frac{F''}{F} + \frac{1}{r} \frac{F'}{F} + \frac{1}{r^2} \frac{\Phi''}{\Phi} + (nk)^2 = \beta^2 \quad (11.24)$$

then the last term has to be $-\beta^2$:

$$\frac{Z''}{Z} = -\beta^2 \quad (11.25)$$

Rewriting Eq. (11.24) gives

$$\left[r^2 \frac{F''}{F} + r \frac{F'}{F} + ((nk)^2 - \beta^2)r^2 \right] + \frac{\Phi''}{\Phi} = 0 \quad (11.26)$$

The function inside the square brackets depends solely on r and the last term is a function solely of ϕ . Similarly, these can be separated by putting the value of the bracketed terms as ν^2 and the last term as $-\nu^2$.

$$\frac{\Phi''}{\Phi} = -\nu^2 \quad (11.27)$$

and

$$F'' + \frac{1}{r} F' + [(nk)^2 - \beta^2]F = \frac{\nu^2}{r^2} F \quad (11.28)$$

For large r , Eq. (11.28) can be approximated as

$$F'' + [(nk)^2 - \beta^2]F = 0 \quad (11.29)$$

The solution of Eq. (11.29) depends on the sign of $[(nk)^2 - \beta^2]$. If it is positive, the solution for large r is sinusoidal, and if it is negative, the solution is either an exponential increase or an exponential decay at large r . The solution of Eq. (11.28) is similarly influenced by the sign of $[(nk)^2 - \beta^2]$. This suggests that in the cladding region $[(nk)^2 - \beta^2]$ should be negative and in the core it should be positive.

With the assumption of Eq. (11.21), the differential Eq. (11.20) finally becomes

$$Z'' + \beta^2 Z = 0 \quad (11.30)$$

$$\Phi'' + \nu^2 \Phi = 0 \quad (11.31)$$

$$F'' + \frac{1}{r} F' + [(nk)^2 - \beta^2]F - \frac{\nu^2}{r^2} F = 0 \quad (11.32)$$

There is more than one type of solution for each differential equation given by Eqs. (11.30)–(11.32). Some solutions are sinusoidal, while others are exponential. The selection is made according to physical considerations. The differential equations for the core and cladding regions are solved separately, and the boundary conditions between the two regions are matched by adjusting the coefficients.

11.2.2.1 Solutions in the Core Region

First, the solutions inside the core region are considered.

$$Z(z) = ae^{j\beta z} + be^{-j\beta z} \quad (11.33)$$

$$\Phi(\phi) = ce^{j\nu\phi} + de^{-j\nu\phi} \quad (11.34)$$

or

$$\Phi(\phi) = c' \cos \nu\phi + d' \sin \nu\phi \quad (11.35)$$

and lastly the solution of Eq. (11.32) is considered. Since sinusoidal-like variation rather than exponential variation in r is desired inside the core, a positive value of $K^2 = [(nk)^2 - \beta^2]$ is selected.

$$F(r) = eJ_\nu(Kr) + fN_\nu(Kr) \quad (11.36)$$

where

$$K^2 = (n_1 k)^2 - \beta^2 \quad (11.37)$$

$$n = n_1 \quad (11.38)$$

Equation (11.33) consists of forward and backward waves. For the most part, fibers are reciprocal. There do exist some nonreciprocal effects that are employed in certain fiber sensors, but these are unusual. Reciprocity means that, coupling conditions being equal, it does not matter which end of the fiber is connected to the source. It is sufficient to choose one term from the right-hand side of Eq. (11.33). There is a choice between Eq. (11.34) and Eq. (11.35). Equation (11.34) represents two skew rays that are rotating in opposite senses. Mode patterns are standing waves generated by oppositely winding skew rays and both terms in Eq. (11.34) are needed. Equations (11.34) and (11.35) with the proper selection of c , c' , d , and d' are equivalent. There is, however, a restraint in choosing the value of ν . The location of ϕ and $\phi + 2\pi$ are the same, and

$$\Phi(\phi) = \Phi(\phi + 2\pi) \quad (11.39)$$

has to be satisfied. The requirement is that ν is an integer.

$J_\nu(Kr)$ and $N_\nu(Kr)$ are respectively, the ν th order Bessel function of the first kind and the Bessel function of the second kind. The curves of $N_\nu(x)$ are shown in Fig. 11.14. $J_\nu(Kr)$ will be described later in Fig. 11.16. $N_\nu(Kr)$ becomes negative infinity at $r = 0$ and physically cannot be accepted, and f in Eq. (11.36) has to be zero.

Both **E** and **H** satisfy the same kind of wave equations, Eqs. (11.14) and (11.15). In the core region $r < a$, E_z and H_z are given by

$$E_z = AJ_\nu(Kr)e^{j\beta z + j\nu\phi} \quad (11.40)$$

$$H_z = BJ_\nu(Kr)e^{j\beta z + j\nu\phi} \quad (11.41)$$

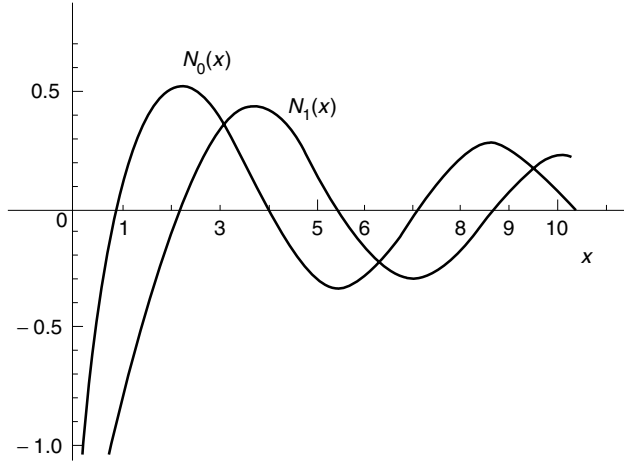


Figure 11.14 Zero- and first-order Bessel functions of the second kind.

Alternatively, the solutions could be written as

$$E_z = J_\nu(Kr) \cos(\nu\phi) e^{j\beta z} \quad (11.42)$$

$$H_z = J_\nu(Kr) \sin(\nu\phi) e^{j\beta z}$$

However, when the real part is taken at the end to obtain the final field expressions, the results are the same.

11.2.2.2 Solutions in the Cladding Region

Next, the field in the cladding region will be found. The type of solution suitable for the cladding region is one where the value of the function rapidly decreases with an increase in r . As mentioned earlier, the solution of Eq. (11.32) becomes a decaying function if the value of the square bracket is negative, that is,

$$-\gamma^2 = (n_2 k)^2 - \beta^2 \quad (11.43)$$

where

$$n = n_2 \quad (11.44)$$

The solution for F is then

$$F(r) = e I_\nu(\gamma r) + f K_\nu(\gamma r) \quad (11.45)$$

The functions $I_\nu(\gamma r)$ and $K_\nu(\gamma r)$ are, respectively, called the modified Bessel function of the first kind and the modified Bessel function of the second kind of the ν th order. The value of $I_\nu(x)$ increases with an increase in x but that of $K_\nu(x)$ decreases with an increase in x , as shown in Fig. 11.15. Since $I_\nu(x)$ becomes indefinitely large with an increase in r , it is rejected on physical grounds, and e in Eq. (11.45) should be zero.

In summary, the expressions for E_z and H_z in the cladding region, $r > a$, are

$$E_z = C K_\nu(\gamma r) e^{j\beta z + j\nu\phi} \quad (11.46)$$

$$H_z = D K_\nu(\gamma r) e^{j\beta z + j\nu\phi} \quad (11.47)$$

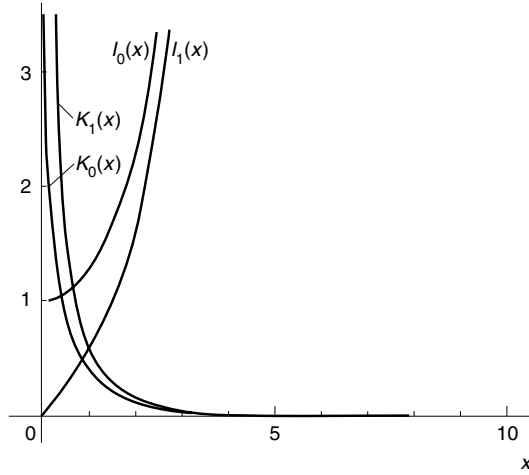


Figure 11.15 Modified Bessel functions of first $I_\nu(x)$ and the second $K_\nu(x)$ kinds.

In some literature, the Hankel function $H_\nu^{(1)}(j\gamma r)$ with a complex argument is used instead of $K_\nu(\gamma r)$. When ν is an integer, the relationship between them is

$$K_\nu(x) = \frac{\pi}{2} j^{\nu+1} H_\nu^{(1)}(jx) \quad (11.48)$$

11.2.3 Expressions for the E_r , E_ϕ , H_r , and H_ϕ Components

Having found expressions for E_z and H_z , the rest of the components are derived using Maxwell's equations. The components of

$$\nabla \times \mathbf{H} = -j\omega\epsilon\mathbf{E} \quad (11.49)$$

where

$$\nabla \times \mathbf{H} = \begin{bmatrix} \frac{\hat{\mathbf{r}}}{r} & \hat{\phi} & \frac{\hat{\mathbf{k}}}{r} \\ \frac{\partial}{\partial r} & \frac{\partial}{\partial \phi} & \frac{\partial}{\partial z} \\ H_r & rH_\phi & H_z \end{bmatrix}$$

in cylindrical coordinates are

$$\frac{1}{r} \frac{\partial H_z}{\partial \phi} - \frac{\partial H_\phi}{\partial z} = -j\omega\epsilon E_r \quad (11.50)$$

$$\frac{\partial H_r}{\partial z} - \frac{\partial H_z}{\partial r} = -j\omega\epsilon E_\phi \quad (11.51)$$

$$\frac{1}{r} \frac{\partial (rH_\phi)}{\partial r} - \frac{1}{r} \frac{\partial H_r}{\partial \phi} = -j\omega\epsilon E_z \quad (11.52)$$

and for

$$\nabla \times \mathbf{E} = j\omega\mu\mathbf{H} \quad (11.53)$$

$$\frac{1}{r} \frac{\partial E_z}{\partial \phi} - \frac{\partial E_\phi}{\partial z} = j\omega\mu H_r \quad (11.54)$$

$$\frac{\partial E_r}{\partial z} - \frac{\partial E_z}{\partial r} = j\omega\mu H_\phi \quad (11.55)$$

$$\frac{1}{r} \frac{\partial(rE_\phi)}{\partial r} - \frac{1}{r} \frac{\partial E_r}{\partial \phi} = j\omega\mu H_z \quad (11.56)$$

Equations (11.50) and (11.55) are solved for E_r and H_ϕ in terms of E_z and H_z , and Eqs. (11.51) and (11.54) are solved for E_ϕ and H_r in terms of E_z and H_z . The relationship $\partial/\partial z = j\beta$ is used.

$$E_r = \frac{j}{K^2} \left(\beta \frac{\partial E_z}{\partial r} + \omega\mu \frac{1}{r} \frac{\partial H_z}{\partial \phi} \right) \quad (11.57)$$

$$E_\phi = \frac{j}{K^2} \left(\frac{\beta}{r} \frac{\partial E_z}{\partial \phi} - \omega\mu \frac{\partial H_z}{\partial r} \right) \quad (11.58)$$

$$H_r = \frac{j}{K^2} \left(-\omega\epsilon \frac{1}{r} \frac{\partial E_z}{\partial \phi} + \beta \frac{\partial H_z}{\partial r} \right) \quad (11.59)$$

$$H_\phi = \frac{j}{K^2} \left(\omega\epsilon \frac{\partial E_z}{\partial r} + \frac{\beta}{r} \frac{\partial H_z}{\partial \phi} \right) \quad (11.60)$$

where

$$K^2 = (nk)^2 - \beta^2 \quad (11.61)$$

The fields inside the core region $r < a$ are obtained by inserting Eqs. (11.40) and (11.41) into Eq. (11.57) through (11.61) but with ϵ replaced by ϵ_1 and with K^2 replaced by $K^2 = (n_1 k)^2 - \beta^2$:

$$E_r = \frac{j}{K^2} \left(A\beta K J'_v(Kr) + B\omega\mu \frac{jv}{r} J_v(Kr) \right) \quad (11.62)$$

$$E_\phi = \frac{j}{K^2} \left(A \frac{\beta}{r} jv J_v(Kr) - B\omega\mu K J'_v(Kr) \right) \quad (11.63)$$

$$H_r = \frac{j}{K^2} \left(-A\omega\epsilon_1 \frac{jv}{r} J_v(Kr) + B\beta K J'_v(Kr) \right) \quad (11.64)$$

$$H_\phi = \frac{j}{K^2} \left(A\omega\epsilon_1 K J'_v(Kr) + B \frac{\beta}{r} jv J_v(Kr) \right) \quad (11.65)$$

where $e^{j\beta z + jv\phi}$ was suppressed.

The fields inside the cladding region $r > a$ are obtained by inserting Eqs. (11.46) and (11.47) into Eqs. (11.57) through (11.61), but with ϵ replaced by ϵ_2 and with K^2

replaced by $-\gamma^2 = (n_2k)^2 - \beta^2$:

$$E_r = \frac{-j}{\gamma^2} \left(C\beta\gamma K'_v(\gamma r) + D\omega\mu \frac{jv}{r} K_v(\gamma r) \right) \quad (11.66)$$

$$E_\phi = \frac{-j}{\gamma^2} \left(C\frac{\beta}{r} jv K_v(\gamma r) - D\omega\mu\gamma K'_v(\gamma r) \right) \quad (11.67)$$

$$H_r = \frac{-j}{\gamma^2} \left(-C\omega\epsilon_2 \frac{jv}{r} K_v(\gamma r) + D\beta\gamma K'_v(\gamma r) \right) \quad (11.68)$$

$$H_\phi = \frac{-j}{\gamma^2} \left(C\omega\epsilon_2\gamma K'_v(\gamma r) + D\frac{\beta}{r} jv K_v(\gamma r) \right) \quad (11.69)$$

where $e^{j\beta z + jv\phi}$ was suppressed. Note that if A , B , ϵ_1 , K , and $J_v(Kr)$ in Eqs. (11.62) to (11.65) are replaced by C , D , ϵ_2 , $j\gamma$, and $K_v(\gamma r)$, respectively, the results are Eqs. (11.66) to (11.69).

11.2.4 Characteristic Equation of an Optical Fiber

Boundary conditions are applied on the boundary between the core and cladding regions. The tangential components of \mathbf{E} and \mathbf{H} have to be continuous at $r = a$. The tangential components of \mathbf{E} are E_z and E_ϕ and those of \mathbf{H} are H_z and H_ϕ .

There are two ways to find the coefficients A , B , C , and D that satisfy these conditions. One way is by a matrix method, whereby the conditions for E_z , E_ϕ , H_z , and H_ϕ at $r = a$ are arranged in a matrix form with A , B , C , and D in Eqs. (11.62) through (11.69) as unknowns. Then the 4×4 determinant is calculated to find the condition for the nontrivial solutions of A , B , C and D [19]. The other way is to find the value of C in terms of A using the continuity condition for E_z , and to find the value of D in terms of B using the continuity condition for H_z . Then, only the 2×2 matrix of A and B has to be calculated. This method involves less manipulation and will be used here.

First, C will be found in terms of A . Continuity of E_z gives

$$AJ_v(Ka) = CK_v(\gamma a) \quad (11.70)$$

hence,

$$C = \frac{J_v(Ka)}{K_v(\gamma a)} A \quad (11.71)$$

In a similar manner, continuity of H_z is used to find D in terms of B .

$$D = \frac{J_v(Ka)}{K_v(\gamma a)} B \quad (11.72)$$

Both Eqs. (11.71) and (11.72) have the same factor.

Next, C and D in the expressions for E_ϕ and H_ϕ , Eqs. (11.67) and (11.69), are to be replaced by A and B using Eqs. (11.71) and (11.72), and then the equations necessary

for the continuity of E_ϕ and H_ϕ are reduced to

$$A\beta v \left(\frac{1}{(Ka)^2} + \frac{1}{(\gamma a)^2} \right) + jB\omega\mu \left(\frac{J'_v(Ka)}{KaJ_v(Ka)} + \frac{K'_v(\gamma a)}{\gamma aK_v(\gamma a)} \right) = 0 \quad (11.73)$$

$$A\omega \left(\frac{\epsilon_1 J'_v(Ka)}{KaJ_v(Ka)} + \frac{\epsilon_2 K'_v(\gamma a)}{\gamma aK_v(\gamma a)} \right) + jB\beta v \left(\frac{1}{(Ka)^2} + \frac{1}{(\gamma a)^2} \right) = 0 \quad (11.74)$$

For nontrivial solutions for A and B to exist, the determinant of the coefficients has to vanish. The result is

$$\begin{aligned} & \left(\frac{1}{Ka} \frac{J'_v(Ka)}{J_v(Ka)} + \frac{1}{\gamma a} \frac{K'_v(\gamma a)}{K_v(\gamma a)} \right) \left(\frac{J'_v(Ka)}{KaJ_v(Ka)} + \left(\frac{n_2}{n_1} \right)^2 \frac{K'_v(\gamma a)}{\gamma aK_v(\gamma a)} \right) \\ &= \left[\frac{\beta v}{n_1 k} \left(\frac{1}{(Ka)^2} + \frac{1}{(\gamma a)^2} \right) \right]^2 \end{aligned} \quad (11.75)$$

This is the characteristic equation for a step-index fiber.

Only values of Ka and γa that satisfy Eq. (11.75) will satisfy the boundary condition at the core-cladding boundary. There are two unknowns, Ka and γa , in Eq. (11.75). One more equation is needed to determine the unknowns. That is obtained by combining Eqs. (11.37) and (11.43):

$$V^2 = (Ka)^2 + (\gamma a)^2 \quad (11.76)$$

where

$$V = ka\sqrt{n_1^2 - n_2^2} \quad (11.77)$$

In short, one has to solve for the γa and Ka that satisfy Eqs. (11.75) and (11.76) for given physical parameters of the normalized radius V and the value of n_2/n_1 . The procedures for obtaining the solutions are exactly the same as those of the slab optical guides described in Chapter 9.

11.2.5 Modes in Optical Fibers

A graph of Eq. (11.75) in $(\gamma a, Ka)$ coordinates is a combination of Bessel function curves. The graph of Eq. (11.76) is a circle with radius V . The intersects between the two curves are solutions. Each intersect is designated as a mode that can be excited and gives such information as the cutoff conditions and the cross-sectional distribution of light in the fiber.

The solutions of the characteristic equation vary a great deal depending on whether $v = 0$ or $v \neq 0$. Hence, they will be treated in two separate sections.

11.2.5.1 Meridional Modes: $v = 0$

As seen from Eq. (11.34) or (11.35), as soon as $v = 0$, the ϕ -dependent factor becomes a constant and a meridional ray is excited. The characteristic equation is significantly

simplified. With $\nu = 0$ the order of the Bessel function reduces, and the right-hand side of Eq. (11.75) becomes zero so that Eq. (11.75) reduces to

$$\frac{J_1(Ka)}{KaJ_0(Ka)} + \frac{K_1(\gamma a)}{\gamma a K_0(\gamma a)} = 0, \quad \text{TE mode} \quad (11.78)$$

and

$$\frac{J_1(Ka)}{KaJ_0(Ka)} + \left(\frac{n_2}{n_1}\right)^2 \frac{K_1(\gamma a)}{\gamma a K_0(\gamma a)} = 0, \quad \text{TM mode} \quad (11.79)$$

where the Bessel function relationships $J'_0(x) = -J_1(x)$ and $K'_0(x) = -K_1(x)$ were used. Equation (11.78) is the characteristic equation for the TE mode and Eq. (11.79) is for the TM mode.

There is a reason for naming these characteristic equations the TE mode or the TM mode, as will be explained before proceeding. From Eqs. (11.40) and (11.41), the ratio of the intensities of H_z to E_z is $(B/A)^2$. Using Eq. (11.73), the ratio $(B/A)^2$ is calculated, and then the term $\beta v(1/(Ka)^2 + 1/(\gamma a)^2)$ is rewritten using Eq. (11.74) to obtain

$$\left(\frac{B}{A}\right)^2 = \frac{1}{\eta_1^2} \frac{\frac{J'_v(Ka)}{KaJ_v(Ka)} + \left(\frac{n_2}{n_1}\right)^2 \frac{1}{\gamma a} \frac{K'_v(Ka)}{K_v(Ka)}}{\frac{J'_v(Ka)}{KaJ_v(Ka)} + \frac{K'_v(\gamma a)}{\gamma a K_v(\gamma a)}} \quad (11.80)$$

where $\eta_1 = \sqrt{\mu/\epsilon_1}$.

If Eq. (11.78) is satisfied, the denominator of the right-hand side of Eq. (11.80) becomes zero for the meridional mode; hence, $A = 0$. This means $E_z = 0$ and there is no longitudinal component of \mathbf{E} and its mode is called a TE (transverse electric) mode. On the other hand, when Eq. (11.79) is satisfied, $B = 0$ and hence $H_z = 0$ and its mode is a TM (transverse magnetic) mode.

Let us leave the exact shape of the Ka versus γa curves of Eqs. (11.78) and (11.79) to the magic power of an electronic computer, and concentrate our attention on making some sense out of the curves. Let us start by examining the curve near the zero and infinity of γ .

The mode is cut off at $\gamma a = 0$ because the decay of the field with respect to r in the cladding is absent and the field is not confined inside the core. The operating point of a single-mode fiber is normally placed at as large a value of γa as possible, within the limit that the next higher mode is not excited.

First, the cutoff conditions of the TE modes will be examined by setting

$$\gamma a = 0 \quad (11.81)$$

Judging from the curves of $K_0(x)$ and $K_1(x)$ in Fig. 11.15 (or more exactly by Eq. (11.98), which will appear later), the limit as γa approaches zero gives

$$\lim_{\gamma a \rightarrow 0} \frac{K_1(\gamma a)}{K_0(\gamma a)} \gg 1 \quad (11.82)$$

Hence, the condition for Eq. (11.78) to be valid at $\gamma a = 0$ is

$$J_0(Ka) = 0_- \quad (11.83)$$

where 0_- means extremely close to zero but a negative number. The roots $\omega_{0\mu}$ of $J_0(\omega) = 0$ are

$$\begin{aligned} \omega_{01} &= 2.4 & \omega_{02} &= 5.5 \\ \omega_{03} &= 8.7 & \omega_{04} &= 11.8 \end{aligned}$$

In conclusion, the values of Ka at the $\gamma a = 0$ cutoff are $\omega_{0\mu}$.^{*} The characteristic curves are numbered starting with the smallest Ka cutoff values to the larger values.

The TE modes are designated by $TE_{0\mu}$, where 0 means $\nu = 0$, and μ indicates the μ th root of the $\nu = 0$ modes. Thus, the cutoffs of the TE_{01} , TE_{02} , and TE_{03} modes are at $Ka = 2.4$, 5.5 , and 8.7 , respectively.

From Eq. (11.79), applying the limit as γa approaches zero gives the same result as for Eq. (11.78). Thus, at the cutoff $\gamma a = 0$, the TM modes become identical to the TE modes and have the same cutoff values as above. It is said that the TE and TM modes are degenerate at $\gamma a = 0$. At all other points, however, they are different and the degeneracy is removed.

Next, the behavior of the TE mode in the region far from cutoff, $\gamma a \rightarrow \infty$, is examined. As seen either from Fig. 11.15 (or more exactly by Eq. (11.101), which will appear later), $\lim_{\gamma a \rightarrow \infty} [K_1(\gamma a)/K_0(\gamma a)]$ is finite and in this region, the first term in Eq. (11.78) has to be zero:

$$J_1(Ka) = 0 \quad (11.84)$$

The roots for $J_1(P) = 0$ are

$$\begin{aligned} P_{10} &= 0.0 & P_{11} &= 3.8 \\ P_{12} &= 7.0 & P_{13} &= 10 \end{aligned}$$

The first term of Eq. (11.78) does not become zero at $Ka = P_{10}$ because Ka is also zero and the value of the limit of the first term becomes

$$\lim_{Ka \rightarrow 0} \frac{J_1(Ka)}{Ka} = \frac{1}{2} \quad (11.85)$$

and P_{10} has to be excluded as an asymptote for $\gamma a = \infty$. Equation (11.79) will give the same result as Eq. (11.78) and the TM modes have the same asymptote for $\gamma a = \infty$ as the TE modes.

From the behavior near $\gamma a = 0$ and $\gamma a = \infty$, the general curve shape of the characteristic equation is drawn, as shown in Fig. 11.16. The upper and lower graphs are $J_1(Ka)$ and $J_0(Ka)$, respectively. From the roots of these functions, dotted lines are extended to the middle graph to indicate the locations of the cutoff and the asymptotes of the characteristic curve.

The values of Ka and γa for a given value of V are found from the intercepts between the characteristic curve and the circle with radius V . The propagation constant β for a particular mode is found by using Eq. (11.37) or (11.43). This procedure is the same as that of the slab optical guide treated in Section 9.3.1.

^{*} $Ka = 0$ is excluded because of Eq. (11.85).

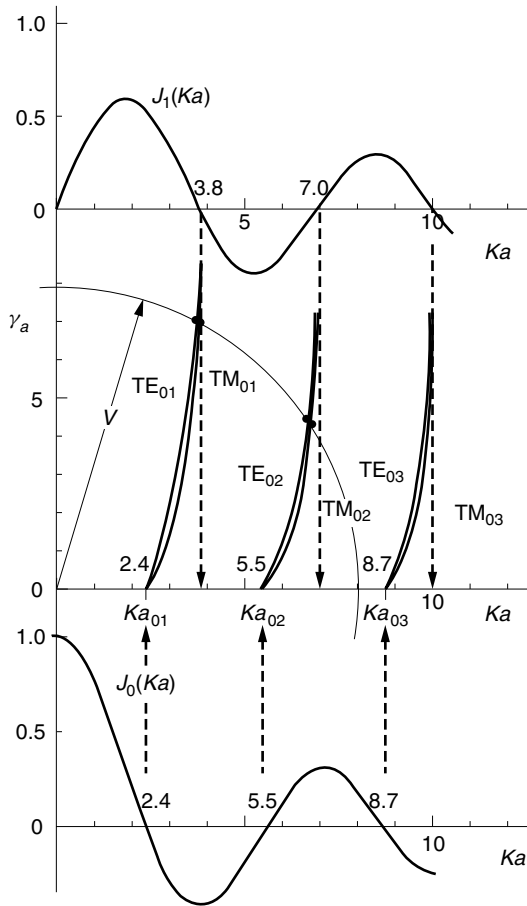


Figure 11.16 Curves of the characteristic equation of the $TE_{0\mu}$ and $TM_{0\mu}$ modes.

When Eq. (11.78) for the $TE_{0\mu}$ modes is compared with Eq. (11.79) for $TM_{0\mu}$, the only difference is that Eq. (11.79) has an extra factor $(n_2/n_1)^2$, which in most cases is $(1.005)^2$ and is close to unity. Both characteristic curves are of similar shape except that the curve for $TM_{0\mu}$ is slightly lower than that of the $TE_{0\mu}$ mode.

11.2.5.2 Skew Modes: $\nu \neq 0$

When $\nu \neq 0$, the right-hand side of Eq. (11.75) is not zero and the procedure for obtaining the solution of the characteristic equation is much more complicated. In practice, the difference in the index of refraction of the core and cladding regions is 0.3–0.5% for most optical fibers, and the approximation

$$\left(\frac{n_2}{n_1}\right)^2 \doteq 1 \quad (11.86)$$

is a very good one.

This approximation significantly reduces the complexity of solving Eq. (11.75), for both the $\nu = 0$ and $\nu \neq 0$ cases. The theory based on this approximation is known as the *theory with the weakly guiding approximation* [20]. This name is from a sense that the guiding capability of a fiber comes from the difference in the indices of refraction of the core and cladding, and when the difference is small, the light is weakly guided. With the weakly guiding approximation, Eq. (11.75) becomes

$$\frac{J'_\nu(Ka)}{KaJ_\nu(Ka)} + \frac{K'_\nu(\gamma a)}{\gamma aK_\nu(\gamma a)} = \pm \nu \left(\frac{1}{(Ka)^2} + \frac{1}{(\gamma a)^2} \right) \quad (11.87)$$

where the assumption

$$\beta \doteq n_1 k \quad (11.88)$$

was made, because in a weakly guided fiber, only the component waves with a very shallow zigzag angle can propagate.

As mentioned earlier, the case of $\nu = 0$ was rather straightforward. One of the roots was $A = 0$; hence, $E_z = 0$ and this mode was called the TE mode or sometimes the H mode. The other root was $B = 0$; hence, $H_z = 0$ and this was called the TM mode or E mode.

In the case of $\nu \neq 0$, the situation is different. With the weakly guiding approximation, Eq. (11.75) is split into two equations, as indicated in Eq. (11.87), because of the positive and negative signs. Referring to the right-hand side of Eq. (11.87), one has to realize that the Ka versus γa curve with the $+$ sign is certainly different from that with the $-$ sign, for the same value of ν . It is necessary to establish two names to distinguish the two different solutions. There are three ways of distinguishing the two solutions. One is by the sign in front of ν . The characteristic equation with the negative sign is named the characteristic equation of the HE modes while that with the positive sign is named the characteristic equation of the EH modes. The second is by the sign of $j(B/A)\eta_1$, which is more popular.

Let us derive the value of $j(B/A)\eta_1$. From Eq. (11.73) and (11.87), the ratio B/A is

$$\frac{B}{A} = -\frac{\beta}{j\omega\mu} \frac{\nu \left(\frac{1}{(Ka)^2} + \frac{1}{(\gamma a)^2} \right)}{\pm \nu \left(\frac{1}{(Ka)^2} + \frac{1}{(\gamma a)^2} \right)} \quad (11.89)$$

With Eq. (11.88), Eq. (11.89) becomes

$$j\frac{B}{A} = \mp \frac{1}{\eta_1} \quad (11.90)$$

The values of $j(B/A)\eta_1$ depend on the sign in front of ν . Snitzer [21] proposed to call a mode HE if the value $j(B/A)\eta_1$ is $+1$ at the cutoff, and EH if it is -1 at the cutoff.

Here we will accept Snitzer's proposal.

$$\text{With negative sign in front of } \nu, \quad j \frac{B}{A} \eta_1 = +1 \quad HE \text{ mode} \quad (11.91)$$

$$\text{With positive sign in front of } \nu, \quad j \frac{B}{A} \eta_1 = -1 \quad EH \text{ mode}$$

Thus, it has been shown that the sign in front of ν is related to that of $j(B/A)\eta_1$.

The fact that $j(B/A)\eta_1 = \pm 1$ means that A or B alone cannot be zero, and there is no pure TE or TM mode because TE, for instance, requires $A = 0$ and $B \neq 0$. Both E_z and H_z are present when $\nu \neq 0$. Modes that contain both E_z and H_z components are called *hybrid modes*. This is the reason why the notation for hybrid modes uses both letters, E and H .

The third way of deciding which solution is to be called the HE mode and which is to be called the EH mode will be mentioned. This method dictates that, when the E_z component found by using the rigorous equations is larger than the H_z component, the mode is called an EH mode, and when it is the other way around, the mode is called an HE mode. This method, however, requires detailed information about the location, how far from the cutoff, and so forth.

Now, Eq. (11.87) will be rewritten using the following Bessel function recurrence formulas

$$J'_\nu(x) = J_{\nu-1}(x) - \frac{\nu}{x} J_\nu(x) \quad (11.92)$$

$$K'_\nu(x) = -K_{\nu-1}(x) - \frac{\nu}{x} K_\nu(x) \quad (11.93)$$

$$J'_\nu(x) = -J_{\nu+1}(x) + \frac{\nu}{x} J_\nu(x) \quad (11.94)$$

$$K'_\nu(x) = -K_{\nu+1}(x) + \frac{\nu}{x} K_\nu(x) \quad (11.95)$$

Equation (11.87) with the negative sign and Eqs. (11.92) and (11.93) lead to the characteristic equation of the HE modes, while Eq. (11.87) with the positive sign and Eqs. (11.94) and (11.95) lead to the characteristic equation of the EH modes.

$$\frac{J_{\nu-1}(Ka)}{KaJ_\nu(Ka)} - \frac{K_{\nu-1}(\gamma a)}{\gamma a K_\nu(\gamma a)} = 0, \quad HE \text{ modes} \quad (11.96)$$

$$\frac{J_{\nu+1}(Ka)}{KaJ_\nu(Ka)} + \frac{K_{\nu+1}(\gamma a)}{\gamma a K_\nu(\gamma a)} = 0, \quad EH \text{ modes} \quad (11.97)$$

First, the HE cutoffs will be found. Useful Bessel function approximations are, for $x \ll 1$,

$$\frac{K_0(x)}{K_1(x)} = x \ln \left(\frac{2}{1.782x} \right) \quad (11.98)$$

$$\frac{K_{\nu-1}(x)}{K_\nu(x)} = \frac{x}{2(\nu-1)}, \quad \nu \geq 2 \quad (11.99)$$

$$\frac{J_{\nu-1}(x)}{J_{\nu}(x)} = \frac{2}{x}\nu \quad (11.100)$$

and for $x \gg 1$,

$$\frac{K_{\nu \mp 1}(x)}{K_{\nu}(x)} = 1 + \frac{1 \mp 2\nu}{2x} \quad (11.101)$$

The behavior of Eq. (11.96) near cutoff, $\gamma a \rightarrow 0$, will be investigated for $\nu \geq 2$. With Eq. (11.99), near $\gamma a \rightarrow 0$, Eq. (11.96) becomes

$$\frac{J_{\nu-1}(Ka)}{KaJ_{\nu}(Ka)} = \frac{1}{2(\nu-1)} \quad (11.102)$$

The recurrence formulas are from Eqs. (11.92) to (11.95),

$$J_{n+1}(x) + J_{n-1}(x) = \frac{2n}{x}J_n(x) \quad (11.103)$$

$$K_{n+1}(x) - K_{n-1}(x) = \frac{2n}{x}K_n(x) \quad (11.104)$$

Equation (11.103) is used with $n = \nu - 1$ to reduce Eq. (11.102) to

$$KaJ_{\nu-2}(Ka) = 0 \quad (11.105)$$

For $\nu \geq 2$, $Ka = 0$ has to be excluded from the solutions. This is because for $\nu \geq 2$ the right-hand side of Eq. (11.102) is finite, and the left-hand side becomes infinite from Eq. (11.100). The roots of Eq. (11.105) are the cutoffs of the *HE* modes. The roots are numbered by μ , and the *HE* mode with the μ th root is designated by *HE* _{$\nu\mu$} . The roots of the *HE* _{2μ} modes are $Ka = 2.40, 5.52, 8.65, \dots$

In the above, the case of $\nu = 1$ was avoided because a different approximate expression applies, namely Eq. (11.98) rather than Eq. (11.99). With Eq. (11.98), the second term of Eq. (11.96) approaches infinity as $\gamma a \rightarrow 0$, and the solution becomes

$$KaJ_1(Ka) = 0 \quad (11.106)$$

On the other hand, from Eq. (11.96), when $\gamma a \rightarrow \infty$, $J_0(Ka) = 0$.

The general curve shape of the characteristic equation is drawn as shown in Fig. 11.17. The upper and lower graphs are $J_0(Ka)$ and $J_1(Ka)$, respectively,* to indicate the locations of the asymptotes and the cutoff of the characteristic curve.

The roots of Eq. (11.106) are $Ka = 0, 3.83, 7.02, 10.2$. The first root is $Ka = 0$, and the cutoff of the *HE*₁₁ mode is zero. For this reason the *HE*₁₁ mode is the dominant mode of the optical fiber. The cutoff condition of the next higher order mode is Eq. (11.83) for *TE*₀₁ and *TM*₀₁, and Eq. (11.105) for the *HE*₂₁ mode as shown in Fig. 11.18. Both of these cutoff conditions are the same, $J_0(Ka) = 0$. Thus, the condition to be a single-mode fiber is

$$V < 2.40 \quad (11.107)$$

Next, the cutoffs of the *EH* modes will be obtained. First, the cases with $\nu \geq 2$ are considered. Using the relationship of Eq. (11.99) with $\nu = \nu' + 1$, we see that

* $KaJ_1(Ka)$ and $J_1(Ka)$ have their zeros at the same locations.

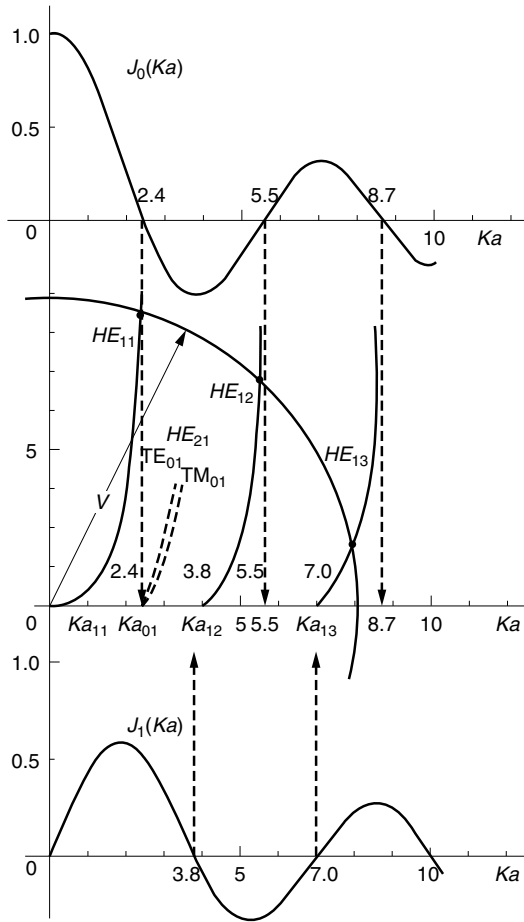


Figure 11.17 Curves of the characteristic equation of the $HE_{1\mu}$ modes.

the second term of Eq. (11.97) becomes infinite as $\gamma a \rightarrow 0$, and at first glance the solution is

$$KaJ_\nu(Ka) = 0 \quad (11.108)$$

The first root of Eq. (11.108) is $Ka = 0$. However, we have to consider this first root more carefully. An approximate expression for $J_\nu(Ka)$ for small Ka and integer ν is

$$J_\nu(Ka) = \frac{1}{\nu!} \left(\frac{Ka}{2} \right)^\nu \quad (11.109)$$

With Eq. (11.109), the first term of Eq. (11.97) becomes

$$\frac{J_{\nu+1}(Ka)}{KaJ_\nu(Ka)} = \frac{1}{2(\nu+1)} \quad (11.110)$$

which is not infinity at $Ka = 0$, and the first root has to be excluded. Next, a similar treatment with $\nu = 1$ leads to the same condition as Eq. (11.108) and the same exclusion of $Ka = 0$. The lowest cutoff of the EH modes is at $Ka = 3.83$ of the EH_{11} mode, and the cutoff of the next higher EH mode is at $Ka = 5.13$ of EH_{21} as summarized in Fig. 11.18.

From Eqs. (11.105) and (11.108), note that the cutoff conditions of $HE_{\nu+1,\mu}$ are identical to that of $EH_{\nu-1,\mu}$.

Next, it will be shown that it is not just the cutoff values of the $HE_{\nu+1,\mu}$ and $EH_{\nu-1,\mu}$ modes that are identical, but the characteristic equations themselves are identical. After inserting $\nu = m + 1$ into Eq. (11.96) and $\nu = m - 1$ into Eq. (11.97), the second terms are moved to the right-hand side. Then, both sides are inverted. The results are

$$\frac{KaJ_{m+1}(Ka)}{J_m(Ka)} = \frac{\gamma a K_{m+1}(\gamma a)}{K_m(\gamma a)} \quad (11.111)$$

$$\frac{KaJ_{m-1}(Ka)}{J_m(Ka)} = -\frac{\gamma a K_{m-1}(\gamma a)}{K_m(\gamma a)} \quad (11.112)$$

and use of the recurrence formulas, Eqs. (11.103) and (11.104), for rewriting $J_{m+1}(Ka)$ and $K_{m+1}(\gamma a)$ convert Eq. (11.111) into (11.112), thus proving that the characteristic equation of $HE_{m+1,\mu}$ is identical with that of $EH_{m-1,\mu}$ in the case of the weakly guiding approximation. Because of the identical nature of the characteristic equations, the two modes are given the same mode name, $LP_{m\mu}$, which stands for linearly polarized mode [20]. For instance, the characteristic equations of the $HE_{3\mu}$, $EH_{1\mu}$ and $LP_{2\mu}$ modes are all identical as far as the characteristic equations are concerned. However, the field patterns of these three modes are all different, as will be explained in detail in the next section.

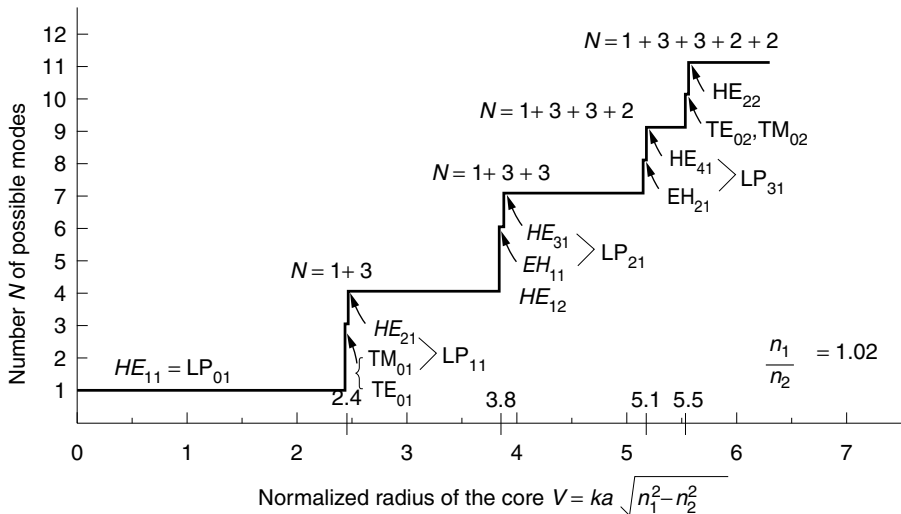


Figure 11.18 Number of possible modes in the step-index fiber as a function of the normalized radius of the core.

Example 11.1 What is the HE mode that pairs with $EH_{5\mu}$ to form a linear polarization (LP) mode? What is the corresponding $LP_{m\mu}$ mode?

Solution They are $HE_{7\mu}$ and $LP_{6\mu}$. □

As was done for the $\nu = 0$ case, a rough sketch of the characteristic curves for the $\nu \neq 0$ case will be made. These curves are used to find the values of Ka and γa from the intersect with a circle of constant V . The behavior of the characteristic curves has been derived near cutoff, $\gamma a = 0$. Before we can sketch the curves, the behavior of the characteristic curve near $\gamma a = \infty$ has to be investigated.

The Ka asymptote of the $HE_{\nu\mu}$ modes for $\gamma a \rightarrow \infty$ are found from Eqs. (11.96) and (11.101) as

$$\frac{J_{\nu-1}(Ka)}{KaJ_{\nu}(Ka)} = 0 \quad (11.113)$$

Thus,

$$J_{\nu-1}(Ka) = 0 \quad (11.114)$$

Finally, the Ka asymptote for the $EH_{\nu\mu}$ modes for $\gamma a \rightarrow \infty$ are found from Eqs. (11.97) and (11.101) as

$$J_{\nu+1}(Ka) = 0 \quad (11.115)$$

A summary of the various Bessel function conditions obtained in Section 11.2.5 for the limits $\gamma a \rightarrow 0$ and $\gamma a \rightarrow \infty$ are tabulated in Table 11.1.

In summary, graphs of the characteristic equation with $\nu = 0$ are drawn in Fig. 11.16. Figure 11.17 is an example of a graph with $\nu = 1$ for the $HE_{1\mu}$ modes. Another example, for the $HE_{3\mu}$ and $EH_{1\mu}$ modes, is sought in Problem 11.3. Intersections of the characteristic curves in Ka - γa coordinates with a circle of radius V , where $V^2 = (Ka)^2 + (\gamma a)^2$, are solutions of Ka and γa for the wavelength of operation in a given fiber.

As shown in Fig. 11.17, the intersection of V with the HE_{11} curve can exist from $V = 0$ to infinity. At $V = 2.4$, the intersections with the TE_{01} , TM_{01} , and HE_{21} curves start to exist. Only the HE_{11} mode is excited in the region $0 < V < 2.4$, so that for

Table 11.1 Bessel functions whose roots give Ka values at either $\gamma a \rightarrow 0$ or $\gamma a \rightarrow \infty$, for modes in a step-index fiber

Limits	Types of Modes		
	$TE_{0\mu}, TM_{0\mu}$	$HE_{\nu\mu}$	$EH_{\nu\mu}$
Near cutoff, $\gamma a \rightarrow 0$	$J_0(Ka) = 0$	$\nu = 1, J_1(Ka) = 0$ including $Ka = 0$ $\nu \geq 2, J_{\nu-2}(Ka) = 0$ except $Ka = 0$	$J_{\nu}(Ka) = 0$ except $Ka = 0$
Far from cutoff, $\gamma a \rightarrow \infty$	$J_1(Ka) = 0$	$J_{\nu-1}(Ka) = 0$	$J_{\nu+1}(Ka) = 0$

$V < 2.4$, the fiber is a single-mode fiber. Each mode can be excited over a region starting from its cutoff value V_c and extending to infinite V . Inside the range of a given mode, the larger V is, the larger γa is. A large value of γ means the field is better confined in the core and the radiation loss of the fiber due to bending decreases.

As the radius V is increased, the number N of intersections with the characteristic curves is increased. N is plotted as a function of V in Fig. 11.18.

Numerical solutions of the transcendental equations of the characteristic curves based on the weakly guiding approximation and the V circle are shown in Fig. 11.19 [19]. The solutions are shown in universal coordinates in Fig. 11.19. The vertical axis is the normalized propagation parameter given by

$$b = (\gamma a / V)^2 \quad (11.116)$$

and the horizontal axis is V . It should be noted that the (m, μ) values are for the $LP_{m\mu}$ modes, but they can be converted into hybrid modes as explained in Example 11.1. An advantage of taking b as a variable is that b has a finite range from 0 to 1. This can be seen by referring to the triangle in Fig. 11.20, which is drawn from Eq. (11.76). The quantity b is expressed as $b = \sin^2 \theta$. Using Eq. (11.76), the value of Ka is calculated from b as

$$Ka = \sqrt{1 - b}V \quad (11.117)$$

Using Eq. (11.37), the propagation constant can also be calculated from b as

$$\beta^2 = (n_1 k)^2 [1 - 2\Delta(1 - b)] \quad (11.118)$$

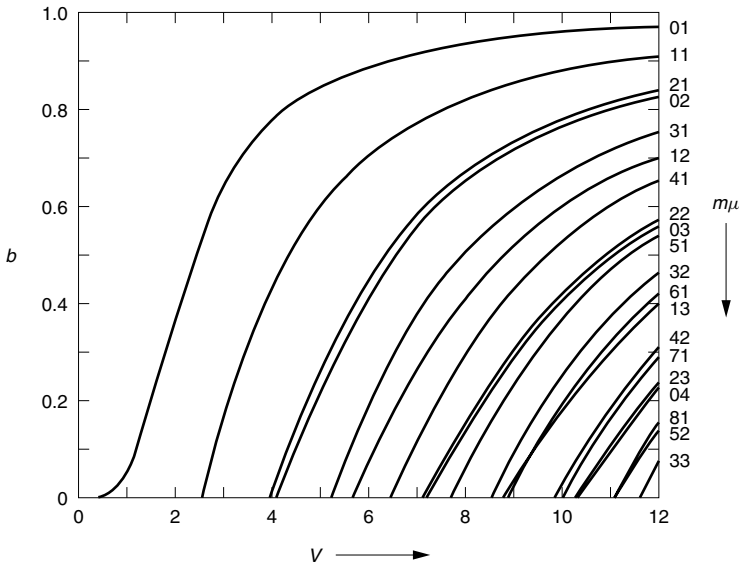


Figure 11.19 Normalized propagation parameter b as a function of the normalized frequency V for $LP_{m\mu}$ modes, which consists of $HE_{m+1\mu}$ and $EH_{m-1\mu}$ for $m > 1$; and $HE_{2\mu}$, $TM_{0\mu}$, $TE_{0\mu}$ for $m = 1$; and $HE_{1\mu}$ for $m = 0$. (After D. Gloge [20].)

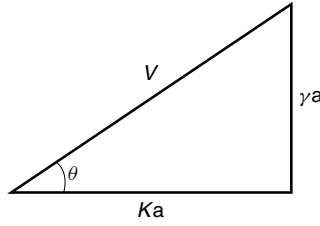


Figure 11.20 Relationship between γa , Ka , and V .

where

$$\Delta = \frac{n_1 - n_2}{n_1} \quad (11.119)$$

and

$$2n_1 \doteq n_1 + n_2$$

Applying the binomial expansion to Eq. (11.118) gives the approximation

$$\beta = n_1 k [1 - \Delta(1 - b)] \quad (11.120)$$

Example 11.2

- If a laser light with wavelength $\lambda = 0.63 \mu\text{m}$ is incident into an optical fiber that was originally designed to be a single-mode fiber ($V = 2.0$, $a = 1.5 \mu\text{m}$, $n_1 = 1.458$) at wavelength $\lambda = 1.55 \mu\text{m}$, how many modes will the fiber support?
- List the mode(s) in hybrid mode designation. (The parameters ($m\mu$) in the figure are linear polarization designations).
- Conversely, if a laser light with wavelength $\lambda = 1.55 \mu\text{m}$ is incident into an optical fiber that was originally designed to be a single-mode fiber ($V = 2.0$, $a = 1.5 \mu\text{m}$, $n_1 = 1.458$) at wavelength $\lambda = 0.63 \mu\text{m}$, how many modes will the fiber support? What is (are) the value(s) of the propagation constant(s)?
- What is the value of γ , which represents the evanescent field in the cladding?

Solution

(a)

$$2.0 = \frac{2\pi}{1.55} a \sqrt{n_1^2 - n_2^2}$$

$$V = \frac{2\pi}{0.63} a \sqrt{n_1^2 - n_2^2}$$

From the ratio of the two equations, the value of V is

$$V = 4.92$$

From Fig. 11.19, four LP modes are supported.

(b) The intercepts between the mode lines and $V = 4.92$ in Fig. 11.19 give the modes. The parameters $(m\mu)$ of Fig. 11.19 are for the $LP_{m\mu}$ modes and their corresponding expressions in hybrid modes for $m = 0$, and $m = 1$ are explained in the labeling of the graph. The results are tabulated as follows:

$(m\mu)$	(01)	(11)	(21)	(02)
$LP_{m\mu}$ designation	LP_{01}	LP_{11}	LP_{21}	LP_{02}
Hybrid mode designation	HE_{11}	HE_{21} TE_{01} TM_{01}	HE_{31} EH_{11}	HE_{12}

(c)

$$V = 0.81$$

From the graph, only one mode HE_{11} is supported with $b = 0.04$. Next, the propagation constant is

$$\beta = n_1 k [1 - \Delta(1 - b)]$$

The value of Δ has to be found to calculate β :

$$\begin{aligned} 2.0 &= \frac{2\pi}{0.63} (1.5)(1.458)\sqrt{2\Delta} \\ \Delta &= 0.0042 \\ \beta &= (1.458) \frac{2\pi}{1.55} [1 - 0.0042(1 - 0.04)] \\ &= 5.9 \text{ rad}/\mu\text{m} \end{aligned}$$

(d) Since $b = (\gamma a/V)^2$ is reduced to 0.04, the decay of the field in the cladding is small and is therefore subject to leakage. More specifically,

$$\gamma = \sqrt{b} \frac{V}{a} = (0.2) \frac{0.81}{1.5} = 0.108 \text{ rad}/\mu\text{m} \quad \square$$

11.3 FIELD DISTRIBUTIONS INSIDE OPTICAL FIBERS

Field expressions have already been given by Eqs. (11.62) through (11.69). These expressions, however, are too cumbersome from which to draw field patterns. Attempts will be made to simplify these expressions by some legitimate approximations [17]. With the approximations of Eq. (11.88), Eq. (11.62) at $z = 0$ can be rewritten as

$$E_r = E \left[J'_v(Kr) + j \frac{B}{A} \frac{\omega\mu}{n_1 k} \cdot \frac{v}{Kr} J_v(Kr) \right] e^{jv\phi} \quad (11.121)$$

where

$$E = \frac{jAn_1k}{K} = |E|e^{j(\pi/2)}$$

The factor involving the ratio B/A in the square brackets in Eq. (11.121) is simplified as

$$j\frac{B}{A}\frac{\omega\mu}{\omega\sqrt{\epsilon_1\mu}} = j\frac{B}{A}\eta_1 \quad (11.122)$$

From Eq. (11.91), the value of Eq. (11.122) is either $+1$ or -1 depending on whether the mode is a HE or EH mode. Thus, with Eq. (11.92), the real part of E_r for the HE modes becomes

$$E_r = |E|J_{\nu-1}(Kr) \cos\left(\nu\phi + \frac{\pi}{2}\right) \quad HE \text{ modes} \quad (11.123)$$

In the following, the absolute sign on $|E|$ and $\pi/2$ will be suppressed. And with Eq. (11.94), E_r for the EH modes becomes

$$E_r = -EJ_{\nu+1}(Kr) \cos \nu\phi \quad EH \text{ modes} \quad (11.124)$$

Next, simplified expressions for the magnetic fields will be obtained. Equation (11.64), with the approximation of Eq. (11.88), is written as

$$H_r = \frac{jn_1k}{K} \left[-\frac{\omega\epsilon_1}{n_1k}A\frac{j\nu}{Kr}J_\nu(Kr) + BJ'_\nu(Kr) \right] e^{j\nu\phi} \quad (11.125)$$

The factor in the first term in the square brackets can be rewritten with the help of Eq. (11.122) and H_r becomes

$$H_r = -jH \left[\frac{\nu}{Kr}J_\nu(Kr) + \left(j\frac{B}{A}\eta_1 \right) J'_\nu(Kr) \right] e^{j\nu\phi} \quad (11.126)$$

where

$$H = \frac{E}{\eta_1}$$

With Eq. (11.91) for the HE modes and Eq. (11.92), the expression for the real part of H_r becomes

$$H_r = HJ_{\nu-1}(Kr) \sin \nu\phi \quad HE \text{ modes} \quad (11.127)$$

With Eq. (11.91) for the EH modes and Eq. (11.94), the expression for H_r is

$$H_r = HJ_{\nu+1}(Kr) \sin \nu\phi \quad EH \text{ modes} \quad (11.128)$$

The rest of the field components can be found in a similar manner. They are summarized as follows. From Eqs. (11.40), (11.41), and (11.91), E_z and H_z for both $HE_{\nu\mu}$

and $EH_{v\mu}$ modes are

$$\begin{aligned} E_z &= AJ_v(K_{v\mu}r) \cos v\phi \\ H_z &= \pm \frac{A}{\eta_1} J_v(K_{v\mu}r) \sin v\phi \end{aligned} \quad (11.129)$$

For $HE_{v\mu}$ modes only,

$$\begin{aligned} E_r &= EJ_{v-1}(K_{v\mu}r) \cos v\phi \\ E_\phi &= -EJ_{v-1}(K_{v\mu}r) \sin v\phi \end{aligned} \quad (11.130)$$

and from Eqs. (11.62) to (11.65),

$$\begin{aligned} H_r &= -\frac{1}{\eta_1} E_\phi \\ H_\phi &= \frac{1}{\eta_1} E_r \end{aligned}$$

For $EH_{v\mu}$ modes only,

$$\begin{aligned} E_r &= -EJ_{v+1}(K_{v\mu}r) \cos v\phi \\ E_\phi &= -EJ_{v+1}(K_{v\mu}r) \sin v\phi \\ H_r &= -\frac{1}{\eta_1} E_\phi \\ H_\phi &= \frac{1}{\eta_1} E_r \end{aligned} \quad (11.131)$$

The expressions for the $TE_{0\mu}$ and $TM_{0\mu}$ modes are calculated later in Eqs. (11.136) through (11.138).

11.3.1 Sketching Hybrid Mode Patterns

Let us draw a few mode patterns using the field expressions in Eqs. (11.130) and (11.131). The first drawing is the HE_{11} mode, which is the simplest and also the most important mode, as it is the only mode in a single-mode fiber. Equation (11.130) with $v = 1$ gives

$$\begin{aligned} E_{r1} &= EJ_0(K_{11}r) \cos \phi \\ E_{\phi 1} &= -EJ_0(K_{11}r) \sin \phi \\ H_{r1} &= -\frac{1}{\eta_1} E_{\phi 1} \\ H_{\phi 1} &= \frac{1}{\eta_1} E_{r1} \end{aligned} \quad (11.132)$$

The top row of Fig. 11.21a illustrates the HE_{11} mode. Field lines of E and H at strategic points are drawn first, in the left and center diagrams. Note that the positive

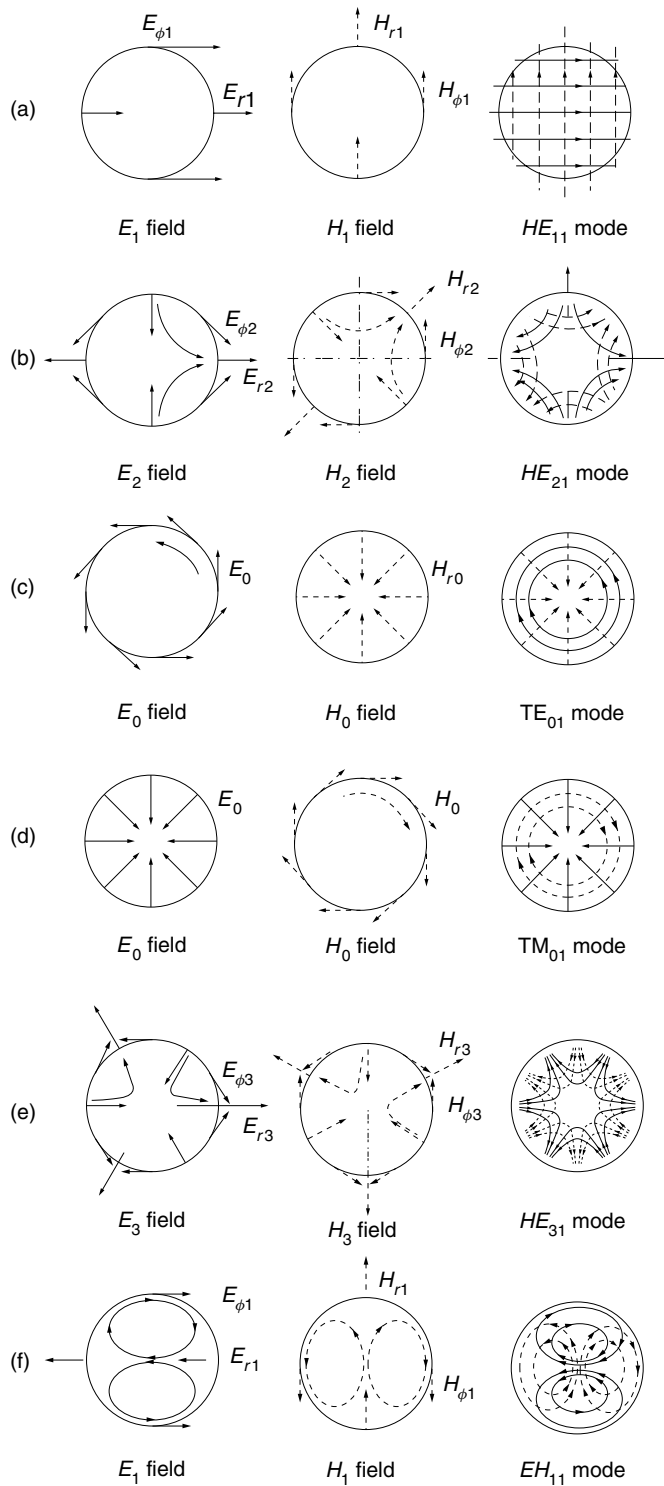


Figure 11.21 Mode patterns in a step-index fiber. The z axis is out of the page. The solid lines represent the E field and the dotted lines represent the H field.

directions of E_r and E_ϕ are in the directions of increasing r and ϕ , respectively. In the left diagram, the extrema of E_{r1} and $E_{\phi1}$ are drawn, and in the center diagram those of H_{r1} and $H_{\phi1}$ are drawn. The lines of the extrema are connected to complete the field pattern. The completed drawings are shown on the right-hand side. In the cylindrical coordinate system, $\hat{\mathbf{r}} \times \hat{\boldsymbol{\phi}} = \hat{\mathbf{z}}$, where $\hat{\mathbf{r}}$, $\hat{\boldsymbol{\phi}}$ and $\hat{\mathbf{z}}$ are unit vectors in the r , ϕ , and z directions. The positive $\hat{\mathbf{z}}$ direction is out of the page. That is why all Poynting vectors $\mathbf{E} \times \mathbf{H}$ point out of the page. A special characteristic of the HE_{11} mode pattern is that the E and H field lines make a square grid. There are two extrema in the ϕ direction and there is only one extremum in the r direction.

Next, the HE_{21} mode is drawn. With $\nu = 2$ and $\mu = 1$, Eq. (11.130) becomes

$$\begin{aligned} E_{r2} &= EJ_1(K_{21}r) \cos 2\phi \\ E_{\phi2} &= -EJ_1(K_{21}r) \sin 2\phi \\ H_{r2} &= -\frac{1}{\eta_1} E_{\phi2} \\ H_{\phi2} &= \frac{1}{\eta_1} E_{r2} \end{aligned} \quad (11.133)$$

Drawings of the HE_{21} mode are shown in Fig. 11.21b. The HE_{21} mode has four extrema in the ϕ direction and one extremum in the r direction. By connecting these extrema smoothly, the field patterns are completed.

Next, an attempt will be made to draw the patterns for the TE_{01} and TM_{01} modes. In these cases, A or B becomes zero. Equations (11.130) and (11.131) were derived using the relationship Eq. (11.121), which cannot be used for $A = 0$. The best approach in this case is to start from the original differential equations.

With $\nu = 0$, Eqs. (11.31) and (11.32) change to

$$\Phi'' = 0 \quad (11.134)$$

$$F'' + \frac{1}{r}F' + [(nk)^2 - \beta^2]F = 0 \quad (11.135)$$

The solution of Eq. (11.134) is a constant* and that of Eq. (11.135) is the zero-order Bessel function and the solution becomes

$$\begin{aligned} E_z &= A'J_0(Kr) \\ H_z &= B'J_0(Kr) \end{aligned} \quad (11.136)$$

The other components will be found from Eqs. (11.62) through (11.65) with $A = A'$ and $B = B'$. With the TE_{01} mode, $A' = 0$ and $\nu = 0$, and the components are

$$\begin{aligned} E_{r0} &= 0 \\ E_{\phi0} &= \frac{j\omega\mu}{K} B'J_1(Kr) \\ H_{r0} &= -\frac{j\beta}{K} B'J_1(Kr) \\ H_{\phi0} &= 0 \end{aligned} \quad (11.137)$$

* The solution $\Phi = a\phi$ cannot satisfy Eq. (11.39) unless $a = 0$.

Both the E_ϕ and H_r components are constant with respect to ϕ , and the mode pattern is cylindrically symmetric. The pattern is shown in Fig. 11.21c.

Next, the TM_{01} mode will be calculated in a similar manner. Equation (11.136) with $B' = 0$ is put into Eqs. (11.62) through (11.65). The results are

$$\begin{aligned} E_{r0} &= -\frac{j\beta}{K}A'J_1(Kr) \\ E_{\phi0} &= 0 \\ H_{r0} &= 0 \\ H_{\phi0} &= -\frac{j}{K}\omega\epsilon_1A'J_1(Kr) \end{aligned} \quad (11.138)$$

The mode pattern of the TM_{01} mode is shown in Fig. 11.21d below that of the TE_{01} mode. If E and H are exchanged, TM_{01} is obtained from TE_{01} . They are complementary patterns.

The HE_{31} and EH_{11} that generate an LP_{21} mode (see Problem 11.4) will now be drawn. These modes have the same cutoffs (see Problem 11.3) but have different field patterns. Equation (11.130) for the $HE_{\nu\mu}$ modes with $\nu = 3$ gives

$$\begin{aligned} E_r &= EJ_2(Kr) \cos 3\phi \\ E_\phi &= -EJ_2(Kr) \sin 3\phi \\ H_r &= -\frac{1}{\eta_1}E_\phi \\ H_\phi &= \frac{1}{\eta_1}E_r \end{aligned} \quad (11.139)$$

The field pattern of HE_{31} is shown in Fig. 11.21e. Equation (11.131) for the $EH_{\nu\mu}$ modes with $\nu = 1$ and $\mu = 1$, gives

$$\begin{aligned} E_r &= -EJ_2(Kr) \cos \phi \\ E_\phi &= -EJ_2(Kr) \sin \phi \\ H_r &= -\frac{1}{\eta_1}E_\phi \\ H_\phi &= \frac{1}{\eta_1}E_r \end{aligned} \quad (11.140)$$

The field pattern for EH_{11} is drawn in Fig. 11.21f at the bottom of the figure. Both HE_{31} and EH_{11} have one extremum in the r direction, but HE_{31} has six extrema in the ϕ direction, while EH_{11} has two extrema in the ϕ direction. That is, there are 2ν extrema in the ϕ direction and μ extrema in the r direction with either pattern.

11.3.2 Sketching Linearly Polarized Mode Patterns

As mentioned in Section 11.2.5.2, the combination of the $HE_{m+1\mu}$ and $EH_{m-1\mu}$ mode generates the $LP_{m\mu}$ mode.

We will demonstrate graphically that the addition of the HE_{21} and TM_{01} mode patterns in Figs. 11.21b and 11.21d generates the LP_{11} mode. While the x components of the E fields cancel each other, the y components of the fields add together and the E field of the LP_{11} mode is

$$E_x = 0$$

$$E_y = 2E$$

Similarly, the x components of H add, while the y components cancel each other, and the H field of the LP_{11} mode becomes

$$H_x = 2H$$

$$H_y = 0$$

Because $E_x = 0$ and $H_y = 0$, the new mode created by the two modes is indeed a linearly polarized (LP) mode. Figure 11.22 shows the field pattern of the LP_{11} mode. The shaded area represents the intensity of the Poynting vector.

It will now be shown that cancellation of the E_x and H_y fields takes place between $HE_{\nu+1\mu}$ and $EH_{\nu-1\mu}$ for any value of ν (excluding $\nu < 2$). Referring to Fig. 11.23, the E_r and E_ϕ components are decomposed into E_x and E_y components as

$$E_x = E_r \cos \phi - E_\phi \sin \phi \quad (11.141)$$

$$E_y = E_r \sin \phi + E_\phi \cos \phi$$

The expressions for E_r and E_ϕ from Eq. (11.130) are inserted into Eq. (11.141) to obtain the fields for the $HE_{\nu+1\mu}$ mode, and likewise, those of Eq. (11.131) are inserted into Eq. (11.141) to obtain the fields for the $HE_{\nu-1\mu}$ mode. For example, the x

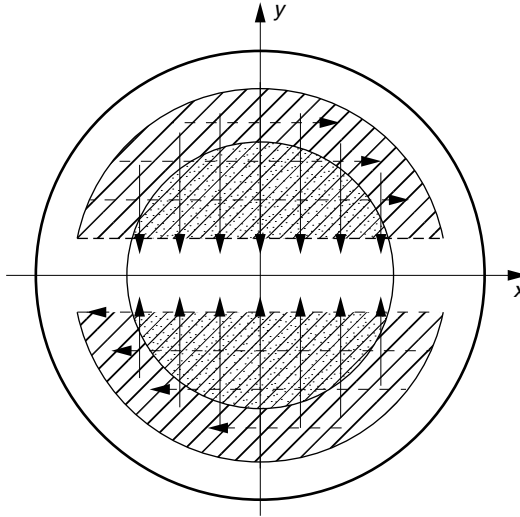


Figure 11.22 Field pattern of the LP_{11} mode.

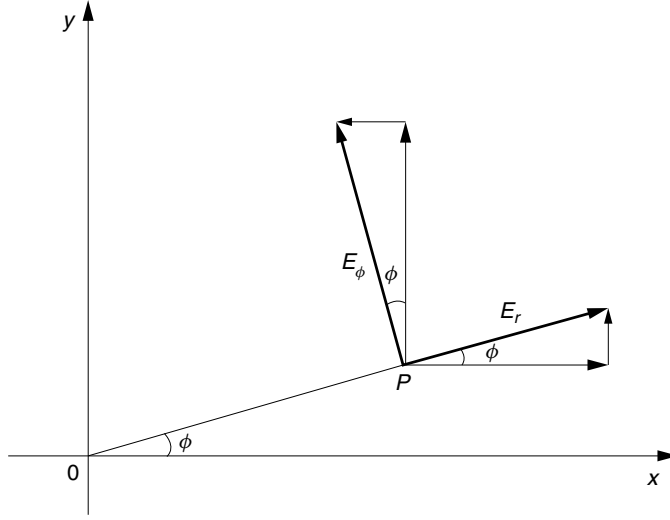


Figure 11.23 Relationship between components in cylindrical and rectangular coordinates.

component of the $HE_{v+1\mu}$ mode, E_x^{HE} , is given by

$$\begin{aligned} E_x^{HE} &= EJ_v(Kr)[\cos(\nu+1)\phi \cos \phi + \sin(\nu+1)\phi \sin \phi] \\ &= EJ_v(Kr) \cos \nu\phi \end{aligned} \quad (11.142)$$

A summary of all the field components is

$$\begin{aligned} E_x^{HE} &= \cos \nu\phi & E_x^{EH} &= -\cos \nu\phi \\ E_y^{HE} &= -\sin \nu\phi & E_y^{EH} &= -\sin \nu\phi \\ H_x^{HE} &= \sin \nu\phi & H_x^{EH} &= \sin \nu\phi \\ H_y^{HE} &= \cos \nu\phi & H_y^{EH} &= -\cos \nu\phi \end{aligned} \quad (11.143)$$

where $EJ_v(Kr)$ or $HJ_v(Kr)$ is suppressed. The addition of the $HE_{v+1\mu}$ and $EH_{v-1\mu}$ fields gives the $LP_{v\mu}$ fields. From Eq. (11.143), this addition gives

$$\begin{aligned} E_x^{HE} + E_x^{EH} &= 0 \\ E_y^{HE} + E_y^{EH} &= -2EJ_v(Kr) \sin \nu\phi \\ H_x^{HE} + H_x^{EH} &= 2HJ_v(Kr) \sin \nu\phi \\ H_y^{HE} + H_y^{EH} &= 0 \end{aligned} \quad (11.144)$$

Thus, the $LP_{v\mu}$ mode has only E_y and H_x components, and neither the E_x nor the H_y component exists. Moreover, E_y and H_x have the same distribution functions. It should be noted that the pattern $(\sin \phi)$ is antisymmetric with respect to ϕ and thus

this LP mode is called the $LP_{\nu\mu}^{\text{odd}}$ or $LP_{\nu\mu}^o$ mode. Figure 11.24 shows the field pattern of the $LP_{\nu\mu}$ mode.

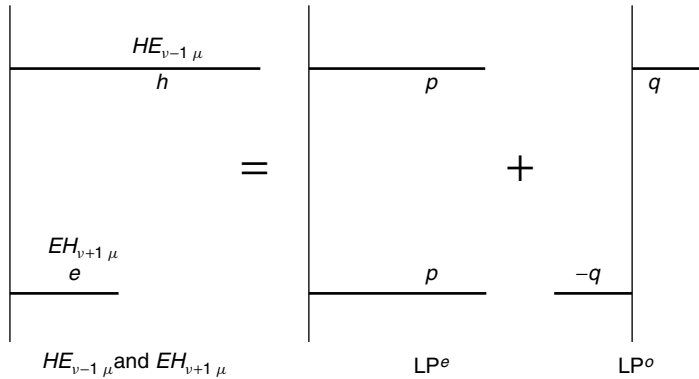
So far, it has always been assumed that both the magnitude and the phase of the $HE_{\nu+1\mu}$ and $EH_{\nu-1\mu}$ modes are identical. A different pattern would be generated, for instance, if the phase of $HE_{\nu+1\mu}$ were shifted π radians from that of $EH_{\nu-1\mu}$. In such a case, the components of the $LP_{\nu\mu}$ mode from Eq. (11.143) become

$$\begin{aligned} E_x &= 2EJ_\nu(Kr) \cos \nu\phi \\ H_y &= 2HJ_\nu(Kr) \cos \nu\phi \\ E_y &= H_x = 0 \end{aligned} \quad (11.145)$$

Because $E_y = 0$ and $H_x = 0$, this mode also classifies as a linearly polarized mode, but this time the LP mode is called $LP_{\nu\mu}^{\text{even}}$ or $LP_{\nu\mu}^e$ because of the symmetry of the pattern ($\cos \nu\phi$) with respect to ϕ . With an arbitrary combination of amplitude and phase, the composite modes generated from $HE_{\nu+1\mu}$ and $EH_{\nu-1\mu}$ consist of both $LP_{\nu\mu}^{\text{odd}}$ and $LP_{\nu\mu}^{\text{even}}$ modes.

Example 11.3 Suppose that an $HE_{\nu-1\mu}$ mode and an $EH_{\nu+1\mu}$ mode are in phase but their amplitudes are different and are given by h and e , respectively. What are the amplitudes of the $LP_{\nu\mu}^{\text{odd}}$ and $LP_{\nu\mu}^{\text{even}}$ modes?

Solution The amplitudes h and e can be divided into p , which is the magnitude of LP^o , and q , which is the magnitude of LP^e as



From the diagram

$$\begin{aligned} h &= p + q \\ e &= p - q \end{aligned}$$

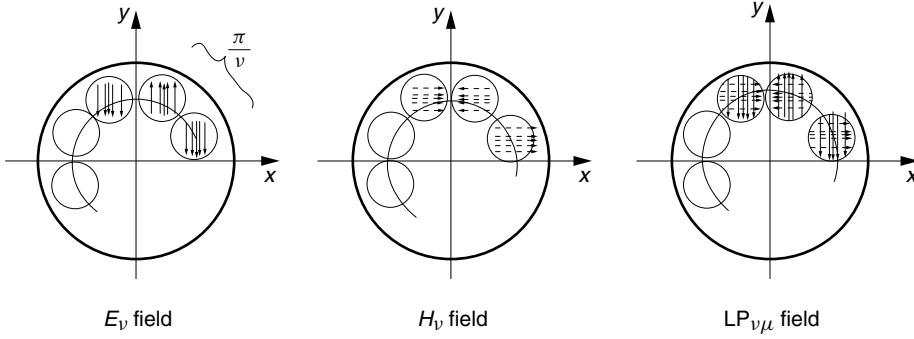


Figure 11.24 Field pattern of $LP_{\nu\mu}$ mode.

Solving for p and q , the magnitudes of LP^e and LP^o are given by

$$p = \frac{h + e}{2}$$

$$q = \frac{h - e}{2}$$

□

11.4 DUAL-MODE FIBER

A dual-mode fiber transmits both the dominant LP_{01} mode and the next higher order LP_{11} mode. The dual-mode fiber is made by setting the normalized radius V within the range of

$$2.405 < V < 3.832$$

which corresponds to the values between the first zero of $J_0(Ka)$ and the second zero of $J_1(Ka)$. The mode pattern of the LP_{01} mode (HE_{11} mode) is shown in Fig. 11.21a, and the LP_{11} mode is shown in Fig. 11.22.

The two modes in a dual-mode fiber behave as if two separate waves are propagating in one fiber. This feature is especially useful in a fiber sensor interferometer (explained below) because the interferometer is more stable when the two waves propagate in the same fiber rather than in two separate fibers.

Figure 11.25 shows the geometry of a dual-mode fiber strain gauge. A short section (20–30 cm) of dual-mode fiber is spliced to a single-mode fiber at both ends. The relative phase between the LP_{01} and LP_{11} modes shifts as the modes propagate due to the difference in the propagation constants. In order to excite both the LP_{01} and LP_{11} modes, the splices between the single-mode fiber and the dual-mode fiber are off center. At the input end, the E fields of the LP_{01} and LP_{11} modes in the encircled input portion of Fig. 11.25 are in phase, but after a distance of $L_B/2$, say, the E fields of the LP_{01} and LP_{11} modes in the encircled output portion of Fig. 11.25 are out of phase. When this occurs, the output from the single-mode fiber is at a minimum. After another $L_B/2$ of propagation, the output pattern becomes the same as the input pattern.

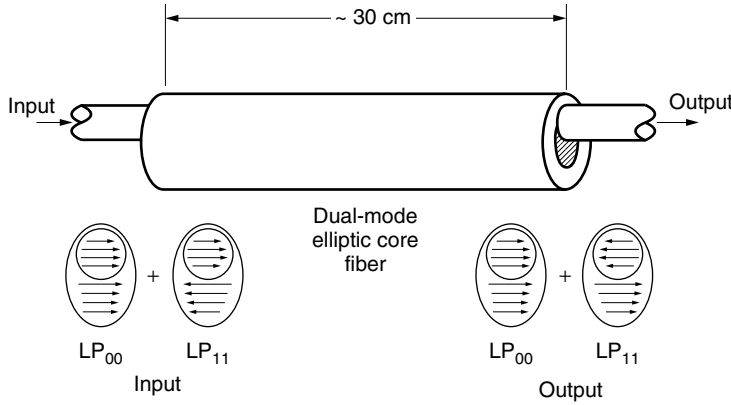


Figure 11.25 A strain gauge made out of a dual-mode fiber. (After F. Blaha.)

The length L_B is called the *coupling length* and is expressed as

$$L_B = \frac{2\pi}{\beta_{01} - \beta_{11}} \quad (11.146)$$

where β_{01} and β_{11} are the propagation constants of the LP_{01} and LP_{11} modes.

For instance, if the length of the dual-mode fiber sensor section is 30 cm and $L_B = 270 \mu\text{m}$, the percentage change in fiber length due to stretching that would be required to vary the light output from the minimum to the maximum is

$$\frac{L_B/2}{L} = \frac{0.135}{300} = 4.5 \times 10^{-4}$$

If 1% of the change from the maximum to minimum is measurable, then the sensitivity of such a sensor is 4.5×10^{-6} . The sensor employs an elliptic core dual-mode fiber, because, as mentioned in Section 11.1.5, the elliptic core fiber preserves the state of polarization of the light. In this way, fluctuations of the output power due to fluctuations in the relative directions of polarization of the LP_{01} and LP_{11} modes can be prevented.

Next, a tunable optical coupler constructed from dual-mode fiber will be described. Often, a slight but adjustable amount of light needs to be tapped off a main trunk line with minimum disturbance. The trunk line is single-mode fiber. Figure 11.26 shows the geometry. The coupler consists of a mode converter and a coupling section. In the mode converter section, either a set of teeth or rods creates a periodic microbending disturbance whose period is equal to the coupling length L_B . A portion of the energy of the LP_{01} mode in the trunk line is converted into that of the LP_{11} mode depending on the degree of the disturbance. Both LP_{01} and LP_{11} modes enter the coupling section. Even though the tap-off fiber is a normal dual-mode fiber, the main trunk line is gradually tapered from the dual-mode into a single-mode fiber in the coupling section. The tap-off of a particular wavelength is possible by using a longer converter section [22].

Finally, an application of the dual-mode fiber to a dispersion compensator will be described. Another feature of the dual-mode fiber is that the LP_{11} mode has an exceptionally large negative dispersion parameter when it is operated near its cutoff,

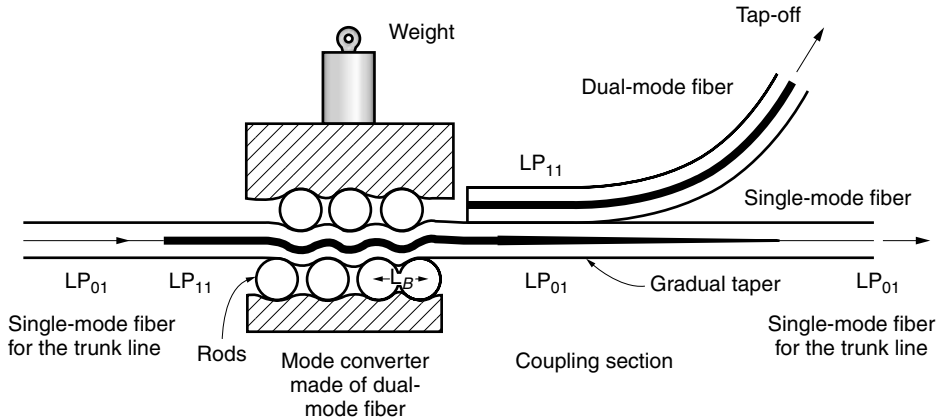


Figure 11.26 Tunable optical coupler for tapping off the trunk line.

and this can be used as a dispersion compensator. A dispersion compensator made out of a dual-mode fiber can provide the same amount of dispersion as a step-index single-mode fiber but with opposite sign, thereby establishing a zero-dispersion light transmission system. Figure 11.27a shows an experimental setup for demonstrating the effectiveness of the dual-mode fiber dispersion compensator. One of the 3-dB coupler output ports monitors the pulse shape after transmission through 50 km of single-mode step-index fiber with dispersion parameter $D = +15.8 \text{ ps}/(\text{km} \cdot \text{nm})$. The other output port of the 3-dB coupler monitors the signal that has made a round trip through 720 m of elliptic core dual-mode fiber with $D = -600 \text{ ps}/(\text{km} \cdot \text{nm})$ over and above the 50 km of step-index single-mode fiber. A mode converter is inserted between the single-mode and dual-mode fibers to convert the LP_{01} mode into the LP_{11} mode.

Near the reflecting mirror, a 90° polarization rotator is installed so as to remove the effect of the birefringence of the compensator's elliptic core fiber. As shown in Fig. 11.18, the LP_{11} mode consists of TE_{01} , TM_{01} , and HE_{21} modes. Their propagation constants are very close but slightly different from each other and could be a source of mode dispersion. This problem, however, is removed by using the elliptic core mode converter as in this system.

Figure 11.27b illustrates the effectiveness of the dispersion compensator [23]. The top figure shows the waveform of the input light pulses. The middle figure shows the waveform distorted by the dispersion of the 50-km step-index single-mode fiber. The pulse shape is unrecognizable. The bottom figure shows the waveform recovered by going through the $720 \times 2\text{-m}$ dual-mode dispersion compensator fiber. A more quantitative description of the dispersion compensator will be provided in Section 11.6 and Section 11.7.

11.5 PHOTOIMPRINTED BRAGG GRATING FIBER

When a germanium-doped (GeO_2 -doped) fiber is exposed to a high-intensity ultraviolet light, the glass is bleached and its index of refraction is permanently altered. The amount of change in the refractive index varies from 10^{-5} to 10^{-3} [24,25]. Such a phenomenon is called the *photosensitivity* of the GeO_2 -doped fiber.

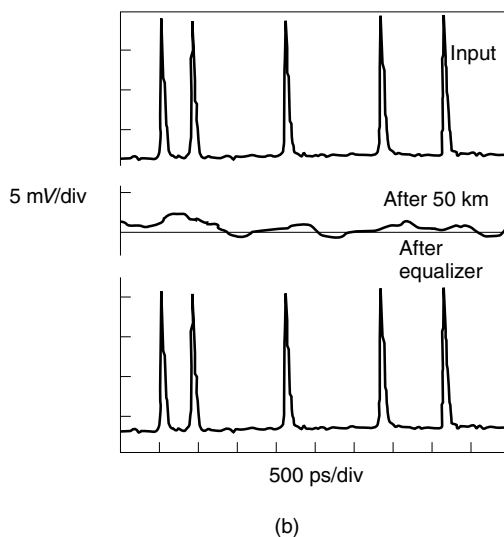
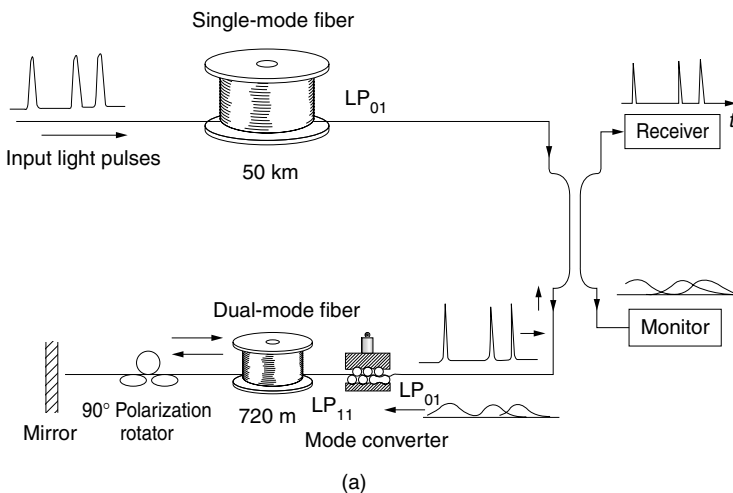


Figure 11.27 Dispersion compensation by a dual-mode fiber. (a) Experimental setup to demonstrate the effectiveness of the dual-mode fiber dispersion compensator. (b) Pulse shapes before and after the compensation. (Courtesy of C. D. Poole et al. [23].)

Photobleaching, however, does not take place in pure silica glass. A fiber consisting of a germanium-doped core surrounded by pure fused silica cladding is ideal for writing a Bragg grating reflector inside the fiber core. Various applications of the fiber Bragg grating have been explored in the fields of fiber lasers, optical communication devices, and fiber sensors.

11.5.1 Methods of Writing Photoinduced Bragg Gratings in an Optical Fiber

The Bragg gratings can be written either by internal or external illumination of the bleaching light.

11.5.1.1 Internal Writing

A high-power ($\sim \text{GJ}/\text{cm}^2$) visible range laser light, for example, argon ion laser light at 488 nm, is injected into a single-mode germanium-doped core fiber terminated with a mirror, as shown in Fig. 11.28. The standing wave inside the optical fiber photoimprints a Bragg grating with the same pattern as the standing wave. The merit of this method is its simplicity, but the drawbacks are that the same pattern is generated throughout the fiber and the period of the grating is changed only by changing the source. Moreover, it requires a high-intensity source.

11.5.1.2 Holographic Writing

A UV light interference pattern [24] externally illuminates a germanium-doped optical fiber, as shown in Fig. 11.29. The interference pattern is formed by an excimer laser operating at a wavelength of 249 nm. The geometry of the arrangement is designed to confine the interference pattern to the plane of the fiber. The UV-absorbing polymer coating of the optical fiber has to be stripped and recoated. Alternatively, it is also possible to write the grating as the fiber is drawn in the tower just before the polymer coating is applied if the laser source is pulsed with a pulse width of about 20 ns [26].

The required power for writing by means of UV light reduces to $1 \text{ kJ}/\text{cm}^2$, which is one-millionth of what is required for writing by means of visible light.

The photosensitivity can be augmented by loading the fiber with H_2 . The fiber is placed in pressurized H_2 gas at an elevated temperature ($250\text{--}400^\circ\text{C}$) for weeks. The change in the index of refraction reaches as high as $\Delta = 0.5\%$, which is comparable to the refractive index step Δ between the core and cladding of a step-index fiber [27]. Alternatively, the so-called flame brushing method [28], which repeatedly brushes the fiber by a flame fueled by hydrogen, augments the photosensitization almost as much as the H_2 gas immersion method. Even though the loss of the fiber is increased by hydrogen loading, the length of the fiber grating is normally less than a few centimeters, and the loss due to hydrogen exposure is not significant.

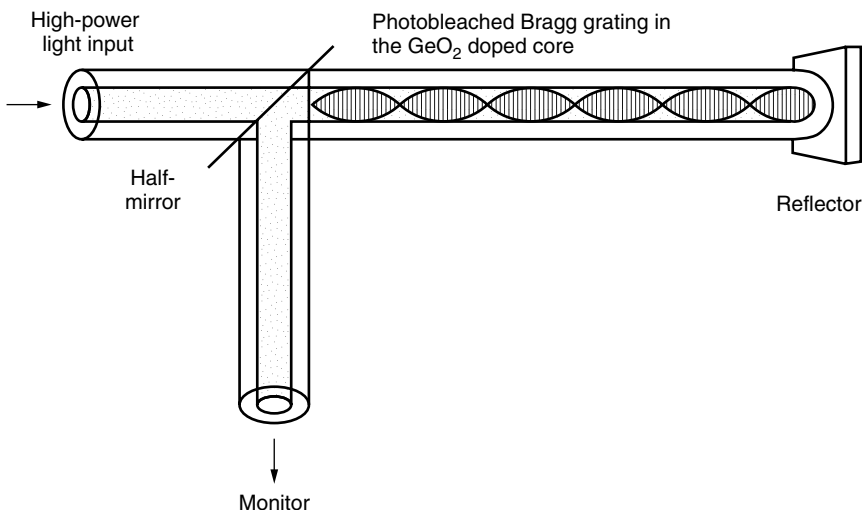


Figure 11.28 Arrangement for internally writing a Bragg grating in the fiber core by generating a standing wave in the core.

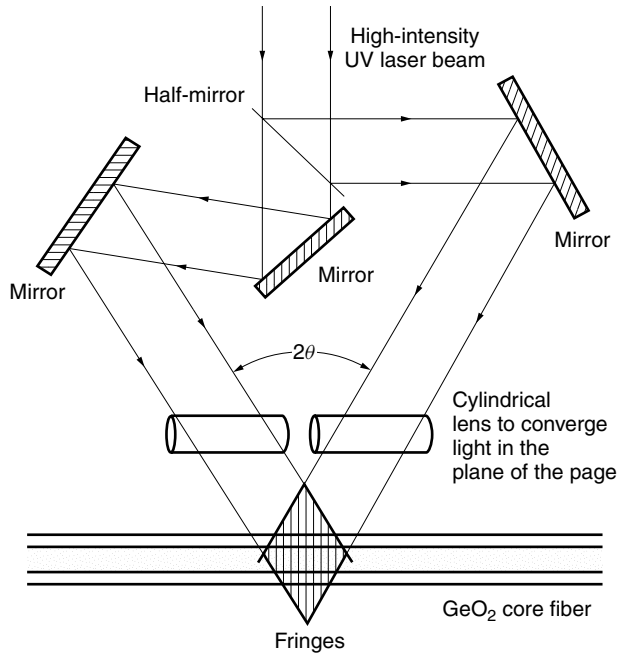


Figure 11.29 An interferometric arrangement for externally writing a Bragg grating in the fiber core.

11.5.1.3 Point-by-Point Writing

A UV laser beam is focused onto the photosensitive optical fiber. After each irradiation, the fiber is translated in the axial direction of the fiber by a computer controlled microtranslation stage. The grating is written one fringe at a time. The advantages of this method are that a laser beam of high intensity is obtainable because the beam is focused; and there is freedom in the selection of the shape, intensity, and period of the written pattern [29].

11.5.1.4 Writing by a Phase Mask

A prefabricated phase mask is used to imprint the pattern onto the optical fiber either in contact or near contact with the fiber. The normal incident UV laser beam bleaches the optical fiber according to the phase mask pattern. The advantages of this method are the flexibility in the patterns of the written grating and the easier handling of the writing apparatus. Figure 11.30 shows a photograph of a photoinduced Bragg grating written on the core of a D-fiber [30].

11.5.2 Applications of the Photoinduced Bragg Gratings in an Optical Fiber

The photoinduced Bragg grating acts as a wavelength-selective component in some fiber lasers, such as the one shown in Fig. 14.67d in Chapter 14. Besides the simplicity of the construction, a special feature of this fiber laser is that the wavelength of the laser can be shifted by simply stretching the fiber laser including the intracore Bragg reflector by means of a piezoexpander. This is possible because the change in the resonance wavelength of the Bragg reflector tracks that of the laser cavity [31].

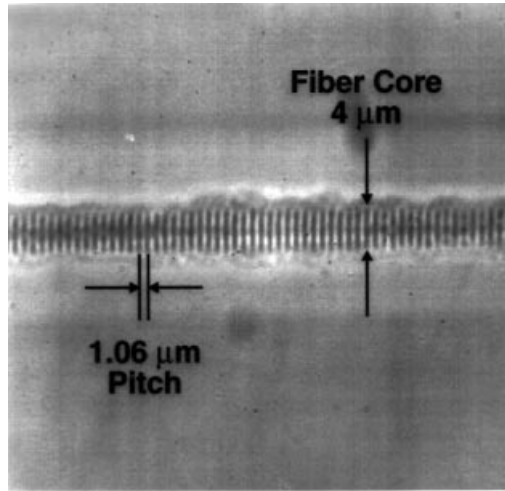


Figure 11.30. A photograph of a photoinduced Bragg grating written on the core of a D fiber. A phase contrast microscope was used. (Courtesy of B. Malo et al. [30].)

Another application of the photoinduced Bragg grating is as a band-stop optical filter. The rejection bandwidth of the apodized (see Section 1.4.2) Bragg reflector is approximately 0.2 nm with a rejection of 40 dB [32]. The transmission loss outside the stop band is less than 0.01 dB.

The demand for band-pass filters is higher than for band-stop filters. However, by combining the Bragg grating fiber with other optical devices, the band-stop characteristics can be converted into the complement characteristics of a band-pass filter.

For example, one way of achieving this conversion is by adding a 50–50 (or 3 dB) Mach–Zehnder fiber coupler [33]. A demultiplexer system containing a Mach–Zehnder coupler and photoinduced Bragg gratings is shown in Fig. 11.31. As this is an interesting application of fiber gratings, the function of this system will be explained in detail, starting with the ideal Mach–Zehnder coupler shown in Fig. 11.31a. Note that the power ratio is $1/2$ but the amplitude ratio is $1/\sqrt{2}$.

Let us say the amplitude of the incident light is a and is applied only to port ①. The light power is equally split between ports ③ and ④, and the amplitudes are $a/\sqrt{2}$ each. In addition to the light being split, there is a $\pi/2$ -radian phase difference between outputs ③ and ④. If output ③ that has travelled from port ① to port ③ taking the route straight through the coupling section (called the bar mode) is $a/\sqrt{2}$, then output ④ that has traveled from port ① to port ④ taking the route across the coupling section is $ja/\sqrt{2}$ (called the cross mode).

Next, a 100% Bragg grating reflector at λ_3 is installed in both the ③ and ④ arms, as shown in Fig. 11.31b. Wavelength division multiplexed (WDM) light containing wavelengths λ_1 , λ_2 , λ_3 , λ_4 , and λ_5 with identical amplitudes a is incident into port ①. Only the λ_3 component is reflected back toward ports ① and ②. The light reflected back toward port ① is considered first. The light reflected from port ③ to ① is the bar mode and $(a/\sqrt{2})(1/\sqrt{2}) = a/2$. Reflection from port ④ to ① is the cross mode and $(ja/\sqrt{2})(j/\sqrt{2}) = -a/2$. Thus, reflections from ③ and ④ cancel each other in port ① and there is no reflected light at port ①.

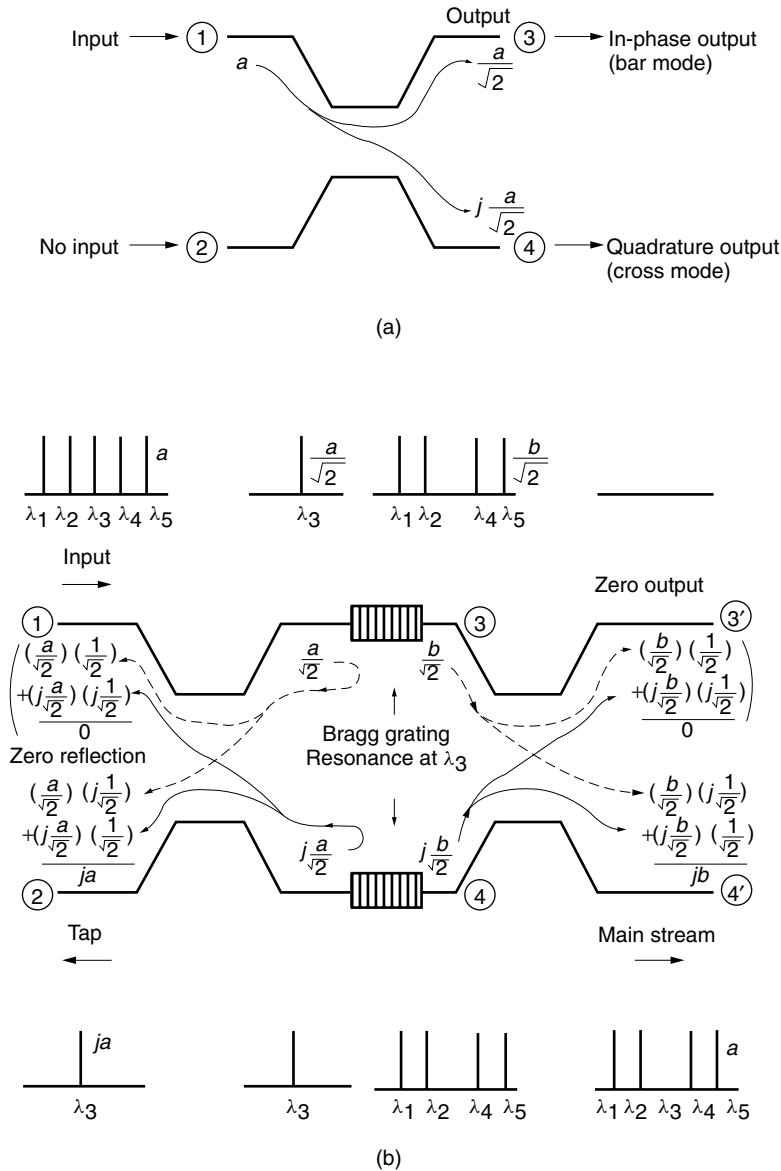


Figure 11.31 Fiber demultiplexer using photoimprinted Bragg reflectors. (a) Principle of the Mach-Zehnder interferometric fiber coupler. (b) Fiber demultiplexer.

Next, the light reflected back toward port ② is considered. The reflected light from ③ to ② is the cross mode and $(a/\sqrt{2})(j/\sqrt{2}) = ja/2$. The reflected light from ④ to ② is the bar mode and $(ja/\sqrt{2})(1/\sqrt{2}) = ja/2$. The reflections from ③ and ④ interfere constructively in port ② and the output from port ② is ja . In conclusion, the light power at λ_3 is fully reflected back to ② but none to ①.

Next, the paths of the rest of the spectra that were not reflected by the Bragg grating reflectors in arms ③ and ④ are considered. Additional 3-dB Mach-Zehnder couplers

are connected to ports ③ and ④ as shown in Fig. 11.31b. The contribution to ③ from ③ is the bar mode and $(b/\sqrt{2})(1/\sqrt{2}) = b/2$; and that from ④ to ③ is the cross mode and $(ja/\sqrt{2})(jb/\sqrt{2}) = -b/2$. Thus, the contributions to ③ cancel each other and no output light is present at ③. Similarly, the contribution from port ③ to ④ is the cross mode and $b/\sqrt{2}(j/\sqrt{2}) = jb/2$; and that from ④ to ④ is the bar mode and $(jb/\sqrt{2})(1/\sqrt{2}) = jb/2$. Thus, contributions from ③ and ④ add constructively and the output from ④ is jb . Full power comes out of port ④ and no power comes out of port ③.

In conclusion, the Bragg grating fiber combined with the Mach–Zehnder interferometer performs the function of wavelength-selective tapping in the WDM stream. The same setup can be also used for a wavelength-selective insertion into a WDM channel (see Problem 11.8).

If the couplers attached to the output of ports ③ and ④ are replaced by light absorbers, then the device becomes an ordinary band-pass filter.

Another important application of the photoimprinted Bragg grating is in the field of fiber sensing. The intracore Bragg grating can be used for sensing strain, vibration, and temperature. The presence of strain or vibration will perturb the period of the Bragg grating and will cause a shift of the resonant wavelength. A perturbation occurs in the presence of a temperature fluctuation, which alters the refractive index of the Bragg grating and shifts the resonant wavelength. One advantage of the Bragg grating sensor over other fiber sensors is that the quantity being measured is a wavelength shift rather than a change in the received power level, and significantly better accuracy and signal-to-noise level are obtainable.

Another advantage is the ease in multiplexing the sensors. Figure 11.32 shows schemes for multiplexing sensors. Sensors of different resonant wavelengths are

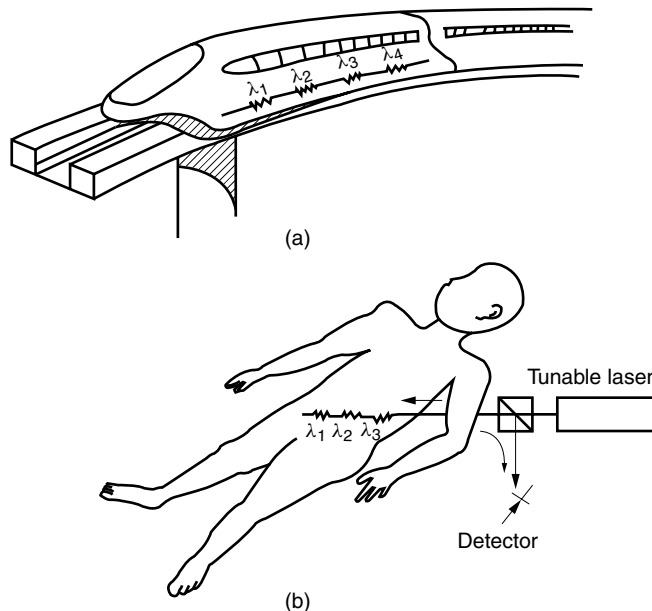


Figure 11.32 Multiplexed fiber Bragg grating sensors for (a) strain and (b) temperature.

imprinted along an optical fiber. A change in a particular resonant wavelength identifies which sensor is being affected [34]. The number of multiplexed sensors can be large because the transmission loss through a sensor at the off-resonance wavelengths is of the order of 0.01 dB. Strain sensors are multiplexed in Fig. 11.32a. Figure 11.32b shows a similar arrangement for temperature sensors. The latter is well suited to measuring temperature profiles, and it is the profile of the temperature rather than an isolated point temperature that is essential to tumor or cancer diagnosis and treatment [35].

Another application as a device in fiber-optic communication is the chirped aperiodic Bragg grating used to compensate for the dispersion of the optical fiber transmission line. This, however, will be explained in the next section, together with other types of dispersion compensators.

11.6 DEFINITIONS ASSOCIATED WITH DISPERSION

Before going into the design of the dispersion-shifted fiber, a few definitions are presented.

11.6.1 Definitions of Group Velocity and Group Delay

The speed of propagation of the envelope of the modulated light is the *group velocity*. The modulated light contains a band of frequency components centered around the carrier frequency. The shape of the envelope of the received light can be calculated by decomposing it into the component sinusoidal waves by the Fourier transform method. The envelope of the received light can be reconstructed by summing up the spectral components, each of which has propagated by its own phase velocity to the receiver. The time for the modulated light to reach the receiver determines the group velocity [36].

A simpler method can provide the same value as obtained by the Fourier transform method when the spread of the frequency spectrum due to the modulation is moderate. As a modulated wave, the simple method uses a beat wave composed of only two frequency components: $\omega + \delta\omega$ and $\omega - \delta\omega$, where ω is the carrier angular frequency. The beat wave is

$$e^{-j(\omega+\delta\omega)t+j(\beta+\delta\beta)z} + e^{-j(\omega-\delta\omega)t+j(\beta-\delta\beta)z} = 2\cos(\delta\omega \cdot t - \delta\beta \cdot z)e^{-j\omega t + j\beta z}$$

The first term is the envelope and the second term, the carrier. The velocity of the envelope can be found in the same way that the phase velocity was found in Section 1.1. The peak of the envelope appears whenever the value of the bracket is zero. At $t = 0$, the peak is at $z = 0$. At $t = \Delta t$, the peak appears at $\Delta z = (\delta\omega/\delta\beta)\Delta t$; hence, the velocity v_g of the envelope is

$$v_g = \frac{d\omega}{d\beta} \quad (11.147)$$

Note that $\delta\beta$ contains not only the change $\delta\omega$ but also the frequency dependence of the refractive index n , for instance, in an unbound medium $\beta = n\omega/c$. Another noteworthy

point is that when the received waveform is too distorted, Eq. (11.147) for the group velocity is no longer valid.

We will now define a quantity related to the group velocity called the group delay. The time it takes for the envelope (or a pulse) to travel a unit distance (for instance, 1 km) is called the *group delay* τ . The group delay is the inverse of the group velocity and

$$\tau = \frac{d\beta}{d\omega} \quad (11.148)$$

Using the relationship $k = \omega/c$, τ can be written in terms of k as

$$\tau = \frac{1}{c} \frac{d\beta}{dk} \quad (11.149)$$

11.6.2 Definition of the Dispersion Parameter

If every frequency spectrum in the pulse has the same group delay, they all arrive with the same delay, and the received envelope is not distorted. On the other hand, if some spectra arrive earlier than others, the received pulse is distorted. In other words, if the derivative of τ with respect to λ or ω is not zero, there is a distortion. The degree of distortion due to the dispersion is expressed by

$$D = \frac{d\tau}{d\lambda} \quad (11.150)$$

and D is called the *dispersion parameter*.

11.7 DISPERSION-SHIFTED FIBER

A rudimentary description of a dispersion-shifted fiber was given in Section 11.1.4. The amount of waveguide dispersion is adjusted such that cancellation with the material dispersion takes place at $\lambda = 1.55 \mu\text{m}$, where the transmission loss of the optical fiber is lowest. Here, we undertake a more quantitative approach to shifting the dispersion-free wavelength. The calculation starts with the expression for the propagation constant β from which the group delay $\tau = d\beta/d\omega$ is obtained. In turn, the group delay τ provides the dispersion parameter $D = d\tau/d\lambda$. Finally, the condition that makes $D = 0$ at the desired wavelength $\lambda = 1.55 \mu\text{m}$ is found. Since the derivation is rather lengthy, the group delay and the dispersion parameter are covered separately.

11.7.1 Group Delay in an Optical Fiber

Inserting Eq. (11.120) into (11.149), the group delay in an optical fiber is found to be

$$\tau = \frac{1}{c}(N_1 - N_w) \quad (11.151)$$

where

$$N_1 = \frac{d(n_1 k)}{dk}$$

or

$$N_1 = n_1 + k \frac{dn_1}{dk} \quad (11.152)$$

and where

$$N_w = \frac{d}{dk} [n_1 k \Delta (1 - b)]$$

or

$$N_w = (n_1 - n_2) \left[1 - \frac{d(kb)}{dk} \right] \quad (11.153)$$

In the above derivation as well as subsequent derivations, assumptions such as

$$\begin{aligned} \frac{d}{dk} (n_1 - n_2) &\div 0 \\ \frac{d}{dk} \sqrt{n_1 - n_2} &\div 0 \\ \frac{d}{d\lambda} \sqrt{n_1^2 - n_2^2} &\div 0 \end{aligned} \quad (11.154)$$

are made. These assumptions mean that the frequency dependence of n_1 can be assumed identical with that of n_2 . This is justifiable from the curves in Fig. 11.7.

First, Eq. (11.152) is considered. N_1 is called the *group index*. N_1 is conventionally tabulated in terms of λ , and an effort will be made to convert the variable accordingly.

$$\frac{dn_1}{dk} = \frac{dn_1}{d\lambda} \frac{d\lambda}{dk} \quad (11.155)$$

$$\frac{dk}{d\lambda} = -\frac{2\pi}{\lambda^2} \quad (11.156)$$

Combining Eq. (11.156) with (11.152) gives

$$N_1 = n_1 - \lambda \frac{dn_1}{d\lambda} \quad (11.157)$$

Note that the group index N_1 has nothing to do with the dimension of the fiber but depends on the material of the core and is associated with the curve of material dispersion in Fig. 11.9.

Next, Eq. (11.153) is considered. N_w is called the *waveguide index*. N_w is usually expressed in terms of the normalized radius V given by Eq. (11.77). We have

$$\frac{dV}{dk} = a \sqrt{n_1^2 - n_2^2} \quad (11.158)$$

where Eq. (11.154) was used.

Equation (11.158) is approximated as

$$\frac{dV}{dk} \div a \sqrt{2n_1(n_1 - n_2)} \quad (11.159)$$

Using Eq. (11.159) and

$$\frac{d}{dk} = \frac{dV}{dk} \frac{d}{dV}$$

the second term in the square brackets of Eq. (11.153) becomes

$$\frac{d(kb)}{dk} = a\sqrt{2n_1(n_1 - n_2)} \frac{d(kb)}{dV} \quad (11.160)$$

and with Eq. (11.158)

$$\frac{d(kb)}{dk} = \frac{V}{k} \frac{d(kb)}{dV}$$

Again using Eq. (11.159), we obtain

$$\frac{d(kb)}{dk} = b + V \frac{db}{dV}$$

and finally,

$$\frac{d(kb)}{dk} = \frac{d(Vb)}{dV} \quad (11.161)$$

Inserting Eq. (11.161) into (11.153) gives

$$N_w = (n_1 - n_2) \left(1 - \frac{d(Vb)}{dV} \right) \quad (11.162)$$

The numerical value of $d(Vb)/dV$ is readily available from Ref. 37, and the curve for the dominant mode HE_{11} is shown in Fig. 11.33.

Finally, the expression for the group delay becomes, from Eqs. (11.151), (11.157), and (11.162),

$$\tau = \frac{1}{c} \left[n_1 - \lambda \frac{dn_1}{d\lambda} - (n_1 - n_2) \left(1 - \frac{d(Vb)}{dV} \right) \right] \quad (11.163)$$

Now, all the preparation for calculating the dispersion has been completed.

11.7.2 Dispersion Parameter of an Optical Fiber

The dispersion parameter given by Eq. (11.150) is obtained by taking the derivative of Eq. (11.163) with respect to λ . Even though the first two terms of Eq. (11.163) are differentiated by λ , the last term is normally differentiated by V . Noting that

$$V = \frac{2\pi}{\lambda} a \sqrt{(n_1^2 - n_2^2)}$$

the derivative of V with respect to λ is

$$\frac{dV}{d\lambda} = -\frac{V}{\lambda} \quad (11.164)$$

where the assumption of Eq. (11.154) was used.

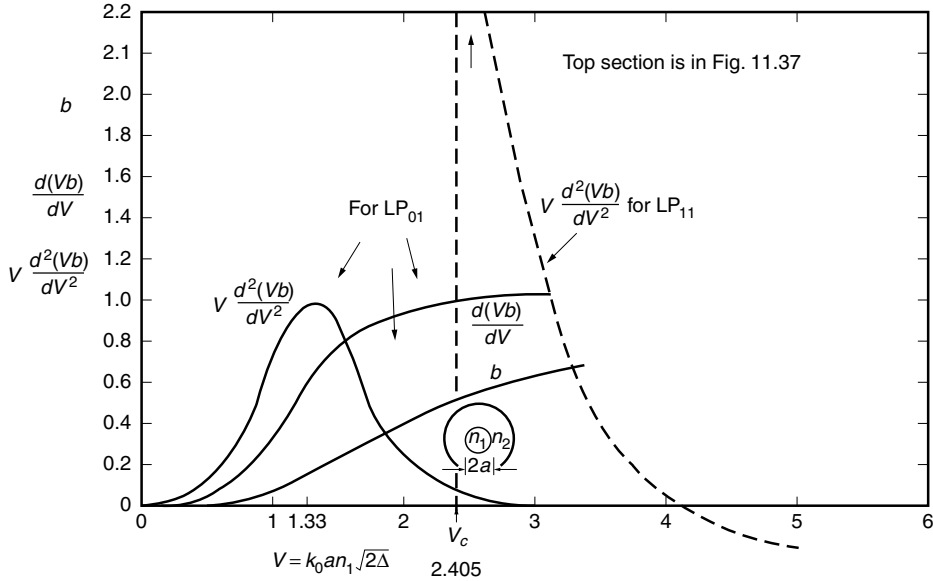


Figure 11.33 Values of b , $d(Vb)/dV$ and $Vd^2(Vb)/dV^2$. These values are used in the design of dispersion-shifted fibers and dispersion compensators. The graph of $Vd^2(Vb)/dV^2$ is shown for both the LP_{01} and LP_{11} modes. (After D. Gloge [37].)

Thus,

$$\frac{d}{d\lambda} = \frac{dV}{d\lambda} \frac{d}{dV} = -\frac{V}{\lambda} \frac{d}{dV} \quad (11.165)$$

Finally, with Eqs. (11.150), (11.154), (11.163), and (11.165), the dispersion parameter is

$$D = -\frac{\lambda}{c} \frac{d^2 n_1}{d\lambda^2} - \frac{n_1 \Delta}{c\lambda} V \frac{d^2(Vb)}{dV^2} \quad (11.166)$$

The first term of Eq. (11.166) has nothing to do with the structure of the fiber: it is associated with the core material and is called the *material dispersion*. The second term depends on the physical structure of the fiber and is called the *waveguide dispersion*.

The values of the first and second terms in Eq. (11.166) are of opposite signs in the region $\lambda > 1.27 \mu\text{m}$. If the magnitude of the waveguide dispersion is increased, the cancellation wavelength shifts to a longer wavelength. The dispersion-shifted fiber is designed such that the cancellation takes place at $\lambda = 1.55 \mu\text{m}$.

The waveguide dispersion D_w is given by the second term of Eq. (11.166). The general approaches to increasing D_w in an ordinary step-index configuration are the following:

1. Choose a value of V near $V = 1.33$, where $Vd^2(Vb)/dV^2$ is a maximum, as shown in Fig. 11.33.
2. Increase the difference $n_1 \Delta = n_1 - n_2$ in the indices of refraction between the core and cladding glasses. Excessive doping of the core in order to

increase the index of refraction is undesirable because of the increased Rayleigh scattering loss. Figure 11.34 shows the refractive index distribution of a low-loss dispersion-shifted fiber [38]. A combination of raising the core refractive index by doping with GeO_2 and lowering the cladding refractive index by doping with fluorine creates a low-loss dispersion-shifted fiber of 0.2 dB/km.

By alternating higher and lower indices of refraction radially in the cladding glass as shown in Fig. 11.35, it is also possible to fabricate an optical fiber whose dispersion is small for the entire wavelength region from $\lambda = 1.3$ to $1.55 \mu\text{m}$. A disadvantage of the dispersion-shifted fiber is the larger bending loss because of the smaller value of V ($V = 1.33$) mostly, $2.0 < V < 2.4$. Bending loss increases with decreasing V because γ is decreased and the confinement of the core light becomes poorer. The principle for

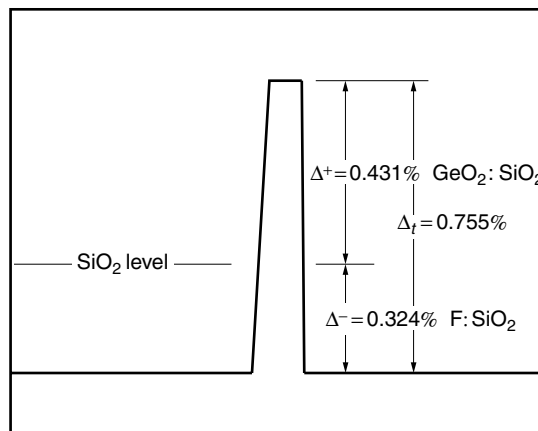


Figure 11.34 Profile of $1.55 \mu\text{m}$ zero-dispersion fiber. (After M. Ogai et al. [38].)

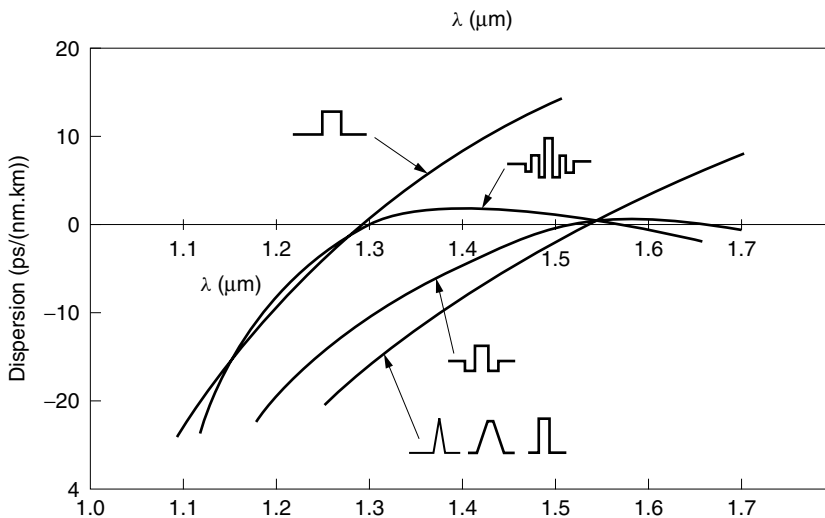


Figure 11.35 SM fiber profile and dispersion. (After H. Murata [39].)

designing a dispersion-shifted fiber will be explained using the example profile shown in Fig. 11.34.

Example 11.4 Design the radius of a dispersion-shifted fiber and its cladding refractive index n_2 using the diagrams in Figs. 11.9 and 11.33. The refractive index of the core is assumed to be $n_1 = 1.458$.

Solution First, we will find D_w . Then, we will select $V = 1.33$, where $Vd^2(Vb)/dV^2$ is a maximum, and determine Δ and a with the constraint of $V = 1.33$. From the second term of Eq. (11.166), the waveguide dispersion parameter D_w is

$$D_w = -\frac{n_1 \Delta}{c\lambda} V \frac{d^2(Vb)}{dV^2} \quad (11.167)$$

From Fig. 11.9, the value of waveguide dispersion that is needed to cancel the material dispersion at $\lambda = 1.55$ is

$$D_w = -28 \text{ ps}/(\text{km} \cdot \text{nm})$$

From the first approach mentioned earlier for increasing D_w , the point of operation in Fig. 11.33 is selected at

$$\begin{aligned} V &= 1.33 \\ V \frac{d^2(Vb)}{dV^2} &= 1 \end{aligned} \quad (11.168)$$

One has to be careful about the units because D_w is defined in terms of ps, km, and nm.

$$\begin{aligned} c &= \frac{3 \times 10^8 \times 10^{-3}}{10^{12}} = 3 \times 10^{-7} \text{ km/ps} \\ \lambda &= 1550 \text{ nm} \end{aligned}$$

Even though both km and nm are distance dimensions, km belongs to only the distance of propagation, whereas nm is used for the wavelength of the light and the radius of the core. Thus, Eq. (11.167) becomes

$$\begin{aligned} 28 &= (1) \frac{n_1 \Delta}{(3 \times 10^{-7})(1550)} \\ n_1 \Delta &= 0.0130 \\ \Delta &= 0.89\% \end{aligned}$$

Hence,

$$n_2 = 1.445$$

The value of a is found from

$$V = 1.33$$

and

$$1.33 = \frac{2\pi}{1.55}(1.458)\sqrt{2 \times 0.0089}a$$

$$a = 1.69 \mu\text{m}$$

The profile therefore becomes tall and slender, similar to the profile shown in Fig. 11.34. \square

In the above example, the value of $Vd^2(bV)/dV^2 = 1$ at $V_{\max} = 1.33$ was used to design the physical parameters of the dispersion-shifted fiber, but as the bit rate of the pulse modulation of the light becomes increasingly high, say, 100 Gb/s ($\Delta\lambda \doteq 1 \text{ nm}$ or $\Delta V = 10^{-3}$), then $Vd^2(bV)/dV^2$ can no longer be considered constant. A correction factor associated with

$$\frac{d}{dV} \left(V \frac{d^2(Vb)}{dV^2} \right)$$

has to be taken into consideration. This is called the third-order dispersion effect [40]. This effect cannot be tolerated in long-haul transmission with high bit rates. As a countermeasure, compensators that create a dispersion equal and opposite to the third-order dispersion effect are installed after a specified distance of transmission in the dispersion-shifted fiber. These compensators cancel the third-order dispersion effect. The next section is devoted to the explanation of the dispersion compensator in general, not just a compensator for the third-order dispersion.

11.8 DISPERSION COMPENSATOR

Even though the dispersion-shifted fiber is an attractive solution to the dispersion problems of an optical fiber, replacing all the existing fiber transmission lines with dispersion-shifted fiber would be a very expensive undertaking. Enough single-mode step-index fiber has already been installed to wrap around the globe more than several times. If we try to make use of already installed single-mode fiber, serious limitations are encountered at high bit rates. For example, if 10 Gb/s of RZ coded pulses were to be transmitted, the maximum span distance of an uncompensated single-mode fiber is less than 100 km.

Dispersion compensators are used to break the bit rate barrier in already installed optical fibers [41]. Three different kinds of dispersion compensators are described next.

11.8.1 Phase Conjugation Method

As mentioned in Section 8.12, if a phase conjugate mirror is installed midway through the transmission fiber, a close approximation of the original pulse shape is recovered at the receiver.

11.8.2 Bragg Grating Method

The Bragg grating method uses a chirped Bragg grating reflector photoimprinted in the core of the fiber [42]. As shown in Fig. 11.36, the pitch of the Bragg grating is

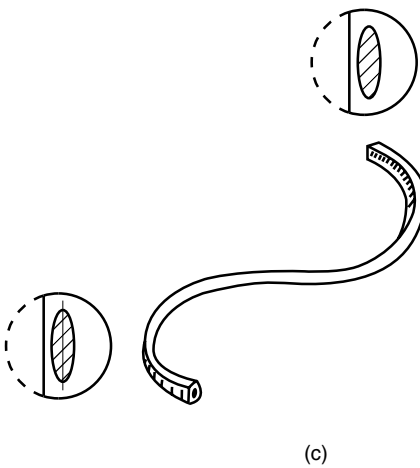
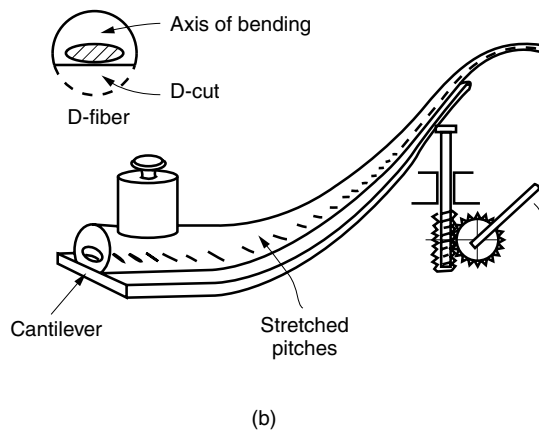
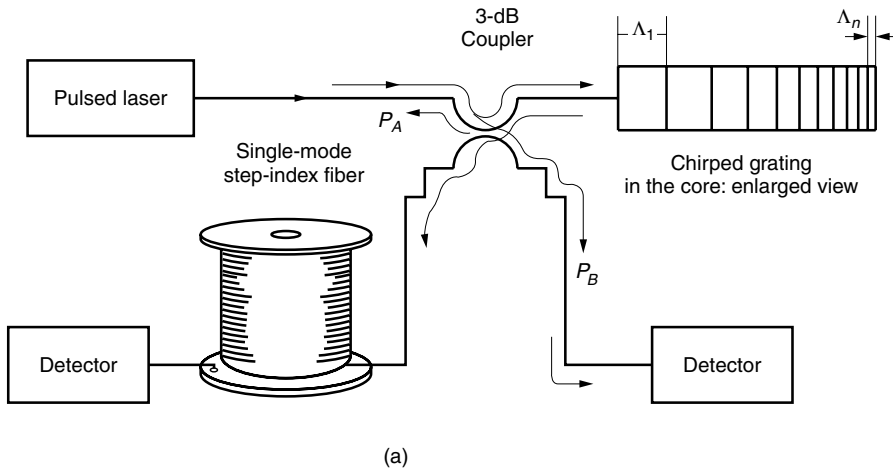


Figure 11.36 Dispersion compensation using a chirped Bragg reflector photoimprinted in the fiber. (a) Experimental setup. (b) Chirping achieved by single bending. (c) Chirping obtained by double bending.

decreased (chirped) with distance. When this grating is used as a reflector, the longer wavelength components penetrate shallower into the grating, and the turnaround time is shorter. Thus, the group delay τ decreases with wavelength and the waveguide dispersion parameter D_w becomes a negative quantity; the dispersion parameter of the step-index fiber, which is a positive quantity, can be canceled out.

The total length of the chirped Bragg reflector is calculated for the example of 10 Gb/s of RZ coded pulses in a single-mode fiber. The spread of the arrival time is $\Delta t = 35$ ps. The distance that the light pulse travels in a $n = 1.55$ fiber core in 35 ps is $(c/n)\Delta t = 6.8$ mm and the required length of the Bragg reflector is 3.4 mm.

With the arrangement shown in Fig. 11.36a, the pulse goes around the chirped reflector first before entering the single-mode step-index fiber; but the order can be reversed. Because of the 3-dB fiber coupler in this configuration, half the power is lost when entering the chirped reflector, and another half of the power is lost getting out of the chirped reflector. This power loss associated with the coupler can be avoided by modifying the Mach–Zehnder interferometer shown in Fig. 11.31. The modification consists of replacing the two ordinary gratings with two chirped gratings.

Besides using a chirped photomask, a chirped fiber grating can be fabricated by simply bending a flexible cantilever, onto which a D-fiber written by a regular pitch grating is bonded. The axis of the bending of the D-fiber is laterally displaced from the center of the circular cross section because of the D-cut. If the fiber is bent with the D-cut facing away from the center of the bending, the pitch of the grating is expanded. If, however, the fiber is bent in the opposite way, the pitch will be shortened. In Fig. 11.36b [43], the fiber is bent in only one direction, while in Fig. 11.36c [44], there are two bends in opposite directions.

11.8.3 Dual-Mode Fiber Method

Dispersion compensation using a dual-mode fiber has already been mentioned briefly, but a more detailed explanation will be given here as to how a large negative waveguide dispersion parameter is obtainable from a dual-mode fiber.

According to Eq. (11.167), the waveguide dispersion parameter is influenced by the value of $Vd^2(Vb)/dV^2$. This value for the LP_{11} mode has been calculated by Poole et al. [45] and is shown in Fig. 11.37. The value asymptotically increases as the cutoff is approached and can provide a large negative waveguide dispersion parameter.

It is instructive to give a physical interpretation of why the LP_{11} mode displays such a large negative waveguide dispersion parameter. As indicated by Eq. (11.150), the variation of τ with respect to λ is the dispersion parameter D . Thus, D can be known by finding how τ changes with an increase in λ . From Eq. (11.77) as λ is increased, V decreases. From Fig. 11.17, a decrease in V causes a decrease in γ . The value of γ controls the field in the cladding, which is approximately expressed as $E_0e^{-\gamma r}$. The decrease in γ means more light energy propagates in the cladding whose index of refraction is smaller than that of the core. Consequently, a decrease in γ increases the group velocity, if the cladding is assumed to be an unbounded medium, and $v_g = c/n$, and hence decreases the group delay τ . In short, an increase in λ decreases τ and the waveguide dispersion parameter is a negative quantity.

Next, the reason for the large magnitude near the cutoff is considered. The shift of the energy into the cladding is controlled by $E_0e^{-\gamma r}$. For instance, the field at $r = a$ is expressed as $E_0e^{-\gamma a}$. The rate of change with γ , $d(E_0e^{-\gamma a})/d\gamma$, is largest when $\gamma = 0$. This is when the operating point is near or at the cutoff.

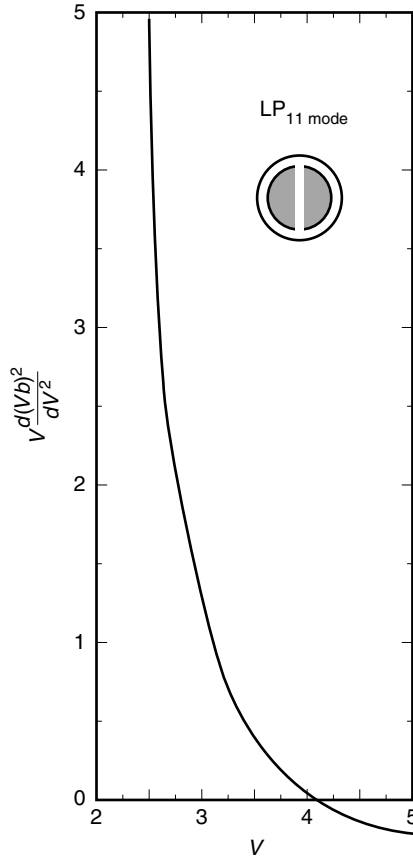


Figure 11.37 $Vd^2(Vb)/dV^2$ of LP_{11} versus V for calculating the dispersion parameter. (After C. D. Poole et al. [45].)

The actual values of D_w for the LP_{11} near the cutoff will be calculated in the next example.

Example 11.5 Determine the value of the waveguide dispersion parameter of a dual-mode fiber with the following physical parameters:

Wavelength of operation, $\lambda = 1.550 \mu\text{m}$

Core radius, $a = 2.1 \mu\text{m}$

Refractive index of the core, $n_1 = 1.460$

Relative core index step, $\Delta = 0.02$

Solution

$$\begin{aligned}
 V &= kan_1\sqrt{2\Delta} \\
 &= \frac{2\pi}{1.55}(2.1)(1.460)\sqrt{2(0.02)} = 2.49 > 2.40
 \end{aligned}$$

From Eq. (11.167) and Fig. 11.37,

$$\begin{aligned} D_w &= -\frac{n_1 \Delta}{c\lambda} V \frac{d^2(Vb)}{dV^2} \\ &= \frac{-(1.46)(0.02)(5)}{(3 \times 10^5 \times 10^{-12})(1550)} = -314 \text{ ps}/(\text{km} \cdot \text{nm}) \end{aligned}$$

The material dispersion D_m is 28 from Fig. 11.9. The dispersion parameter D is

$$D = D_m + D_w = 28 - 314 = -286 \text{ ps}/(\text{km} \cdot \text{nm}) \quad \square$$

Example 11.6 After 100 km of transmission through a step-index single-mode fiber, the dual-mode fiber specified in Example 11.5 is used as a dispersion compensator. What is the required length of the dual-mode fiber?

Solution The length of the dual-mode fiber required to cancel the total dispersion of the single-mode fiber is found. From Fig. 11.9 the dispersion constant D for a single mode step index fiber at $\lambda = 1.55 \mu\text{m}$ is $D = 17 \text{ ps}/(\text{km} \cdot \text{nm})$. We have

$$\begin{aligned} 17 \times 100 &= 286x \\ x &= 5.9 \text{ km} \end{aligned} \quad \square$$

11.9 RAY THEORY FOR GRADED-INDEX FIBERS

The refractive index of the core of a graded-index fiber varies with radius. This space dependence of n makes it very difficult to solve the wave equations (11.14) and (11.15). Ray theory [46,47], which is sometimes called geometrical optics, is often used instead of wave theory. Ray theory is approximate and assumes that the lightwave in a fiber is a plane wave that is changing its course according to the spatial variation of the refractive index. In ray theory, the procedure for solving the wave equation starts with reducing the wave equation to the eikonal equation. The eikonal equation is an approximate but simpler differential equation to solve for the spatial distribution of the phase. After finding the phase distribution, the path of light or wavenormal is found from its gradient. This approach assumes that any physical dimensions such as the fiber core and the fiber length are much larger than the wavelength of the light. In other words, ka is much larger than unity. The accuracy of the ray theory deteriorates as the dimensions approach the order of a wavelength.

Knowledge of the light path, however, leads to such important quantities as the propagation constant, modes, group delay, and dispersion of the multimode graded-index fiber.

11.9.1 Eikonal Equation

When the index of refraction n becomes *space dependent*, the exact solution of the wave equation

$$\nabla^2 u + [kn(r, \phi, z)]^2 u = 0 \quad (11.169)$$

is very difficult to obtain. As a matter of fact, solutions can be found in closed form for only a limited number of functions $n(r, \phi, z)$.

The procedure begins by assuming a solution of the wave equation of the form

$$u = e^{jkL(r, \phi, z)} \quad (11.170)$$

We will seek $L(r, \phi, z)$ that satisfies the wave equation. Before putting Eq. (11.170) into (11.169), $\nabla^2 u$ will be calculated. A useful identity for $\nabla^2 u$ is

$$\nabla^2 u = \nabla \cdot \nabla u \quad (11.171)$$

where ∇u in cylindrical coordinates is

$$\nabla u = \hat{\mathbf{r}} \frac{\partial u}{\partial r} + \hat{\phi} \frac{1}{r} \frac{\partial u}{\partial \phi} + \hat{\mathbf{k}} \frac{\partial u}{\partial z}$$

From Eq. (11.170), ∇u is expressed as

$$\nabla u = \underbrace{jk e^{jkL}}_f \underbrace{\nabla L}_A \quad (11.172)$$

Equation (11.172) is the product of the scalar function

$$f = jk e^{jkL} \quad (11.173)$$

and the vector function

$$\mathbf{A} = \nabla L \quad (11.174)$$

The second operation $\nabla \cdot$ in Eq. (11.171) is performed using the identity

$$\nabla \cdot (f \mathbf{A}) = f \nabla \cdot \mathbf{A} + (\nabla f) \cdot \mathbf{A} \quad (11.175)$$

With Eqs. (11.170) to (11.175), the wave equation of Eq. (11.169) is written as

$$\nabla^2 u + (kn)^2 u = \{jk \nabla^2 L - k^2 [(\nabla L) \cdot (\nabla L) - n^2]\} e^{jkL} = 0 \quad (11.176)$$

If k is much larger than unity, the k term is much smaller than the k^2 term and the first term in the bracket can be ignored. Thus, Eq. (11.176) becomes

$$|\nabla L|^2 = n^2 \quad (11.177)$$

Equation (11.177) is called the eikonal equation (meaning “image” in Greek). $|\nabla L|$ is the magnitude of the vector ∇L . L is called the eikonal and gives the specific phase distribution of the light.

Next, the eikonal of the light inside a graded-index fiber will be found. The eikonal equation, Eq. (11.177), in cylindrical coordinates is

$$\left(\frac{\partial L}{\partial r} \right)^2 + \left(\frac{1}{r} \frac{\partial L}{\partial \phi} \right)^2 + \left(\frac{\partial L}{\partial z} \right)^2 = n^2(r) \quad (11.178)$$

where the distribution of the index of refraction $n(r)$ is assumed cylindrically symmetric. The differential equation, Eq. (11.178), will be solved by separation of variables. Let the solution be of the form

$$kL = R(r) + \Phi(\phi) + Z(z) \quad (11.179)$$

Both sides of Eq. (11.178) are first multiplied by k^2 and Eq. (11.179) is inserted to obtain

$$\underbrace{(R')^2 - n^2(r)k^2 + \frac{1}{r^2}(\Phi')^2}_{-\beta^2} + \underbrace{(Z')^2}_{\beta^2} = 0 \quad (11.180)$$

Since the last term is the only variable in z , the condition that the equation be satisfied for any value of z in space is that the last term has to be constant, as designated by β^2 ; so

$$Z' = \pm\beta \quad (11.181)$$

and

$$Z = \pm\beta z \quad (11.182)$$

With Eq. (11.181), Eq. (11.180) becomes

$$\underbrace{r^2[R'^2 - (nk)^2 + \beta^2]}_{-v^2} + \underbrace{\Phi'^2}_{v^2} = 0 \quad (11.183)$$

For the same reason as before, Φ'^2 has to be a constant v^2 and

$$\Phi = \pm v\phi \quad (11.184)$$

From Eq. (11.183)

$$R' = \pm\sqrt{(nk)^2 - (v/r)^2 - \beta^2} \quad (11.185)$$

Only the plus signs will be taken up for now, and with the plus sign, Eq. (11.179) becomes

$$kL = \int \sqrt{(kn)^2 - (v/r)^2 - \beta^2} dr + v\phi + \beta z \quad (11.186)$$

Finally, the expression for the lightwave in the fiber is

$$u = \exp \left[j \int \sqrt{(kn)^2 - (v/r)^2 - \beta^2} dr + jv\phi + j\beta z \right] \quad (11.187)$$

Now that the phase distribution has been found, the direction of the wave normal or the light path can be calculated.

11.9.2 Path of Light in a Graded-Index Fiber

The light path can be found from the gradient of the phase contour; namely, $\nabla(kL)$ indicates the direction of the wavenormal. In order to make the wavenormal direction a unit vector \hat{s} , the quantity $\nabla(kL)$ has to be divided by its magnitude $|\nabla(kL)|$:

$$\hat{s} = \frac{\nabla(kL)}{|\nabla(kL)|} \quad (11.188)$$

From Eq. (11.177), the unit vector \hat{s} is written as

$$\hat{s} = \frac{\nabla L}{n} \quad (11.189)$$

One more expression is needed to find the path of light; that is, the expression for the light path using the position vector. As shown in Fig. 11.38, the position vector \mathbf{R} is generated by connecting a point on the light path with the origin of the coordinate system. The cord $\Delta\mathbf{R}$ in Fig. 11.38 is an approximation to the path of light. The shorter $\Delta\mathbf{R}$ is, the better $\Delta\mathbf{R}$ matches the path of light. As soon as $\Delta\mathbf{R}$ exactly matches the path, the magnitude becomes zero and there is no vector. This situation can be remedied by expressing the path by

$$\hat{s} = \lim_{s \rightarrow 0} \frac{\Delta\mathbf{R}}{\Delta s} \quad (11.190)$$

where Δs is the length measured along the actual light path. The limit operation leads to

$$\hat{s} = \frac{d\mathbf{R}}{ds} \quad (11.191)$$

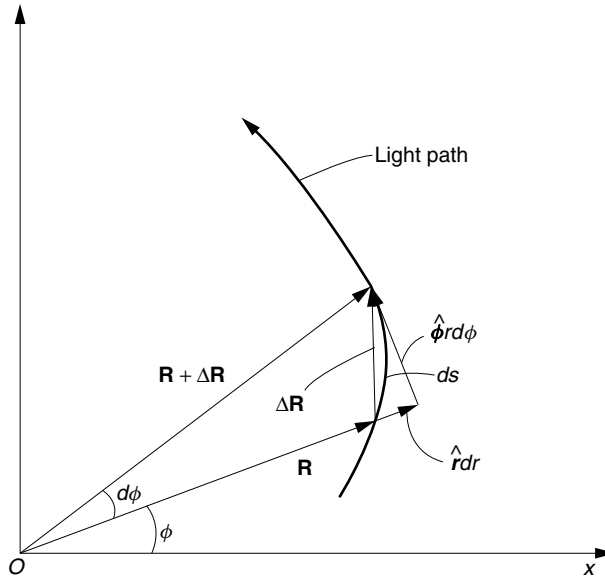


Figure 11.38 Expression for the light path in terms of the position vector.

where, from Fig. 11.38, $d\mathbf{R}$ is given by

$$d\mathbf{R} = \hat{\mathbf{r}}dr + \hat{\boldsymbol{\phi}}rd\phi + \hat{\mathbf{k}}dz \quad (11.192)$$

The combination of Eqs. (11.189) with (11.191) gives the expression for the light path

$$n \frac{d\mathbf{R}}{ds} = \nabla L \quad (11.193)$$

Insertion of Eqs. (11.186) and (11.192) into Eq. (11.193) gives

$$nk \frac{dr}{ds} = \sqrt{(nk)^2 - (v/r)^2 - \beta^2} \quad (11.194)$$

$$nkr \frac{d\phi}{ds} = \frac{1}{r}v \quad (11.195)$$

$$nk \frac{dz}{ds} = \beta \quad (11.196)$$

Division of Eq. (11.196) by (11.194) and division of Eq. (11.195) by (11.194) finally gives

$$z = \int \frac{\beta}{\sqrt{[n(r)k]^2 - (v/r)^2 - \beta^2}} dr \quad (11.197)$$

$$\phi = \int \frac{v}{r^2 \sqrt{[n(r)k]^2 - (v/r)^2 - \beta^2}} d\phi \quad (11.198)$$

Calculation of Eqs. (11.197) and (11.198) for a given distribution of $n(r)$ gives the expression for the light ray path.

Here we will consider the special case of a fiber with a quadratic distribution of $n^2(r)$ as

$$n^2(r) = n_c^2(1 - \alpha^2 r^2) \quad (11.199)$$

where α^2 is the refractive index gradient constant squared. A graded-index fiber with such a refractive index distribution is known as a Selfoc fiber.

After some manipulation, inserting Eq. (11.199) into (11.197) leads to

$$z = \frac{\beta}{2kn_c\alpha} \int \frac{dt}{\sqrt{q^2 - (t-p)^2}} \quad (11.200)$$

where

$$t = r^2 \quad (11.201)$$

$$p = \frac{(n_ck)^2 - \beta^2}{2(n_ck\alpha)^2} \quad (11.202)$$

$$q^2 = p^2 - \left(\frac{v}{n_ck\alpha} \right)^2 \quad (11.203)$$

The integral of Eq. (11.200) gives

$$t = p + q \sin \frac{2n_c k \alpha}{\beta} (z - z_0) \quad (11.204)$$

From Eqs. (11.201) and (11.204), r^2 wobbles with z . This suggests that the path is a helix with an elliptic cross section, which will be verified later. The maximum radius is $r = \sqrt{p+q}$ and the minimum is $r = \sqrt{p-q}$.

Next, the integral of Eq. (11.198) will be calculated. It is quite similar to Eq. (11.197) and it becomes

$$\phi = \frac{\nu}{2n_c k \alpha} \int \frac{dt}{t \sqrt{q^2 - (t-p)^2}} \quad (11.205)$$

After the change of variable

$$x = t - p \quad (11.206)$$

and with the help of the following relationship from a table of integrals,

$$\int \frac{dx}{(c^2x + ab)\sqrt{b^2 - c^2x^2}} = \frac{1}{bc\sqrt{a^2 - c^2}} \sin^{-1} \frac{acx + bc}{c^2x + ab} \quad (11.207)$$

the integral of Eq. (11.205) is

$$\phi - \phi_0 = \frac{1}{2} \sin^{-1} \left(\frac{p(t-p) + q^2}{qt} \right) \quad (11.208)$$

where Eq. (11.203) was also used.

With Eq. (11.201), Eq. (11.208) becomes

$$\frac{1}{r^2} (p^2 - q^2) = p - q \sin 2(\phi - \phi_0) \quad (11.209)$$

Equation (11.209) will be rewritten in a more familiar form. Noting that

$$\sin 2(\phi - \phi_0) = \cos 2(\phi - \phi_0 - \pi/4)$$

we have

$$q \sin 2(\phi - \phi_0) = q \cos^2(\phi - \phi_0 - \pi/4) - q \sin^2(\phi - \phi_0 - \pi/4) \quad (11.210)$$

$$p = p [\cos^2(\phi - \phi_0 - \pi/4) + \sin^2(\phi - \phi_0 - \pi/4)] \quad (11.211)$$

Eq. (11.209) is rewritten as

$$1 = \frac{r^2 \cos^2(\phi - \phi_0 - \pi/4)}{p+q} + \frac{r^2 \sin^2(\phi - \phi_0 - \pi/4)}{p-q} \quad (11.212)$$

Changing into rectangular coordinates by noting

$$\begin{aligned} X &= r \cos(\phi - \phi_0 - \pi/4) \\ Y &= r \sin(\phi - \phi_0 - \pi/4) \end{aligned} \quad (11.213)$$

Eq. (11.212) becomes

$$\frac{X^2}{A^2} + \frac{Y^2}{B^2} = 1$$

with

$$\begin{aligned} A &= \sqrt{p+q} \\ B &= \sqrt{p-q} \end{aligned} \quad (11.214)$$

Now it has been verified that the cross section of the skew ray is an ellipse such as shown in Fig. 11.39.

Only the solutions with the positive sign in Eqs. (11.181), (11.184), and (11.185) have been considered, but the solutions with negative signs have to be added. The solutions with negative signs are again skewed but wound in the opposite sense. These two skew rays spiraling in opposite directions form a standing wave, which is precisely what the mode patterns are as will be mentioned in Section 11.9.5.

As v in Eq. (11.203) approaches zero, the ellipse shrinks into a line and the solution becomes that of a meridional ray.

As the skew ray encircles the fiber axis once, r^2 goes through a maximum and minimum twice. The advance in the z direction after one complete turn is the pitch of

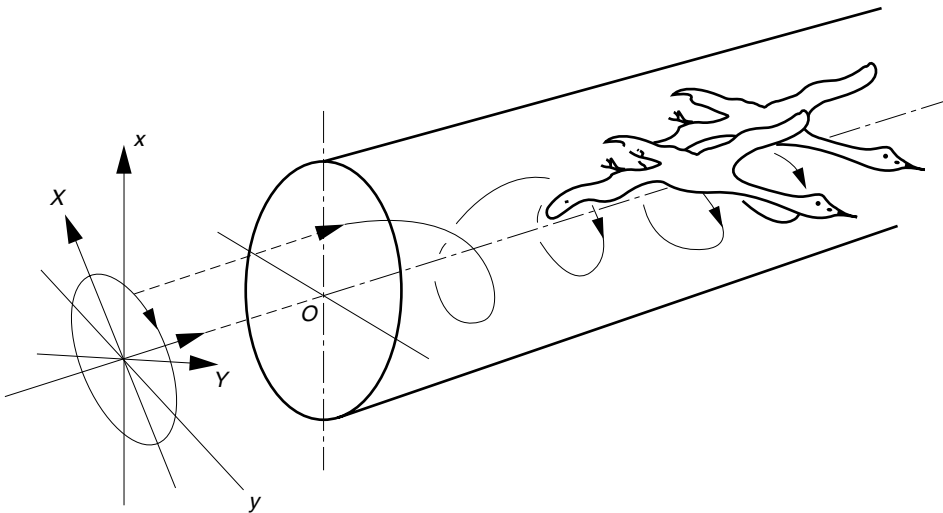


Figure 11.39 Path of a skew ray in a graded-index fiber.

the helix. From Eq. (11.204), the pitch ρ is found:

$$\frac{2n_c k \alpha}{\beta} \rho = 4\pi \quad (11.215)$$

$$\rho = 2\pi \frac{\beta}{n_c k \alpha} \quad (11.216)$$

For lower order modes, $\beta \doteq n_c k$ and

$$\rho \doteq \frac{2\pi}{\alpha} \quad (11.217)$$

Inside a Selfoc fiber with $\alpha = 0.01 \mu\text{m}^{-1}$, the pitch is about half a millimeter.

11.9.3 Quantization of the Propagation Constant in a Graded-Index Fiber

As the dimensions of the fiber are reduced, problems of quantization become important. Suppose that a light ray has a finite width with a taper in the direction transverse to the direction of propagation, like the wings of a bird in Fig. 11.39. A portion of the width (the wing of one bird) of the light interferes with the width (the wing of another bird) of the light of the previous turn. If the phases of the two waves are different, they destructively interfere and the amplitude decreases each time the ray encircles the fiber axis. Since the skew ray goes around the fiber axis more than 10^3 times in 1 meter, even a slight decrease in amplitude accumulates, and no propagation takes place. It is therefore necessary that the phase match completely each time ϕ advances by 2π , and hence ν in Eq. (11.184) has to be an integer:

$$\nu = 0, 1, 2, 3, \dots \quad (11.218)$$

There is another quantization. That is in the r direction. The skew ray waves toward and away from the axis between $r_{\min} = p - q$ and $r_{\max} = p + q$ according to Eq. (11.204). This wavy path can be pictured as a zigzag path in a curved slab guide wrapped around the fiber axis, where the width of this slab is $r_{\max} - r_{\min}$. If we interpret the wavy ray path as a zigzag path in a curved slab guide, then the optical width of such a slab guide has to be an integral multiple of π radians, as discussed in Section 9.7.4. Thus,

$$\mu\pi = \int_{r_{\min}}^{r_{\max}} \sqrt{(nk)^2 - (v/r)^2 - \beta^2} dr \quad (11.219)$$

The integrand of Eq. (11.219) has a square root, but the square root can be removed by converting the variable from r to z using Eqs. (11.194), (11.196), and (11.216):

$$\mu\pi = \frac{1}{\beta} \int_0^{\rho/4} [(nk)^2 - (v/r)^2 - \beta^2] dz \quad (11.220)$$

For convenience, the integral I of Eq. (11.220) is separated into two parts:

$$I_1 = \frac{1}{\beta} \int_0^{\rho/4} [(nk)^2 - \beta^2] dz \quad (11.221)$$

$$I_2 = \frac{1}{\beta} \int_0^{\rho/4} \left(\frac{v}{r}\right)^2 dz \quad (11.222)$$

where

$$I = I_1 - I_2 \quad (11.223)$$

Equation (11.204) is rewritten in terms of Eq. (11.216) as

$$r^2 = p + q \sin \frac{4\pi}{\rho} (z - z_0)$$

Setting $z_0 = \rho/8$ the above simplifies as

$$r^2 = p + q \cos \left(\frac{4\pi}{\rho} z \right) \quad (11.224)$$

With Eqs. (11.199), (11.202), and (11.224), after some manipulation the calculated integral I_1 becomes

$$I_1 = \frac{n_c k \alpha \pi}{2} p \quad (11.225)$$

The second integral I_2 can be calculated using the following formula from an integral table:

$$\int \frac{dx}{p + q \cos bx} = \frac{1}{b \sqrt{p^2 - q^2}} \cos^{-1} \left(\frac{q + p \cos bx}{p + q \cos bx} \right) \quad (11.226)$$

The result of integral I_2 is

$$I_2 = \frac{\pi}{2} v \quad (11.227)$$

From the results of I_1 and I_2 , Eq. (11.220) becomes

$$\mu \pi = \frac{n_c k \alpha \pi}{2} p - \frac{\pi}{2} v$$

Using Eq. (11.202), p is rewritten and the quantization formula becomes

$$2n_c k \alpha (v + 2\mu) = n_c^2 k^2 - \beta_{v\mu}^2 \quad (11.228)$$

Finally, the propagation constant $\beta_{\mu v}$ of a graded-index fiber is

$$\beta_{v\mu} = n_c k \sqrt{1 - \frac{2\alpha(v + 2\mu)}{n_c k}} \quad (11.229)$$

The mode number

$$N = v + 2\mu \quad (11.230)$$

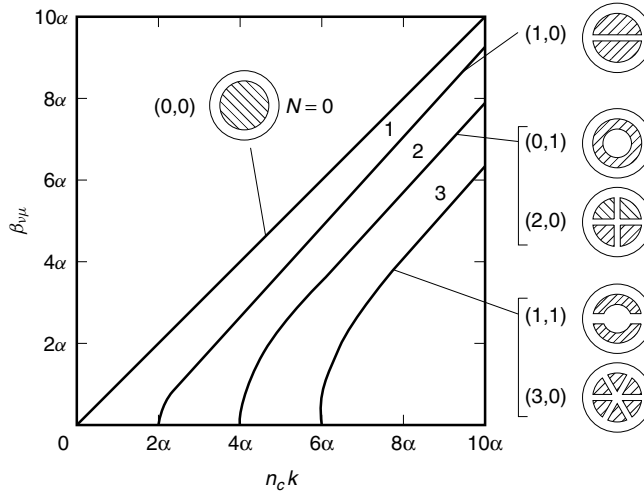


Figure 11.40 $\beta_{v\mu}$ versus $n_c k$.

is called the *principal mode number* of a graded-index fiber. The propagation constant $\beta_{v\mu}$ can be the same for different combinations of v and μ . Modes with the same N are degenerate modes. Figure 11.40 shows a graph of $\beta_{v\mu}$ versus $n_c k$ with N as a parameter. Both axes are graduated by α . $N = 0$ corresponds to the mode $(v, \mu) = (0, 0)$; $N = 1$ to $(1, 0)$; $N = 2$ to the degenerate modes of $(2, 0)$ and $(0, 1)$; and so forth. The condition for a single-mode graded-index fiber is

$$\frac{n_c k}{\alpha} < 2 \quad (11.231)$$

11.9.4 Dispersion of Graded-Index Fibers

Now that the expression for $\beta_{v\mu}$ has been obtained, it is possible to calculate the group delay. Taking the derivative of Eq. (11.228) with respect to k , the group delay Eq. (11.149) for the Selfoc fiber is obtained as

$$\tau = \frac{N_c}{c} \frac{n_c k}{\beta_{v\mu}} \left(1 - \alpha \frac{(v + 2\mu)}{n_c k} \right) \quad (11.232)$$

where

$$N_c = \frac{d(n_c k)}{dk} \quad (11.233)$$

and where N_c is the group index at the fiber axis.

Next, the material and waveguide dispersion of a single-mode graded-index fiber will be calculated. For a single-mode fiber, Eqs. (11.229) and (11.232) with $\mu = v = 0$ give

$$\tau = \frac{N_c}{c} \quad (11.234)$$

Analogous to the derivation of Eq. (11.157), N_c is expressed as

$$N_c = n_c - \lambda \frac{dn_c}{d\lambda} \quad (11.235)$$

By taking the derivative of Eq. (11.235), the dispersion parameter of the graded-index fiber therefore becomes

$$D = -\frac{\lambda}{c} \frac{d^2 n_c}{d\lambda^2} \quad (11.236)$$

Thus, unlike a step-index single-mode fiber, a graded-index single-mode fiber has only material dispersion and no waveguide dispersion.

Next, the mode dispersion of a multimode graded-index fiber will be calculated. The factor $(\nu + 2\mu)$ can be eliminated from Eq. (11.232) by expressing it in terms of $\beta_{\nu\mu}$ using Eq. (11.228) as

$$\tau = \frac{N_c}{c} \frac{n_c k}{2\beta_{\nu\mu}} \left[1 + \left(\frac{\beta_{\nu\mu}}{n_c k} \right)^2 \right] \quad (11.237)$$

If the ray of the lowest mode propagates straight without any zigzag or encircling of the fiber axis and Eq. (11.234) is satisfied, the group delay τ_c is

$$\tau_c = \frac{N_c}{c} \quad (11.238)$$

From Eqs. (11.237) and (11.238), the mode dispersion, which is the difference $(\tau - \tau_c)$ in the group delays, is

$$\Delta\tau = \frac{N_c}{c} \frac{(1 - \beta/n_c k)^2}{2(\beta/n_c k)} \quad (11.239)$$

where subscripts $\nu\mu$ were suppressed.

Referring to Fig. 11.41, β for the (ν, μ) mode makes an angle δ with the fiber axis, and

$$\cos \delta = \frac{\beta}{n_c k} \quad (11.240)$$

The angle δ can be expressed in terms of the numerical aperture of the fiber using Snell's law at the entrance:

$$\text{NA} = n_c \sin \delta \quad (11.241)$$

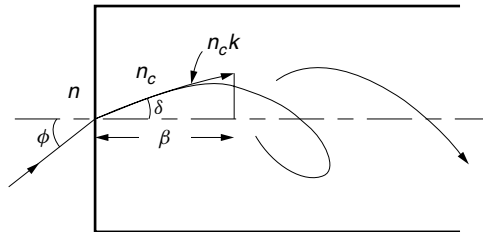


Figure 11.41 Relationship between NA and δ .

Finally, using Eqs. (11.240) and (11.241) for a small value of δ , Eq. (11.239) can be approximated as

$$\Delta\tau = \frac{(\text{NA})^4}{8cn_c^3} \quad (11.242)$$

where $N_c \doteq n_c$ was assumed.

Let us now compare the information-carrying capacity of a multimode step-index fiber with that of a multimode graded-index fiber. Comparison between Eqs. (11.7) and (11.242) leads to the conclusion that the graded-index fiber capacity is $4n_c^3/n_1(\text{NA})^2$ times greater, which is normally a few hundred times that of a step-index fiber.

11.9.5 Mode Patterns in a Graded-Index Fiber

A few words about approximate field distributions obtained from ray theory will be mentioned. As the relevant dimensions decrease, the accuracy of ray theory deteriorates. Mode patterns calculated from ray theory cannot be expected to be accurate when the dimensions are of the order of a wavelength. We will calculate the fields using ray theory and compare these with our earlier results. Thus far only the positive signs of Eqs. (11.184) and (11.185) have been retained and the negative signs were discarded. The negative signs generate the skew rays encircling in the opposite direction. Including the terms with the negative sign, two oppositely propagating skew rays form a standing-wave pattern that is the mode pattern of the fiber. Equation (11.187) indicates that such standing waves, $u_0(e^{jv\phi} + e^{-jv\phi}) = 2u_0 \cos v\phi$, have $2v$ maxima in every complete turn in circumference.

Next, we will consider the radial direction. From Eq. (11.187)

$$\begin{aligned} u &= u_0 \left[e^{j \int_{r_{\min}}^r \sqrt{(nk)^2 - (v/r)^2 - \beta^2} dr} + e^{-j \int_{r_{\min}}^r \sqrt{(nk)^2 - (v/r)^2 - \beta^2} dr} \right] \\ &= 2u_0 \cos \int_{r_{\min}}^r \sqrt{(nk)^2 - (v/r)^2 - \beta^2} dr \end{aligned}$$

The phase advances with r . Eq. (11.219) indicates that by the time r reaches r_{\max} from r_{\min} , the phase advances $\mu\pi$ radians. During this phase advance the cosine function goes through μ extrema.

In conclusion, the (v, μ) mode generates $2v$ extrema in the circumference and μ extrema in the radial direction. Examples of the mode patterns are shown in Fig. 11.40.

Thus, the field expressions of the graded-index fiber obtained by ray theory match those of the $\text{LP}_{v\mu}$ modes of the step-index fiber, except that the r dependence of the $\text{LP}_{v\mu}$ mode is a Bessel function, while the fields obtained by ray theory are sinusoidal functions. The results of the two theories agree reasonably well.

Example 11.7 Answer the following questions for a Selfoc fiber whose physical parameters are as follows:

Refractive index at the center of the fiber, $n_c = 1.54$

Wavelength, $\lambda = 1.3 \mu\text{m}$

Effective radius (i.e., the largest possible major axis of the light path), $r_{\text{eff}} = 10 \mu\text{m}$

Numerical aperture, $\text{NA} = 0.2$

- (a) What is the acceptance angle of the fiber?
- (b) What is the refractive index gradient constant α ?
- (c) What is the largest value of the principal mode number N ?
- (d) Approximately how many modes are excited?
- (e) How many of the modes are meridional rays?

Solution

- (a) From Eqs. (11.3) and (11.4),

$$\phi_c = 11.5^\circ$$

- (b) The major axis A of the ellipse is, from Eq. (11.214),

$$A = \sqrt{p + q}$$

With Eqs. (11.202) and (11.203), A has the largest when $\nu = 0$ and is $\sqrt{2p}$.

$$\begin{aligned} r_{\text{eff}} &= \sqrt{2p} = \frac{\sqrt{(n_c k)^2 - \beta^2}}{n_c k \alpha} \\ &= \frac{\sqrt{1 - (\beta/n_c k)^2}}{\alpha} \doteq \frac{\delta}{\alpha} \end{aligned}$$

where Eq. (11.240) was used. From the above equation and Eq. (11.241), α is

$$\alpha = \frac{\text{NA}}{n_c r_{\text{eff}}} = 0.013 \mu\text{m}^{-1} \quad (11.243)$$

The result is interpreted as follows. A larger α means a larger focusing power of the incident light to the fiber, and hence a larger NA.

- (c) From Eqs. (11.229) and (11.230), N_{max} is

$$\begin{aligned} 1 &= \frac{2\alpha N_{\text{max}}}{n_c k} \\ N_{\text{max}} &= \frac{n_c k}{2\alpha} = \frac{1.54 \times 2\pi/1.3}{2 \times 0.013} = 286 \end{aligned}$$

- (d) Note that

$$\nu + 2\mu \leq 286$$

$$\nu = 286 - 2\mu$$

which is the equation of a line in (ν, μ) coordinates, intercepting the axes at $\nu = 286$ and $\mu = 143$, as shown in Fig. 11.42. Each point inside the triangular area is a mode, so that the total number m of modes is

$$m = \frac{1}{2} \times 286 \times 143 = 20,449$$

including degenerate modes.

- (e) Meridional rays have $\nu = 0$ and there are 143 such modes. □

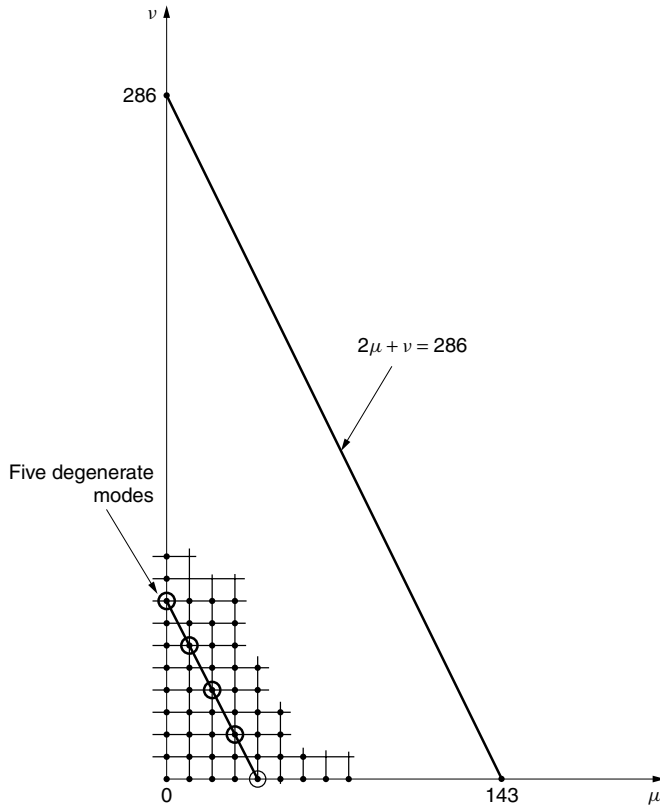


Figure 11.42 Total number of modes in a Selfoc fiber.

Example 11.8 Figure 11.43 shows an excerpt from a Corning Glass Works specification sheet for their 50/125 μm LDFTM CSB4 multimode optical fiber. Verify (a) the numerical aperture and (b) the bandwidth at $\lambda = 1300$ nm listed in the optical specifications of Fig. 11.43 using the parameters found in the characterization data. Assume a quadratic distribution of the index of refraction.

Solution

(a) In order to use Eq. (11.243), the value of α has to be found first. From the given refractive index profile

$$\Delta_{\max} = 0.0125$$

The index of refraction n_c at the axis as specified is

$$n_c = 1.4598$$

Hence, from Δ_{\max} , n_2 at the cladding is

$$n_2 = 1.4416$$

2.0 Optical Specifications

Bandwidth:

Standard Bandwidth Cells:

Bandwidth Cells [MHz-km]	
850 nm	1300 nm
$\geq 400 - \geq 1000$	$\geq 400 - \geq 1500$

Special bandwidth cells available upon request.

Core Diameter $50.0 \pm 3.0 \mu\text{m}$

Numerical Aperture: 0.200 ± 0.015

6.0 Characterization Data

Characterized parameters are typical values.

Core Material Index of Refraction (Peak): 1.4655 at 850 nm
1.4598 at 1300 nm

Refractive Index Profile (typical fiber):

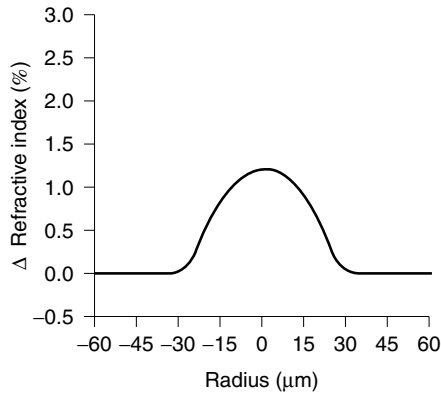


Figure 11.43 Excerpt from Corning's specification sheet.

If a quadratic distribution is assumed, then

$$n^2 = n_c^2(1 - \alpha^2 r^2)$$

$$1 - \left(\frac{n}{n_c}\right)^2 = \alpha^2 r^2$$

The index of refraction in the graph reaches n_2 at $r = 27 \mu\text{m}$.

$$\alpha = \frac{\sqrt{1 - 0.9752}}{27} = 0.00583 \mu\text{m}^{-1}$$

From the previous example, Eq. (11.243) gives

$$\text{NA} = n_c r_{\text{eff}} \alpha$$

assuming $r_{\text{eff}} = 25 \mu\text{m}$ from the specification for the core diameter, the NA is calculated as

$$\begin{aligned} \text{NA} &= 1.4598 \times 25 \times 0.00583 \\ &= 0.213 \end{aligned}$$

which matches with the value $\text{NA} = 0.200 \pm 0.015$ in the specification sheet.

(b) Next, the maximum bandwidth will be found. From Eq. (11.242),

$$\begin{aligned} \Delta\tau &= \frac{(\text{NA})^4}{8cn_c^3} = \frac{(0.21)^4}{(8)(3 \times 10^5)(1.4598)^3} \\ &= 260 \text{ ps/km} \end{aligned}$$

As explained in more detail in Section 16.6.5, in the field of digital communication, the most often used criterion for the required rise time ΔT (time required for the level to rise from 10% to 90% of the steady-state signal level) is that the rise time be kept less than 70% of the bit period when NRZ coding is used and 35% when RZ coding is used, as shown in Fig. 11.44.

Using the 70% criterion, the rise time ΔT should satisfy $\Delta T \leq 0.7T$, where T is the pulsewidth. If the rise time is assumed to be equal to the pulse spread $\Delta\tau$, then the bit rate $1/T$ using the 70% criterion is

$$R = \frac{1}{\Delta\tau} \times 0.7 = 2.695 \times 10^9 \text{ (bits/s)} \cdot \text{km}$$

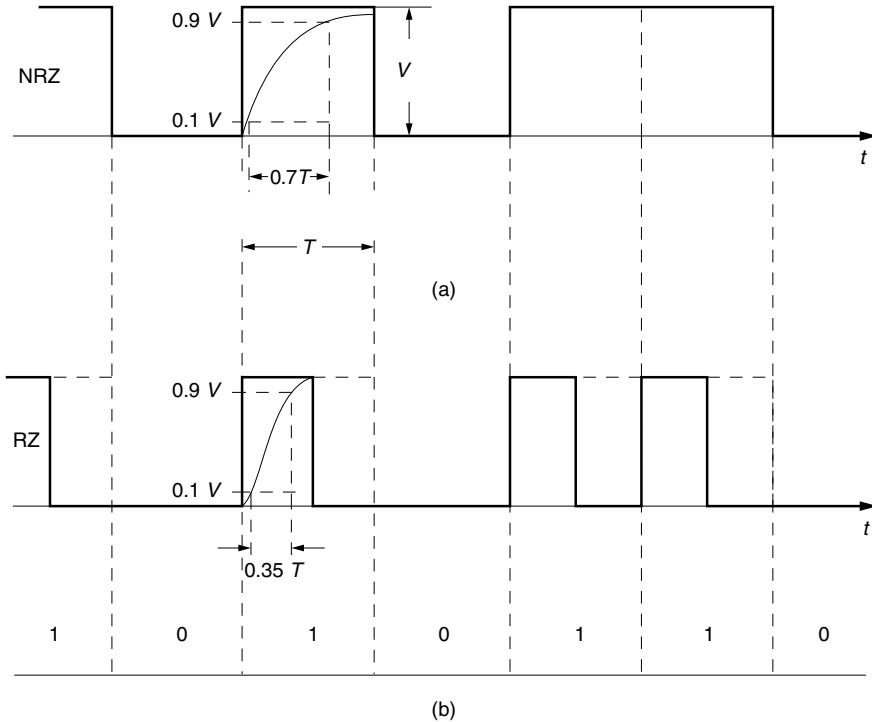


Figure 11.44 Time space T needed for pulses with finite rise time ΔT for (a) NRZ and (b) RZ coding.

Since the specification sheet is given in terms of frequency, a pulsewidth in the time domain has to be converted into the frequency domain. As explained in Section 16.6.5, the pulsetrain at the bit rate R needs a frequency bandwidth B given by

$$B = mR$$

$$m = 0.5 \quad \text{for NRZ code}$$

and

$$B = 1.348 \text{ GHz}$$

This value agrees well with the specification sheet. □

11.10 FABRICATION OF OPTICAL FIBERS

Fabrication of optical fibers may broadly be categorized into one-stage processes and two-stage processes. In the one-stage process, the fiber is drawn directly from the liquefied materials, and in the two-stage process, a highly purified preform rod is fabricated at the first stage, and then the fiber is drawn out of the preform in the second stage. Although the one-stage process has such advantages as simplicity of fabrication, unlimited fiber length, and a faster rate of fabrication, it is the two-stage process that can produce fibers with lower loss and better uniformity.

11.10.1 Fabrication of a Fiber by the One-Stage Process

Figure 11.45 shows a diagram of the double-crucible method, which belongs to the category of one-stage processes. There are inner and outer crucibles with a nozzle at the bottom. The inner crucible is filled with the material of higher index of refraction and the outer with that of the lower index of refraction. The fiber is drawn from the bottom. The nozzle of the inner crucible for the core is much smaller than that of the cladding. The molten core glass is exposed to the molten cladding glass. Diffusion of the molten glasses takes place, and the profile of the graded-index fiber is established. The drawing and the temperature of the heater control the fiber dimension as well as the refractive index profile formed by diffusion.

The diameter of the drawn fiber is monitored, and the monitor output controls the speed of the capstan that pulls the fiber. Immediately after drawing, the fiber is coated with a UV-curable resin, which is then cured inside a confocal reflector UV light cavity, and the coated fiber is reeled onto a bobbin.

An advantage of the double-crucible method is that the fiber can be drawn continuously. A disadvantage is that the double-crucible method can only be used with a lower melting point glass such as multicomponent glass, which has a higher loss than pure silica glass. Another disadvantage associated with the double-crucible method is that product uniformity is more difficult to control.

With a small variation, a plastic-clad silica (PCS) fiber can be fabricated. As the core of the fiber is drawn from the crucible of molten glass, a plastic material that can act as the cladding layer of the fiber is coated onto the glass. Even though fabrication is simpler and costs less, the transmission loss of the resulting fiber is high so that the PCS fiber is only useful for short-distance transmission. Short-distance transmission means a larger dispersion can be tolerated, and the NA values of the PCS fiber are

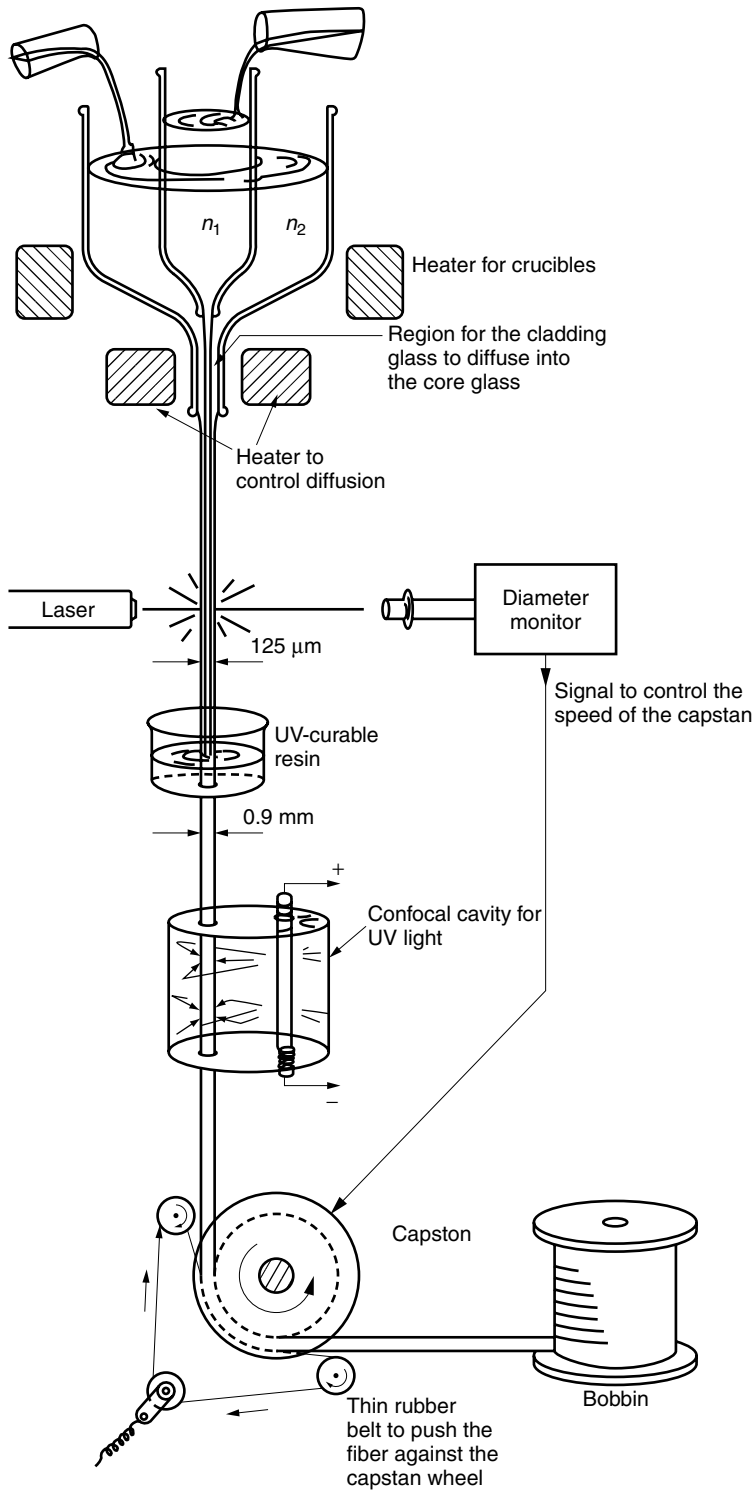


Figure 11.45 Fabrication of optical fiber by the double-crucible method.

usually made larger ($NA = 0.35$) than that of the glass fiber ($NA = 0.2$) for easier coupling.

11.10.2 Fabrication of a Fiber by the Two-Stage Process

Fabrication of a fiber by the two-stage process consists of fabricating a preform and then drawing a fiber from the preform. Since the preform can be made out of highly purified silica with a precise refractive index profile, a fiber with low loss and low dispersion can be fabricated. A disadvantage of this fabrication process, however, is the finiteness of the fiber length and the necessity of the additional stage in the process.

11.10.2.1 Fabrication of Preforms

A silica-based core with a purity better than 0.1 ppb (parts per billion 10^{-9}) can be achieved. In order to appreciate this high degree of purity, let us make an analogy with the world's population. In a population of approximately 5 billion people, 0.1 ppb corresponds to $\frac{1}{2}$ a person.

It was the chemical vapor deposition (CVD) method that made it possible to attain such a high degree of purity. The CVD method was originally developed in semiconductor industries. It is an extremely effective method. The method uses the difference in the vapor pressures of the liquid metal halides of the material and those of the impurities. Figure 11.46 shows the vapor pressures of various metal halides as a function of temperature. Metal halides such as BCl_3 , SiCl_4 , and POCl_3 are used for the material, and VCl_4 and FeCl_3 are the impurities to be removed. Halides whose vapor pressures are above the container pressure will evaporate into the container while those

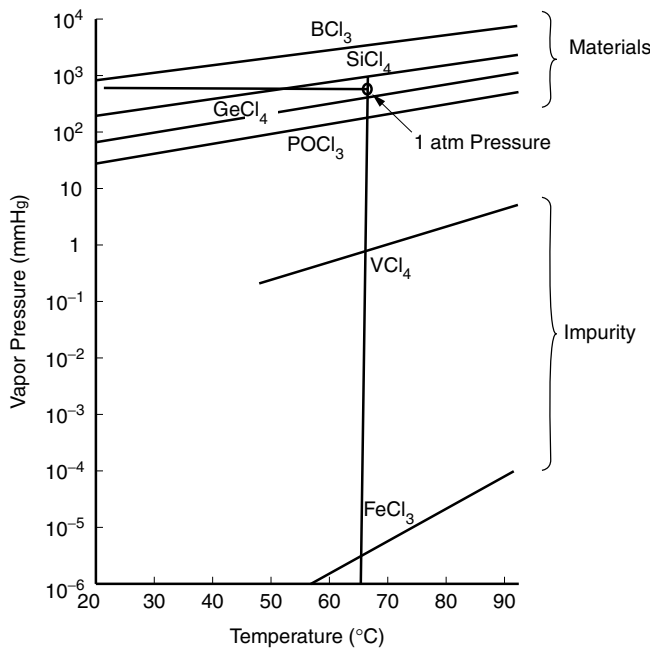


Figure 11.46 Relation of vapor pressures for metal halide additives and potential impurities. (After P. C. Schultz [48].)

below the container pressure will stay as liquid. For instance, if O_2 is bubbled into the $SiCl_4$ container at $65^\circ C$ with 1 atmosphere pressure, $SiCl_4$ bubbles out as vapor but impurities such as VCl_4 or $FeCl_3$ stay in the liquid. Thus, $SiCl_4$ gas that is free from impurity is obtained. As seen in Fig. 11.46, the difference between the vapor pressures of the materials and that of the impurities is so large that purification is achievable without the need for tight temperature control.

The next step is to fabricate the preform out of these material gases. There are a number of approaches for doing this, which can be classified into three major groups depending on the way the deposit of the material is made.

In the first group, layers of material are deposited inside a silica tube, and depending on the method of heating the tube, they are further subdivided into the following three methods.

1. Modified chemical vapor deposition (MCVD) method.
2. Plasma chemical vapor deposition (PCVD) method.
3. Plasma-enhanced modified chemical vapor deposition (PMCVD) method.

The outside vapor deposition (OVD) method belongs to the second group, which deposits the layers of material on the outside of a mandrel. The mandrel is removed after the formation of the layers.

The third group is the vapor-phase axial deposition (VAD) method, which deposits the layer in the direction of the axis of the preform and therefore does not have length limitations.

Let us start with the MCVD method. The MCVD arrangement is shown in Fig. 11.47. The material gases are prepared by the CVD method. Material halides in liquid form, such as $SiCl_4$, $GeCl_4$, and $POCl_3$, are stored in separate reservoirs. Purified

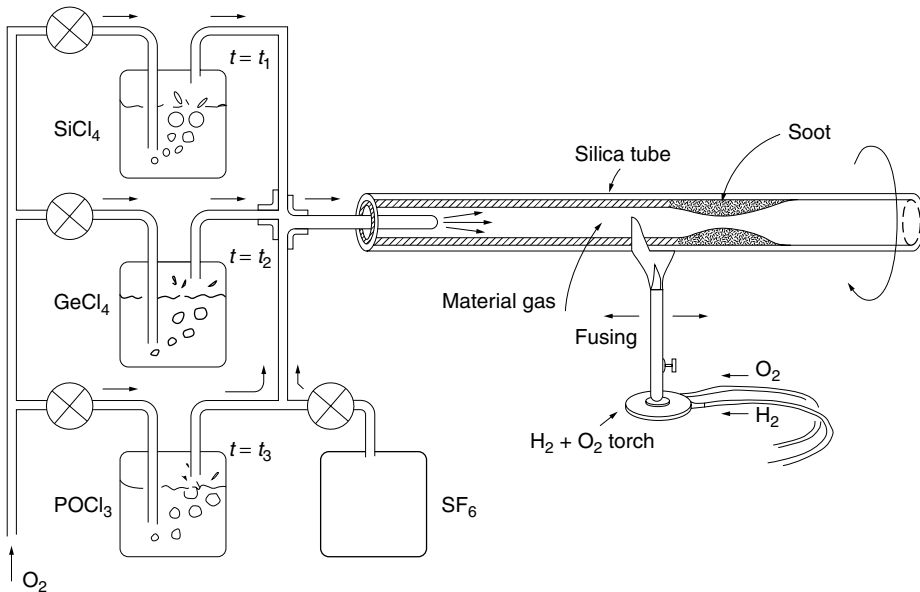
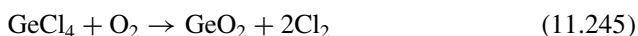
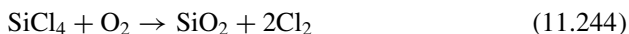


Figure 11.47 Modified chemical vapor deposition (MCVD) method.

oxygen gas is bubbled into these reservoirs at a prescribed pressure and temperature so that only the pure material gas can bubble out. The bubbled out material gases are mixed in prescribed proportions and led into the inside of a silica tube. The mixture proportions are manipulated by a computer-controlled mass flow manifold.

A chemical reaction takes place in vapor form inside the silica tube with the aid of an oxyhydrogen flame outside the tube. The metal halide vapors are oxidized, and small glass particles, which look like chalk powder, are deposited on the inside wall of the silica tube. The small glass particles are called “soot” and are formed by the following chemical reactions:



Soot deposited ahead of the flame is fused to the glass wall as the flame passes. Both dopants GeO_2 and P_2O_5 raise the index of refraction of the glass, while F lowers the index of refraction. Core and cladding layers are formed by programmed control of the mass flow manifolds. The maximum achievable increase or decrease Δ in the index of refraction is limited because, with excessive amounts of dopant, the fiber cracks due to the difference in the heat expansion coefficient between the dopants and the silica glass. The maximum values of Δ that can be tolerated before cracking becomes a problem are $\Delta = 3.5\%$ for GeO_2 -doped SiO_2 , $\Delta = 1.2\%$ for P_2O_5 -doped SiO_2 , and $\Delta = 0.7\%$ for F-doped SiO_2 [49].

The preform of a graded-index fiber is completed after about 30 repetitions of the process of fusing the layers. The tube with the completed layer formation is then collapsed into a rod by heating.

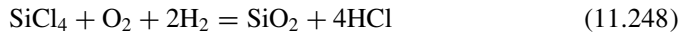
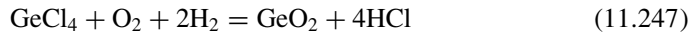
Next, let us take a look at the PCVD method. The PCVD method uses the plasma generated in a microwave cavity instead of the oxyhydrogen flame as a source of heating. The cavity is cylindrical in shape and is resonated at a few gigahertz. Two holes are made on the sides of the cavity so that it can slide coaxially with the silica tube. Because of the high temperature of the plasma generated inside the cavity, the material gas becomes direct-deposited new glass on the tube wall, instead of by way of soot. Advantages of the PCVD method over the MCVD method are that, in the PCVD method, the deposition efficiency and speed are higher, there is greater control over profiles because the temperature can be more precisely controlled, and the tube need not be rotated. The disadvantage of the PCVD method is that the entire apparatus has to be under vacuum so that plasma can be generated inside the cavity, and the apparatus of the PCVD is more complex. Because of the high temperature of the plasma, the silica has to be preheated and this also creates additional complexity.

Next, the PMCVD method will be explained. PMCVD is quite similar to PCVD except that it uses an induction heater operated at a few megahertz. The advantage of the induction heater over the microwave cavity is that it does not require a vacuum. The temperatures obtainable with the induction heater are not high enough to fuse the glass directly to the tube wall, so that the process has to be assisted by an additional oxyhydrogen flame. The advantage of the PMCVD method over the original MCVD method is related to the advantage of heating from the inside (induction heating) over heating from the outside (flame). PMCVD has a much faster deposition rate, and larger

preforms can be made. The disadvantage of the PMCVD method is that the profile is more difficult to control than the MCVD and PCVD methods.

Next, the OVD method, which deposits the soot on a rotating carbon or ceramic rod, is explained.

Figure 11.48 shows a diagram of the OVD method. The material gases are prepared again by the CVD method. Material gases such as SiCl_4 , GeCl_4 , and POCl_3 are bubbled out with purified O_2 . The material gases are brought into the torch region, fueled by H_2 and O_2 . The soot is formulated by the following chemical reactions:



Note the difference from the case of MCVD where there is no chance that the material gases meet hydrogen. After the starting rod is pulled out, the soot is fused into a preform in a furnace. Cl_2 and helium gas are introduced into the furnace. Cl_2 removes OH ion impurities, and helium prevents bubble formation in the glass.

Compared to the MCVD method, it is possible to make larger preforms with the OVD method, which means longer continuous lengths of fiber can be drawn. The deposition speed is also faster with OVD than MCVD because of the direct interaction of material gases and flame gases that takes place in OVD. However, this direct interaction of H_2 and O_2 gases with the material gases means the likelihood of OH ion contamination in the glass is greater with OVD than MCVD, increasing the fiber loss. In OVD there is also the added step of removing the starting rod, which may produce irregularities in the refractive index profile of the core.

The last method of preform fabrication to be described is the VAD method. A diagram of this method is shown in Fig. 11.49a, and a photograph of the flame is

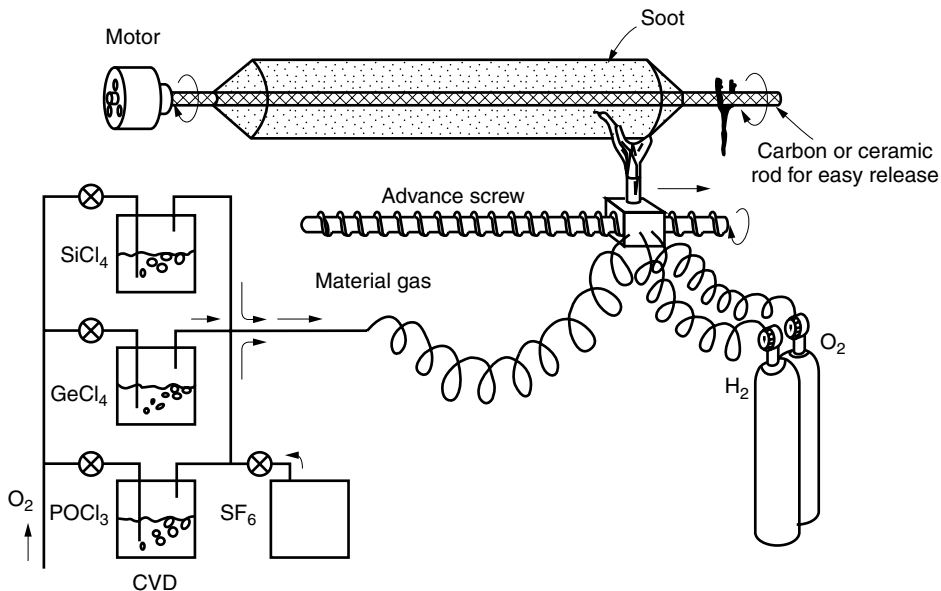


Figure 11.48 Outside vapor deposition (OVD) method.

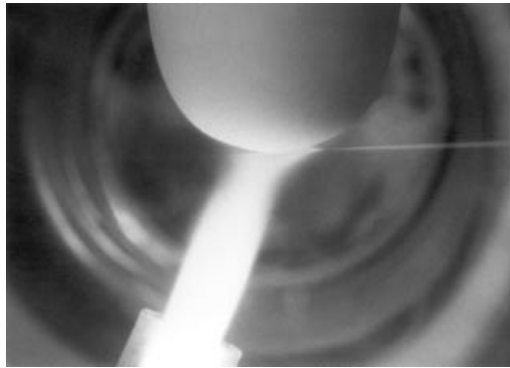
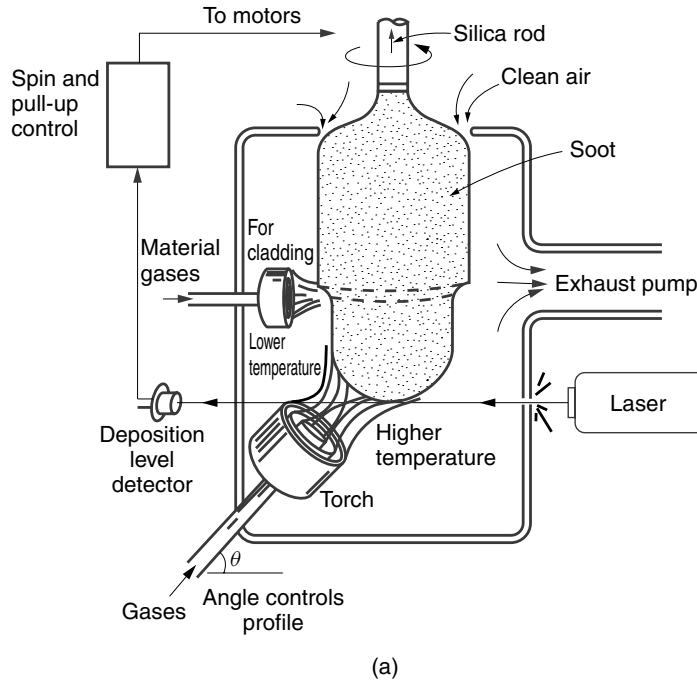


Figure 11.49 Vapor-phase axial deposition (VAD) method. (a) Apparatus. (b) Deposit of the soot. A horizontal laser light monitors the position of the bottom of the soot. (Courtesy of H. Murata).

shown in Fig. 11.49b. The soot is deposited by the interaction of the flame with the material gases. The rod is rotated on its own axis and is slowly pulled upward as it grows. Theoretically speaking, there is no limit on the length of the soot rod, and the length of the rod can be arbitrarily long.

The torch is structured in multicoaxial layers, and the arrangement of the material and fuel gases is critical.

The flame is angled with respect to the rod so that a temperature differential is established between the center and the circumference of the rod. The temperature at

the center of the rod is highest because this spot is exposed to the flame throughout the revolution of the rod while a spot on the circumference is exposed to the flame only during a fraction of the revolution. The amount of deposition of $\text{GeO}_2\text{:SiO}_2$ soot is largest at the highest temperature. The desired profile of the index of refraction of the graded-index fiber can be achieved by critically adjusting the angle of the torch as well as the proportion of the material gases.

11.10.2.2 Drawing into an Optical Fiber

In the second stage of the process, an optical fiber is drawn from the preform rod. Figure 11.50 shows an apparatus for drawing an optical fiber. The lower end of the

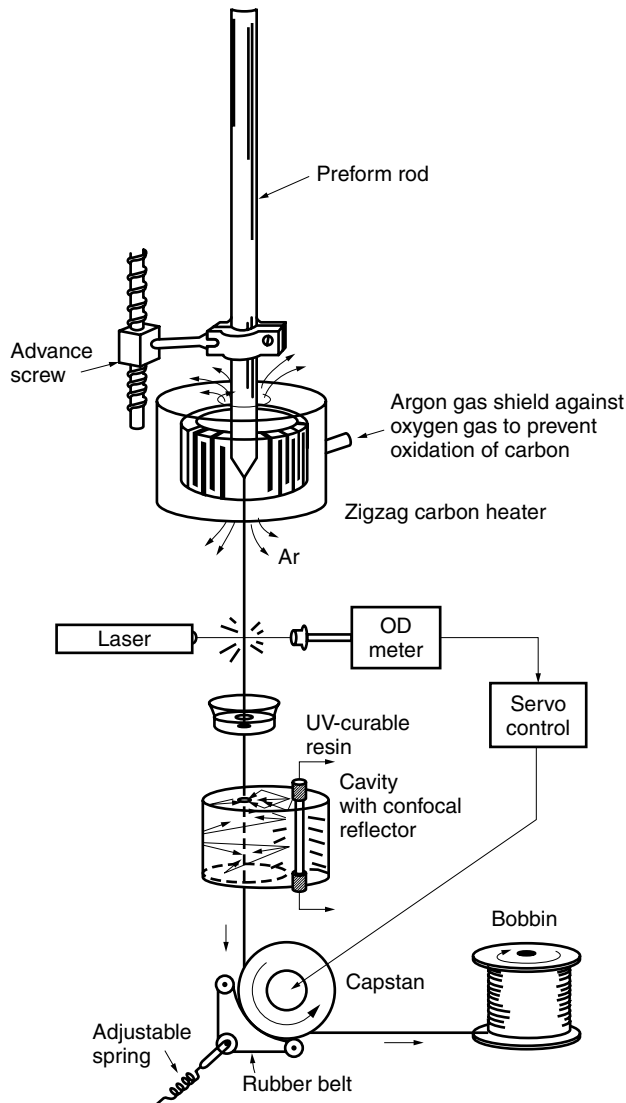


Figure 11.50 Apparatus for drawing a fiber.

preform is heated in a furnace to 2000–2100°C, which is a few hundred degrees above the melting temperature (1900°C) of the fiber. The furnace makes it possible to draw an optical fiber with a specified diameter in one step. The furnace is made out of a fat graphite filament bent like a cage surrounding the preform. Argon gas is blown into the furnace so as to protect the filament from oxidation burnout.

The fiber diameter is controlled by the speed with which the fiber is pulled. The pulling speed is adjustable by the number of revolutions per minute (rpm) of the capstan. The feedback signal of the fiber diameter monitor controls the rpm of the capstan. The fiber is pushed against the wheel of the capstan by a thin rubber belt that also rotates at the same speed as the capstan wheel. The diameter of a drawn fiber is normally 125 μm .

The drawn fiber is immediately jacketed by a UV-curable resin. This reduces the chance of foreign particles attaching themselves to the bare fiber. Foreign particles on the fiber surface become sources of small cracks, weakening the optical fiber.

The resin jacket is cured inside a confocal reflector UV light cavity. The fiber passes along one of the lines of focus of a cylindrical cavity with an elliptical cross section while a bar UV light is positioned along the other line of focus. The outer diameter of the jacketed fiber is normally either 0.25–0.35 mm or 0.8–1.0 mm.

The fiber is then reeled onto a spool either with or without going through the screen test spool. The screen test is performed by bending through a set of small wheels under tension.

The jacketed fiber is then cabled for telecommunication purposes.

11.11 CABLING OF OPTICAL FIBERS

The mechanical specifications of cabling [49,50] are that, under normal conditions of use, the elongation should be less than 0.2% and the bending radius should be no less than 3 cm. That is, the performance of the fiber is guaranteed for these specifications. As a matter of fact, when subjected to extreme tests, one piece of fiber can pick up a 5-kg weight resulting in a 5% elongation, or the fiber can be bent to curvature as small as 2–3 mm radius without breaking. The cabling specifications for the values of elongation or bending radius are far from the physical limits of the fiber.

The general principle of reducing the tension of a fiber inside a cable is stranding and is the same as that of the telephone cord shown in Fig. 11.51. A telephone cord is coiled so that even a reckless child will not rip the cord off the telephone. The difference between a telephone cord and an optical fiber cable is that the optical fiber cable is equipped with a strength member inside the cable to limit the elongation and a sheath outside to prevent damage during installation and operation.

Another important concern with optical fibers is the increase in microbending loss at lower temperatures. The temperature expansion coefficient of glass is of the order of 10^{-7} , while that of most of the jacket materials is of the order of 10^{-4} . As the temperature is lowered, the jacket shrinks one thousand times more than the glass fiber, and the optical fiber is subjected to many small bends that induce the so-called microbending loss. One solution to this problem is to introduce a buffer layer. The buffer-covered fiber has two different kinds of coatings and has minimum microbending loss. The first inner coating is a soft resin coating that acts as a slipping-buffer layer. The second coating is a hard resin coating that protects the fiber from external forces.

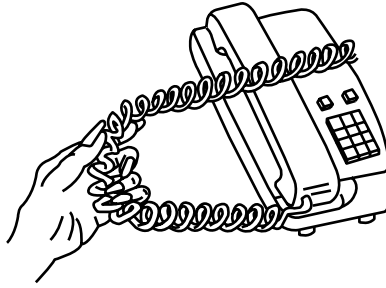


Figure 11.51 Telephone cord and cabling fibers share the same philosophy.

With this configuration, the fiber can slip with respect to the hard coating and the microbending is greatly alleviated.

The complexity of the cable design depends on the application. In laboratory experiments, a single coated fiber may suffice, whereas in a telecommunication link, the overall cable structure may house a number of individual cabled fibers. Let us now describe this hierarchy of cable design, which is broadly classified into the following three categories:

1. Element fibers.
2. Unit fiber cable.
3. Multiunit fiber cable.

The configurations for the element fibers are shown in the top row of Fig. 11.52, while those for the unit fiber cable and the multiunit fiber cable are shown in the middle and bottom rows of Fig. 11.52, respectively. The element fibers will be explained first.

The 0.25-mm-OD monocoated fiber (Fig. 11.52a) is thin with an outer diameter of only 0.25 mm. Even though it has the merit of low production cost, it has such demerits as high microbending loss and difficulty of handling and stranding.

The 0.25-mm-OD buffer-covered fiber (Fig. 11.52b) also has an outer diameter of 0.25 mm. The jacket is composed of two layers, a soft inner layer and a harder outer layer. As mentioned previously, this configuration minimizes the increase in microbending loss at lower temperatures.

The 0.9-mm-OD buffer-covered fiber (Fig. 11.52c) also has soft and hard layers, but the jacket is thicker, giving an outer diameter of 0.9 mm. This fiber has the merit of smaller microbending loss and easier handling compared to its thinner counterpart.

The loose-tube covered fiber (Fig. 11.52d) has a significantly larger buffer layer filled with either jelly or nothing. The fiber used for the inside is buffer-covered 0.25-mm-OD fiber. The microbending characteristics are excellent and no recognizable increase in the microbending is observed even at very low outside temperatures. There is, however, some degree of difficulty in removing the tube at the time of splicing because of the combination of the hard outside tube and the thin fiber inside the tube.

The middle row of Fig. 11.52 shows bundles of fibers at an intermediate stage to the final cable configurations shown in the bottom row. They are explained as follows.

For the unit cable (Fig. 11.52e), six 0.9-mm-OD buffer-covered fibers are stranded around a strength member of a copper-plated steel wire. The stranding pitch is 10 to 40 cm. Stranding provides flexible stretching of the fiber analogous to the telephone

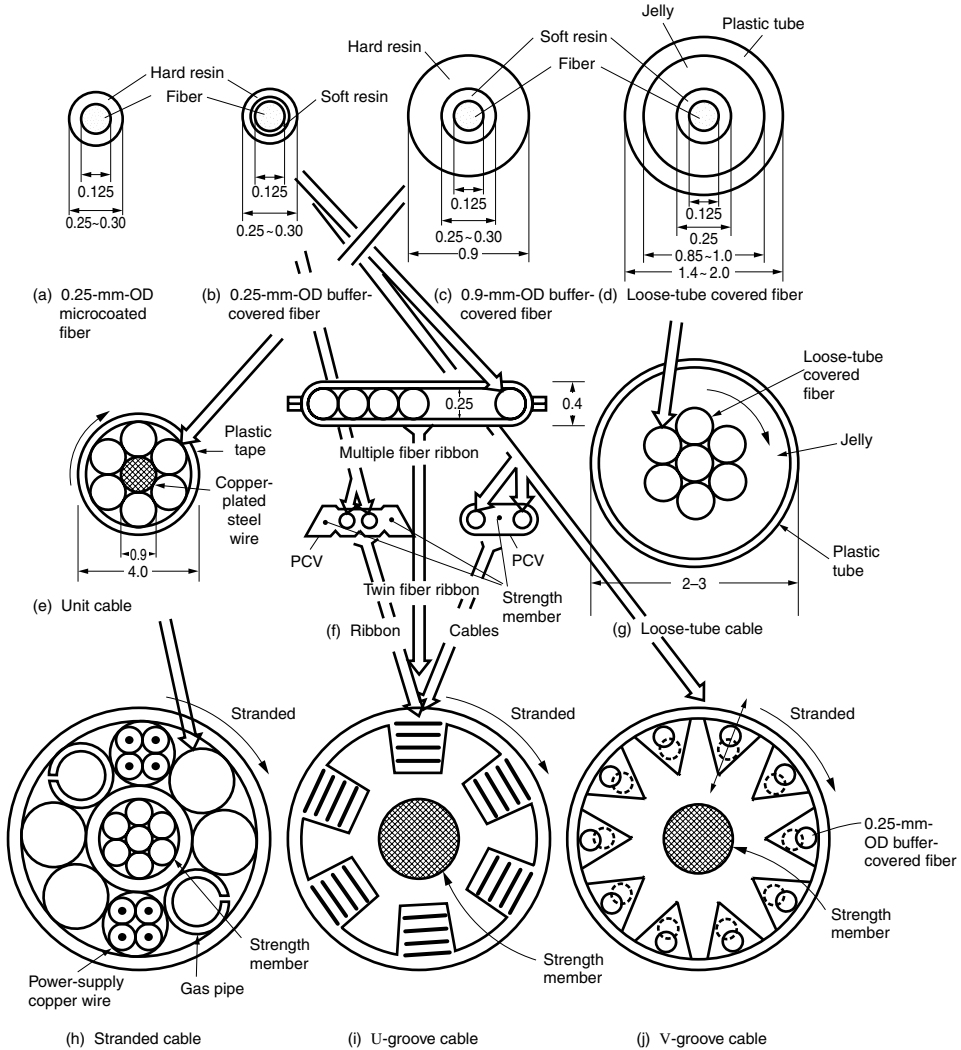


Figure 11.52 Hierarchy of optical fiber cables (dimensions in mm). (After H. Murata [49].)

cord effect mentioned earlier. The stranded fibers are held together by wrapping with plastic tape.

For the ribbon cable (Fig. 11.52f), five to twelve 0.25-mm-OD buffer-covered fibers are arranged in parallel and are sealed by adhesive plastic tape. An advantage of the fiber ribbon design is that it is possible to splice all fibers in one operation by using a mass fusion splicing machine. The twin fiber ribbons are designed for indoor use. The potential for easy speedy splicing in the field of a large number of fibers is the greatest merit of the ribbon fiber.

For the loose-tube cable (Fig. 11.52g), seven 0.25-mm-OD buffer-covered fibers are stranded into one bundle and put into a 2–3-mm-diameter plastic tube. The tube is filled with jelly and the fiber bundle moves freely inside the tube, escaping from external stresses.

Finally, the cabling structures shown in the bottom row of Fig. 11.52 will be explained.

For the stranded cable (Fig. 11.52h), several unit cables are stranded into a cable with a stranding pitch more or less the same as that of the unit cable (10–40 cm). Figure 11.50h is an example of a 24 optical fiber cable. The cable consists of four 6 fiber unit cables, two 4 copper conductor cables for the electrical power supply to the repeater stations, and a stranded copper-plated steel wire as a strength member. Stranding of the steel wire makes the cable more flexible. The last two pipes are gas pipes for keeping moisture off the inside of the cable.

For the U-groove cable (Fig. 11.52i), rectangular grooves are helically made on a polyethylene rod. Ribbon fibers are stacked inside the grooves. A special feature of this cable is its capacity for accommodating a large number of fibers in one cable. The cable shown in the figure contains twenty-four 5 ribbon fibers, and the total number of fibers is 120.

For the V-groove fiber (Fig. 11.52j), the grooves are helically made on a polyethylene rod. Each V-groove can accommodate either a single fiber or a multiple number of fibers. A strength member wire is placed in the center of the cable. The grooved rod not only makes compartments for fibers but also protects the fibers from external forces. Fibers are first put into the groove and then a jelly coating is applied.

Since the rod is helically grooved, the fibers in the grooves behave as if they are stranded. As the cable is stretched, fibers move toward the center of the cable, as indicated by the dotted lines in the figure.

The V-grooved cable can be treated as a unit V-groove cable, and a multiple number of such cables can be stranded into an even bigger size cable, thus accommodating a large number of fibers.

11.12 JOINING FIBERS

Usually, reels of optical fiber cables have to be joined in order to make a cable long enough for a communication system. Basically, there are two kinds of fiber joints. One is a permanent joint, and the other is a demountable joint. The permanent type is not intended to disconnect once installed, and an example is the installation of trunk lines connecting reels of cables. Fibers are spliced together. The demountable type of joint is intended to disconnect occasionally, and an example is the connection to the terminal equipment. Without exception, permanent joints are made by splicing fibers together, as this ensures long-life reliability. Connectors are generally used for nonpermanent joints.

11.12.1 Splicing Fibers

The most common method of splicing two fibers [51] is with an electric arc because it can provide high temperature with cleanliness, accuracy, and reproducibility. A mass fusion splicing machine whose mechanism is illustrated in Fig. 11.53 can splice five fibers in a ribbon automatically with minimal human intervention. Figure 11.53a is a step-by-step illustration of mass fusion splicing, and Fig. 11.53b illustrates the layout of the automated machine. The numbers in Fig. 11.53a indicate the steps in the following explanation.

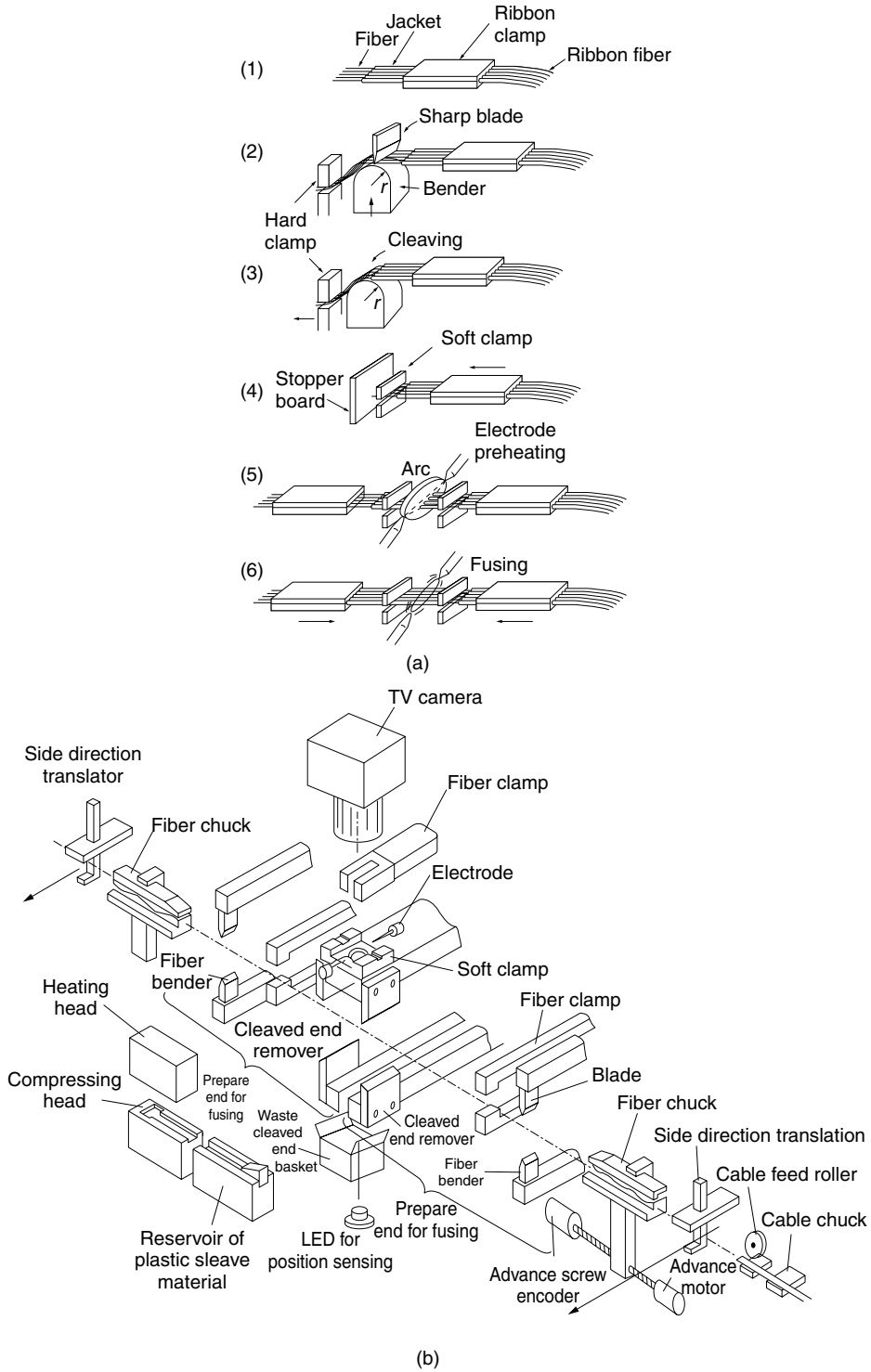


Figure 11.53 (a) Steps for mass fusion splicing. (b) Mass fusion splicing machine for five fiber ribbon. (After M. Matsumoto et al. [51].)

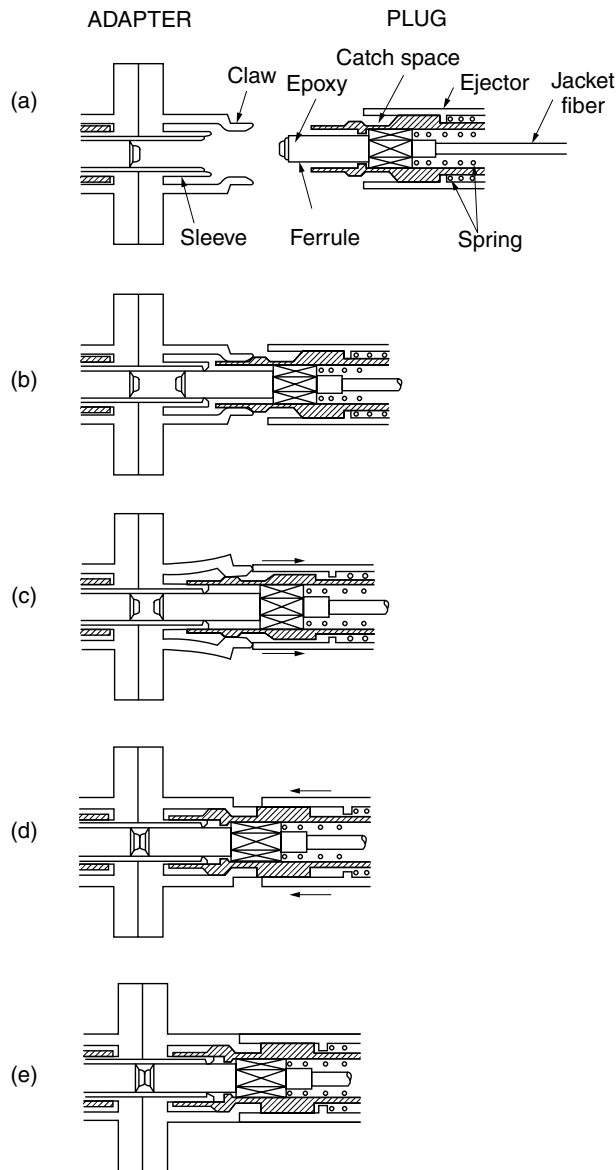


Figure 11.54 Cross section of single port optical fiber connector and steps for making the connection. (After T. Kakii et al. [53].)

(1) The ribbon fiber is first held by a fiber chuck and is cut to a predetermined length, and then its jacket is removed by a jacket stripper to expose an array of fibers. The ends of the fibers are clamped in preparation for cleaving. Cleaving action consists of scoring, bending, and breaking the fibers. Cleaving produces clean, smooth fiber ends, and the cleaved surfaces are reasonably perpendicular to the fiber axis. (2) The fibers are first individually scored by either a diamond or a high-speed steel blade. (3) The scored fibers are then pushed upward by a semicylindrical bed so that the fibers are

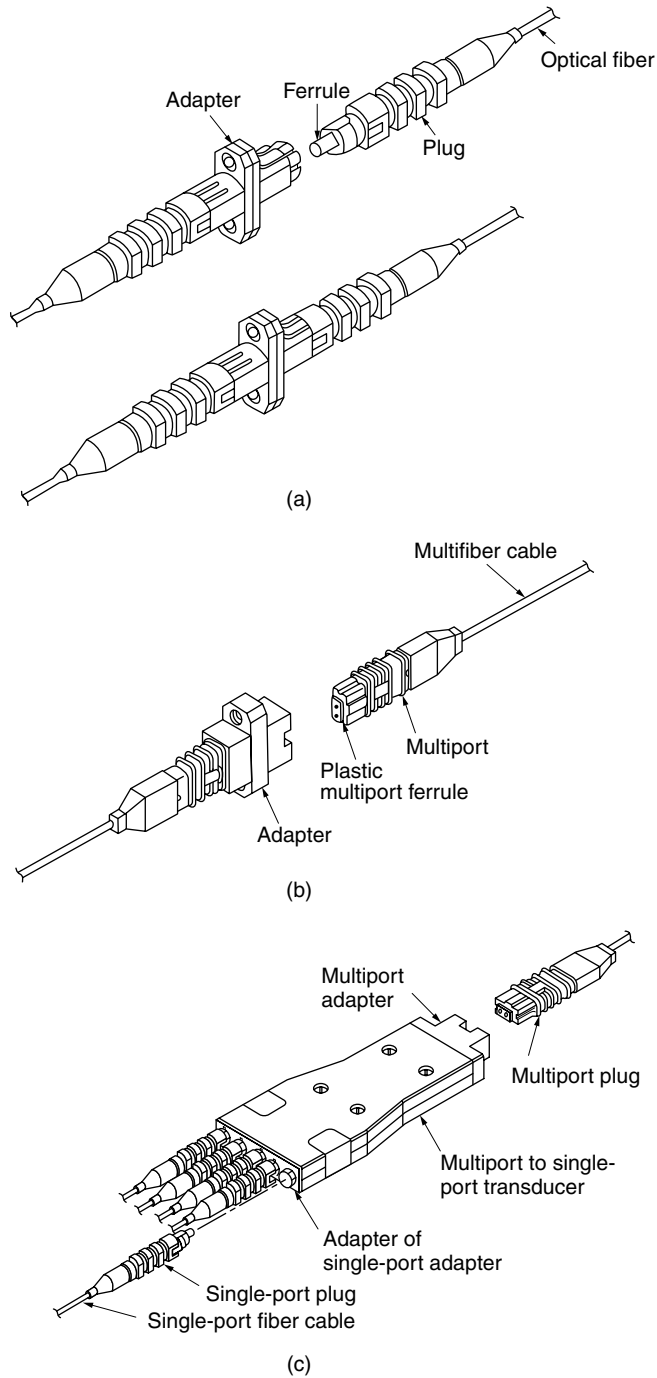


Figure 11.55 Structure of connectors of various types. (a) Single-port optical fiber connector. (b) Multiport optical fiber connector. (c) Multiport to single-port adapter (After T. Kakii et al. [53].)

stretched and bent in an arc, then further pulled, and broken off to complete cleaving. A monitoring TV image not only examines the cleaved surfaces but also aligns the left and right cores. (4) Theunjacketed section of the fibers are held by soft clamps, and are pushed against the stopping plate that appears from the bottom, in order to eliminate any unevenness of the lengths of the cleaved fibers.

After the stopping plate is withdrawn to the bottom, (5) the ends of the fibers are preheated by an electric arc. After preheating the ends, the ribbon fibers are brought together until the ends of the fibers touch; then (6) the fibers are fused together by the electric arc. After the fused fibers are proof-tested by pulling apart with a predetermined tension, (7) the spliced section is reinforced by a bonding agent and the entire splicing process is completed.

Factors that influence the splicing loss are (a) the transversal offset between the two fibers being spliced, (b) the angular tilt of the two fibers, (c) the differences in the core diameters, and (d) the differences in the refractive index profiles of the index of refraction. In order to suppress the splicing loss of a single-mode fiber to less than 0.1 dB, the offset distance should be less than $0.5\text{ }\mu\text{m}$ and the tilt angle has to be less than 0.5° [52].

11.12.2 Optical Fiber Connector

Fiber connectors [53] are used instead of splices at terminal relay stations, at the locations of home subscribers, for ease of operational inspection, in new installations, and for rerouting of communication lines.

Points to be considered in the design of optical fiber connectors are the following:

1. Connectors must be able to withstand outdoor use and normal handling.
2. They should be extremely reliable and durable.
3. The design should strive to minimize connector loss.
4. For systems requiring large numbers of connectors, it is important to keep the cost of fabricating the connectors low.

The major challenge in designing optical fiber connectors is to design connectors that can be mass-produced despite severe machining tolerances.

Figure 11.54a shows the cross section of the connector, and the rest of the diagrams illustrate how the spring action interlocks the two ferrules to the center adapter, maintaining the required precision in offset as well as tilt angle between the two ferrules.

Figure 11.55a shows how the single-port fiber connector looks when the connection is completed. Figure 11.55b shows the mating of a multiport connector, in which a multiport plug is inserted into a multiport adapter. Figure 11.55c shows a transducer that converts a multiport connector into separate single-port connectors. Such a transducer is useful for dropping individual subscriber lines from a ribbon fiber cable.

PROBLEMS

- 11.1** A laser beam with diameter $2a = 0.8\text{ mm}$ is to be focused onto the end of an optical fiber using a convex lens (Fig. P11.1). The diameter of the core is $9.5\text{ }\mu\text{m}$.

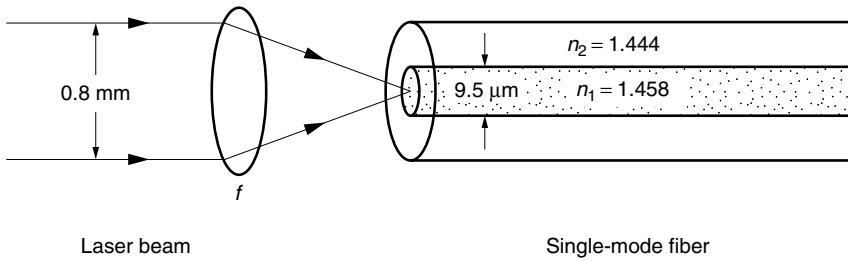


Figure P11.1 Selection of the focal length of a focusing lens.

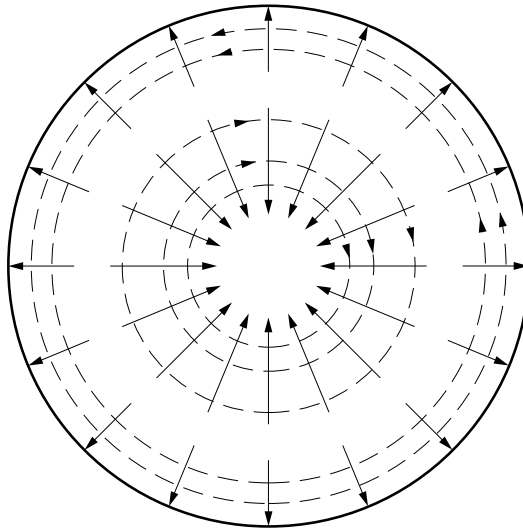


Figure P11.3 A pattern in a step-index fiber. Solid line for E field dotted line for H field.

The index of refraction of the core is $n_1 = 1.458$. The index of refraction of the cladding is $n_2 = 1.444$. The wavelength of the light is $\lambda = 1.55 \mu\text{m}$. What is the range of focal lengths of the lens that can be used for this purpose? Include consideration of the diffraction-limited resolution of the focused image.

- 11.2** Find the asymptotes of the characteristic curves of the $HE_{1\mu}$ modes.
- 11.3** What is the designation of the mode shown in Fig. P11.3?
- 11.4** (a) Draw a rough graph of the characteristic equations of the $HE_{3\mu}$ and $EH_{1\mu}$ modes.
 (b) Verify the cutoff values of V_c indicated in Fig. 11.18 up to the seventh mode using the graphs in the text and the graph drawn for part (a) of this problem.
- 11.5** Graphically construct the field pattern of the LP_{21} mode from those of the hybrid modes.
- 11.6** Find the mode numbers of the $LP_{\nu\mu}$ modes shown in Fig. P11.6. Also find the hybrid modes that are the constituents of these $LP_{\nu\mu}$ modes.

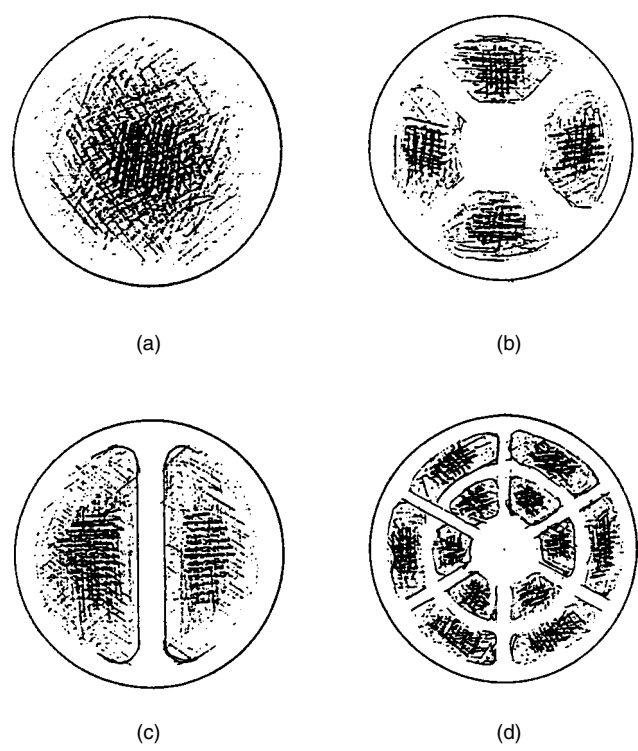


Figure P11.6 Field patterns of $LP_{\nu\mu}$ modes.

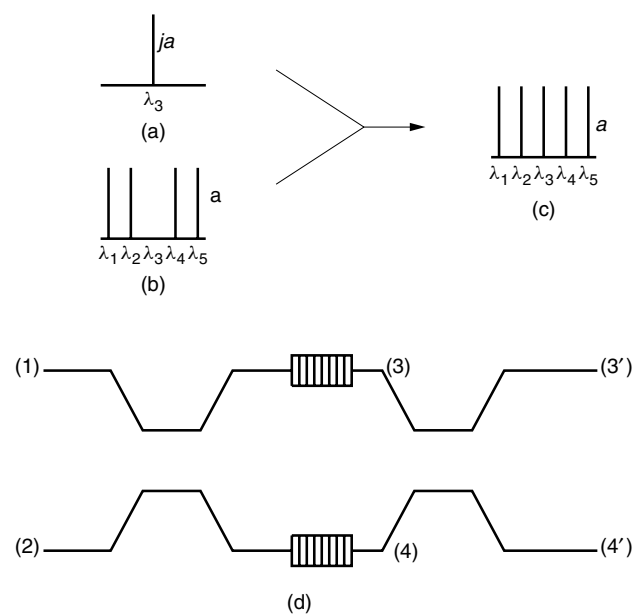


Figure P11.8 Insert the λ_3 channel in (a) into the main stream of the WDM in (b) as shown in (c) using the device shown in (d).

- 11.7** Draw the mode pattern of HE_{22} .
- 11.8** Figure P11.8 shows a multiplexer made out of a Bragg grating fiber and a Mach–Zehnder interferometer. Channel λ_3 shown in Fig. P11.8a has to be multiplexed with the rest of the WDM stream shown in Fig. P11.8b to form the filled WDM stream in Fig. P11.8c. To which ports of the device shown in Fig. P11.8d should the λ_3 signal and the rest of the WDM stream be applied?

REFERENCES

1. C. K. Kao and G. A. Hockham, "Dielectric-fiber surface waveguides for optical frequencies," *Proc. IEE (London)* **113**(7), 1151–1158 (1966).
2. F. J. Denniston and P. K. Runge, "The glass necklace," *IEEE Spectrum*, 24–27 (Oct. 1995).
3. N. S. Bergano and H. Kidorf, "Global undersea cable networks," *Optics and Photonics News*, **12**(3), 32–35 (2001).
4. T. Miya, Y. Terunuma, T. Hosaka, and T. Miyashita, "Ultimate low-loss single-mode fibre at 1.55 μm ," *Electron. Lett.* **15**(4), 106–108 (1979).
5. N. J. Pitt, A. Marshall, J. Irven, and S. Day, "Long term interactions of hydrogen with single-mode fibers," 10th ECOC, pp. 308–309, Sept. 1984.
6. M. Kuwazuru, Y. Namihira, K. Mochizuki, and Y. Iwamoto, "Estimation of long-term transmission loss increase in silica-based optical fibers under hydrogen atmosphere," *J. Lightwave Technol.* **6**(2), 218–225 (1988).
7. G. Tanaka, H. Yokota, H. Kanamori, Y. Ishiguro, Y. Suetsugu, H. Takada, S. Ito, S. Tanaka, Y. Asano, M. Kyoto, M. Watanabe, and K. Yano, "Characteristics of pure silica core single mode optical fiber," *Sumitomo Electric Tech. Rev.* **26**, 43–53 (Jan. 1987).
8. S. Tanaka, and M. Honjo, "Long-term reliability of transmission loss in optical fiber cables," *J. Lightwave Technol.* **6**(2), 210–217 (1988).
9. I. Yoshida, M. Watanabe, G. Tanaka, H. Yokota, and H. Kanamori, "Temperature and dose rate dependence of radiation damage," *12th European Conference of Optical Communication (ECOC 12)*, Barcelona, Spain, p. 41, 1986.
10. H. Bueker, F. W. Haesing, F. Pfeiffer, and H.-J. Schmitz, "A fiber optic twin sensor for dose measurements in radiation therapy," *Opt. Rev.* **4**(1A), 130–132 (1997).
11. S. Kobayashi, S. Shibata, N. Shibata, and T. Izawa, "Refractive-index dispersion of doped fused silica," *1977 International Conference on Integrated Optics and Optical Fiber Communication*, Tokyo, B8-3, pp. 309–312, 1977.
12. D. B. Keck, "Fundamentals of optical waveguide fibers," *IEEE Commun. Mag.*, 17–22 (May 1985).
13. M. Sato, T. Ishigure, and Y. Koike, "Thermally stable high-bandwidth graded-index polymer optical fiber," *J. Lightwave Tech.* **18**(7), 952–958 (2000).
14. B. J. Eggleton, P. S. Westbrook, C. A. White, C. Kerbage, R. S. Windeler, and G. L. Burdge, "Cladding-mode-resonances in air-silica microstructure optical fibers," *J. Lightwave Technol.* **18**(8), 1084–1100 (2000).
15. T. M. Monro, D. J. Richardson, N. G. R. Broderick, and P. J. Bennett, "Modeling large air fraction holey optical fibers," *J. Lightwave Technol.* **18**(1), 50–56 (2000).
16. M. J. Steel and R. M. Osgood, Jr., "Polarization and dispersive properties of elliptical-hole photonic crystal fibers," *J. Lightwave Technol.* **19**(4), 495–503 (2001).
17. N. Kishi and E. Yamashita, "Optical broadband phase devices using axially nonsymmetric W-type optical fibers," *J. Lightwave Technol.* **16**(2), 301–306 (1998).

18. L. G. Van Uitert, and S. H. Wemple, "ZnCl₂ glass: a potential ultralow-loss optical fiber material," *Appl. Phys. Lett.* **33**(1), 57–59 (1978).
19. D. Marcuse, *Light Transmission Optics*, 2nd ed. Van Nostrand Reinhold, New York, 1982.
20. D. Gloge, "Weakly guiding fibers," *Appl. Opt.* **10**(10), 2252–2258 (1971).
21. A. Kapoor and G. S. Singh, "Mode classification in cylindrical dielectric waveguides," *J. Lightwave Tech.* **18**(5), 849–852 (2000).
22. K. O. Hill, B. Malo, D. C. Johnson, and F. Bilodeau, "A novel low-loss inline bimodal fiber tap: wavelength selective properties," *IEEE Photonics Technol. Lett.* **2**(7), 484–486 (1990).
23. C. D. Poole, J. M. Wiesenfeld, and D. J. DiGiovanni, "Elliptical-core dual-mode fiber dispersion compensator," *IEEE Photonics Technol. Lett.* **5**(2), 194–197 (1993).
24. K. O. Hill, B. Malo, F. Bilodeau, and D. C. Johnson, "Photosensitivity in optical fibers," *Annu. Rev. Mater. Sci.* **23**, 125–157 (1993).
25. W. W. Morey, G. A. Ball, and G. Meltz, "Photoinduced Bragg gratings in optical fibers," *Opt. Photonics News*, 8–14 (Feb. 1994).
26. L. Dong, J.-L. Archambault, L. Reekie, P. St. Russell, and D. N. Payne, "Single pulse Bragg gratings written during fibre drawing," *Electron. Lett.* **29**(17), 1577–1578 (1993).
27. P. J. Lemaire, A. M. Vengsarkar, W. A. Reed, and D. J. DiGiovanni, "Thermal enhancement of UV photosensitivity in H₂-loaded optical fibers," *OFC'95 Tech. Digest* **8**, 158–159 (1995).
28. F. Bilodeau, B. Malo, J. Albert, D. C. Johnson, K. O. Hill, Y. Hibino, M. Abe, and M. Kawachi, "Photosensitization of optical fiber and silica-on-silicon/silica waveguide," *Opt. Lett.* **18**(12), 953–955 (1993).
29. D. C. Johnson, F. Bilodeau, B. Malo, K. O. Hill, P. G. J. Wigley, and G. I. Stegeman, "Long-length, long-period, rocking filters fabricated from conventional monomode telecommunications optical fiber," *Opt. Lett.* **17**(22), 1635–1637 (1992).
30. B. Malo, D. C. Johnson, F. Bilodeau, J. Albert, and K. O. Hill, "Single-excimer-pulse writing of fiber gratings by use of a zero-order nulled phase mask: grating spectral response and visualization of index perturbations," *Opt. Lett.* **18**(15), 1277–1279 (1993).
31. G. A. Ball and W. W. Morey, "Continuously tunable single-mode erbium fiber laser," *Opt. Lett.* **17**(6), 420–422 (1992).
32. B. Malo, S. Thériault, D. C. Johnson, F. Bilodeau, J. Albert, and K. O. Hill, "Apodised in-fiber Bragg grating reflectors photoimprinted using a phase mask," *Electron. Lett.* **31**(3), 223–224 (1995).
33. F. Bilodeau, D. C. Johnson, S. Thériault, B. Malo, J. Albert, and K. O. Hill, "An all-fiber dense-wavelength-division multiplexer/demultiplexer using photoimprinted Bragg gratings," *IEEE Photonics Technol. Lett.* **7**(4), 388–390 (1995).
34. K. P. Koo and A. D. Kersey, "Noise and cross talk of a 4-element serial fiber laser sensor array," *OFC'96 Techn. Digest* **2**, 266–267 (1996).
35. Y. Rao, D. J. Webb, D. A. Jackson, L. Zhang, and I. Bennion, "In-fiber Bragg-grating temperature sensor system for medical applications," *J. Lightwave Technol.* **15**(5), pp. 779–785 (1997).
36. R. E. Collin, *Foundations for Microwave Engineering*, 2nd ed., McGraw-Hill, New York, 1992.
37. D. Gloge, "Dispersion in weakly guiding fibers," *Applied Optics* **10**(11), 2442–2445 (1971).
38. M. Ogai, Y. Yano, A. Iino, M. Hashimoto, K. Kokura, and K. Matsubara, "Low loss dispersion shifted fiber with fluorine-doped cladding and step like index profile," *OFC'86 Post Dead Line Paper* 4, 19–22 (Feb. 1986).
39. H. Murata, *Optical Fibers Cable*, Ohm-Sha, Tokyo (1987).

40. K. Takiguchi, S. Kawanishi, H. Takara, K. Okamoto, K. Jinguji, and Y. Ohmori, "Higher order dispersion equalizer of dispersion shifted fiber using a lattice-form programmable optical fiber," *Electron. Lett.*, **32**(8), 755–757 (1996).
41. A. E. Willner, "Mining the optical bandwidth," *IEEE Spectrum*, 32–41 (Apr. 1997).
42. R. Kashyap, S. V. Chernikov, P. F. McKee, and J. R. Taylor, "30 ps Chromatic dispersion compensation of 400 fs pulses at 100 Gbit/s in optical fibers using an all fiber photoinduced chirped grating," *Electron. Lett.* **30**(13), 1078–1080 (1994).
43. D. Garthe, R. E. Epworth, W. S. Lee, A. Hadjifotiou, C. P. Chew, T. Bricheno, A. Fielding, H. N. Rourke, S. R. Baker, K. C. Byron, R. S. Baulcomb, S. M. Ohja, and S. Clements, "Adjustable dispersion equalizer for 10 and 20 Gbit/s over distances up to 160 km," *Electron. Lett.* **30**(25), 2159–2160 (1994).
44. P. A. Krug, T. Stephens, G. Yoffe, F. Ouellette, P. Hill, and G. Dhosi, "270 km Transmission at 10 Gbits/s in non-dispersion-shifted fiber using an adjustable chirped 120 mm fiber Bragg grating dispersion compensator," *OFC'95, Tech. Digest* **8**, 428–431 (1995).
45. C. D. Poole, J. M. Wiesenfeld, A. R. McCormick, and K. T. Nelson, "Broadband dispersion compensation by using the higher-order spatial mode in a two-mode fiber," *Opt. Lett.* **17**(14), 985–987 (1992).
46. L. Jacomme, "A model for ray propagation in a multimode graded index-fiber," *Opt. Commun.* **14**, 134–138 (1975).
47. K. Iizuka, *Engineering Optics*, 2nd ed., Springer-Verlag, New York, 1988.
48. P. C. Schultz, "Vapor phase materials and processes for glass optical waveguides," *Fiber Optics*, edited by B. Bendow and S. S. Mitra, Plenum Press, pp. 3–31, 1979.
49. H. Murata, *Handbook of Optical Fibers and Cables*, Marcel Dekker, New York, 1988.
50. K. Hogari, S. Furukawa, K. Tomiyama, Y. Nakatsuji, S. Koshio, and K. Nishizawa, "Optical fiber cables for residential and business premises," *J. Lightwave Technol.* **16**(2), 207–213 (1998).
51. M. Matsumoto, M. Tachikura, T. Katagiri, M. Sato, A. Ide, and M. Miyauchi, "Fully automatic speed fusion splice machine for single mode optical fiber ribbons," *Proc. ECOC'87* **1**, 155–158 (1987).
52. T. Katagiri, M. Tachikura, and Y. Murakami, "Evaluation of fiber slippage and core-axis offset distribution in optical fiber mechanical splice," *J. Lightwave Technol.* **19**(2), 195–204 (2001).
53. T. Kakii, K. Kashiara, T. Komiya, S. Suzuki, Y. Iwamoto, and Y. Sakata, "Development of optical connectors for GI-type subscriber fiber optic cables," *Sumitomo-denki* **132**, 51–59 (1988).